Development of the Wide-Field Camera System Using Kinetic Inductance Detectors for the Antarctic Terahertz Telescope

Tom Nitta

February 2014

Development of the Wide-Field Camera System Using Kinetic Inductance Detectors for the Antarctic Terahertz Telescope

Tom Nitta
Doctoral Program in Physics

Submitted to the Graduate School of
Pure and Applied Sciences
in Partial Fulfillment of the Requirements
for the Degree of Doctor of Philosophy in
Science

at the
University of Tsukuba

Abstract

In this thesis, we present development of a wide field-of-view (FoV) millimeter-wave camera system and a design of a 20000 pixels terahertz camera for the Antarctic terahertz telescope that will be constructed at Dome Fuji, a Japanese Antarctic station.

The Dome Fuji station is in high altitude of 3800 m and the lowest temperature is $-$ 80°C. Therefore it is expected to be one of the best site for millimeter-wave and terahertz astronomical observations. It is very important for astronomy to understand the star-formation history of distant galaxies and to reveal the evolution process of its large-scale structure. The detection of millimeter and terahertz waves from distant galaxies is one of the most recent topics in the cosmic star-formation history. A combination of wide FoV and background-limited sensitivity makes in sufficient to enable the surveys for radio emissions from unknown distant galaxies. For this purpose, construction of ground-based telescopes with wide FoV, as well as the development of large-format ($>$ 1000 pixels) cameras are planned around the world.

In this thesis, a 220-GHz band camera with lens-antenna-coupled microwave kinetic inductance detectors (MKIDs) has been demonstrated. The optical design of our camera is based on a double-slot antenna and an extended hemispherical silicon lens array. A double-slot antenna on a silicon lens produces a symmetrical beam pattern with low side-lobe level, and its assembly is quite simple. A highly integrated small-size ($< 3\lambda$ diameter, where λ is the target wavelength) lens array is required to realize a CCD-like camera. For this reason, close-packed silicon lens arrays with small lens diameters in the 220-GHz band were investigated by simulation of the beam patterns, considering the effects of surrounding lenses. By optimizing the lens shape, good-quality beams with circular symmetry pattern and sidelobe level of $-$ 15 dB were obtained with lens diam-

eters of 1.2λ, 2λ, and 3λ in the bandwidth of 210 $-$ 230 GHz. The silicon lens array was directly machined using a high-speed spindle on an ultra-precision machine. The shape fabrication error and the surface roughness of the top of the lens were typically less than 15 μm (peak-to-valley) and approximately 0.7 μm (rms), respectively.

Anti-reflection (AR) coatings are critical for dielectric lenses with high refractive indices, such as silicon, because such a high refractive index causes reflections of approximately 30% at each material/vacuum interface. Two types of AR coatings for silicon and alumina were studied at 220 GHz band, one is by direct machining of mixed epoxy (Stycast 1266 and 2850FTJ) for a silicon lens array, while the other is antireflective subwavelength structure for a large alumina lens used in a re-imaging optics system. The refractive indices of mixed epoxies were varied linearly as functions of the volume fraction of Stycast 2850FTJ. We successfully obtained epoxies with a target refractive index of 1.84, which matches that of silicon. The thickness of the epoxy AR coating was precisely controlled with direct machining. Transmittance of the AR-coated silicon substrate, measured with a Fourier transform spectrometer, was approximately 95% at the center frequency of the 220 GHz band with a bandwidth of 25% at 27 K. The antireflective subwavelength structure with periodic rectangular pillars was designed for an alumina sample. The measured 220-GHz-band transmittance was higher than 95% with a bandwidth of 25% at 25 K.

Beam patterns of the 220-GHz band camera with lens-antenna-coupled MKIDs were measured by using a millimeter-wave CW source. The comparison of the measured beam patterns with the calculations showed good agreement. This proved that the silicon lens array, processed with the ultra-precision cutting, is capable of performing as the optical system of the millimeter-wave cameras.

By using these technologies, we developed a compact cryogenic re-imaging optics with large-diameter silicon and alumina lenses and 220-GHz band 608 pixel MKID camera for wide FoV observations. The re-imaging optics connects a telescope focus of F/# = 6 at ambient temperature with a focal plane of F/# = 1 at 100 mK for the camera. Three kinds of infrared blocking filters were used to reduce the 300 K radiation from a window with a diameter of 150 mm. A nested baffle was installed to reduce stray light. 220-GHz band transmittance from the window to the MKID camera was approximately 80% with a bandwidth of 25%. The camera has been cooled at 100 mK with 300 K load. High yield of

around 95% has been achieved for the 608 pixel MKID camera. This wide FoV cryogenic optics can be scalable for the Antarctic terahertz telescope.

The Antarctic terahertz telescope has two Nasmyth foci, and the one is used for a large-format terahertz camera. A 850-GHz band re-imaging optics, which connects a Nasmyth focus of F/# = 6 with a focal plane of F/# = 1, was designed. Four free-form reflective mirrors at ambient temperature and a single alumina lens at cryogenic temperature were used to realize the wide FoV with compact configuration. The resulting design solution provided a 1 degree FoV at 850 GHz. A 20000 pixels terahertz camera was also designed based on the technology of 220-GHz band 608 pixel MKID camera.

List of Acronyms and Symbols

AR Anti Reflection

CPW Coplanar Waveguide

EMT Effective Medium Theory

FDM Frequency-Domain Multiplexing

FoV Field-of-View

FTS Fourier Transform Spectrometer

HDPE High-Density Polyethylene

HEMT High Electron Mobility Transistor

HFSS High Frequency Structure Simulator

HPBW Half-Power Beam Width

IR Infrared

LDPE Low-Density Polyethylene

LNA Low-Noise Amplifier

MKID Microwave Kinetic Inductance Detector

NEP Noise Equivalent Power

PO Physical Optics

PWV Precipitable Water Vapor

SED Spectrum Energy Distribution

SMG Submillimeter Galaxy

SWS Sub-wavelength Structure

tanδ Dielectric Loss Tangent

n Refractive Index

λ Wavelength

Acknowledgement

Before anything else, I would like to tell my sincere gratitude to all who gave me a kind advice and support.

Especially, without Prof. Naomasa Nakai, who gave me a chance to get involved in the research, I could not find what I really want to do. When I entered the university, he was willing to help and introduce me to the National Astronomical Observatory of Japan, Advanced Technology Center (NAOJ-ATC) while I was looking for my subject of study. Not only that, he kindly supported me with comfortable environment to proceed the research.

I would like to express my sincere thankfulness to Prof. Yutaro Sekimoto for his enormous assistance and encouragement for five years. He gave me the best research theme, the development of the millimeter- and submillimeter-wave cameras. He always arranged me a wonderful environment to devote myself to my work, and I have learned so many things there.

As for optical design of camera, I learned a lot from Dr. Masato Naruse and Dr. Kenichi Karatsu. They were also kind enough to advice me on measurements of Microwave Kinetic Inductance Detector (MKID).

It was my precious experience to discuss about the development of MKID, its measurements and design of wide field-of-view optics with Mr. Shigeyuki Sekiguchi, Mr. Masakazu Sekine, Mr. Takashi Okada and Mr. Shibo Shu.

I would like to thank Prof. Takashi Noguchi, Prof. Hiroshi Matsuo and Prof. Yoshinori Uzawa for their lots of sincere advice. Especially Prof. Matsuo provided me a chance to use a 0.3 K cryostat and a Fourier transform spectrometer.

Mr. Norio Okada and Mr. Kenji Mitsui kindly cared for me about the lens array development and evaluation. I troubled them many times, but I could finally work up

the designed lens array with their patient support. I also learned about the processing of an anti-reflection coating from them.

Mr. Toshihiro Tsuzuki and Mr. Hiroaki Imada gave me a great support and useful discussion on design of wide field-of view optics for the Antarctic terahertz telescope.

I feel grateful to Dr. Masumichi Seta who advised me a lot on my research. Besides, he always cared for me when he visited NAOJ.

I appreciate members of observational astrophysics group. Even though I was not there so long, it was great to spend time and have many discussions with them. Dr. Shun Ishii and Mr. Taketo Nagasaki, who are involved in the development of the submillimeter-wave receiver, gave me an enormous assistance.

It was very fruitful to receive helpful guidance from Dr. Aritoki Suzuki, Mr. Yuki Inoue and Dr. Tomotake Matsumura about the development of an anti-reflection coating with Stycast epoxy.

I got valuable advice from Dr. Tatsuya Takekoshi and Dr. Tai Oshima while proceed my research. Especially I thank to Dr. Takekoshi to discuss with me about the analysis of HFSS and ZEMAX simulations.

I would like to express my heartfelt gratitude to Prof. Osamu Tajima, Dr. Takafumi Kojima, Dr. Takehiko Wada, Dr. Satoru Mima, Dr. Toyoaki Suzuki, Dr. Hirofumi Inoue, Dr. Hironobu Makitsubo, Mr. Koichi Kuroiwa, Mr. Douta Watanabe, Mr. Hiroki Watanabe, Mr. Norio Sekiya and ALMA members of ATC.

Finally, I thank to my parents, my sister, my grandparents and my wife for their encouragement and continuous support for me at all times.

Contents

1

Introduction

1.1 Distant Galaxy Survey

It is very important for astronomy to understand the star-formation history of distant galaxies and to reveal the evolution process of its large-scale structure. Massive distant galaxies form with processes of accretion and mergers of small galaxies in high-density circumstance. They are expected to be obscured by dust; in fact, which are too weak to detect at optical wavelengths. On the other hand, they are bright enough in observation of the millimeter- and submillimeter-wave range. This type of galaxy called as submillimeter galaxies (SMGs) (Blain et al., 2002). According to the previous studies, SMGs are ultraluminous sources ($> 10^{12} L_{\odot}$, corresponding to a star formation rate of $10^2 - 10^3 M_{\odot}\mathrm{yr}^{-1}$) and have molecular gas reservoirs of $10^{10} M_{\odot} - 10^{11} M_{\odot}$ for their star-formation activities (Tamura et al., 2009). That shows a possibility of their being progenitors of massive elliptical galaxies (Blain et al., 2002). The detection of millimeter and terahertz waves from distant galaxies is one of the most recent topics in the cosmic star-formation history.

The SMG was first detected 16 years ago with the Submillimeter Common User Bolometer Array (SCUBA; Holland et al. 1999) on the James Clerk Maxwell Telescope (JCMT) (Hughes et al., 1998). SCUBA observed the sky in the atmospheric windows at both 450 and 850 μm. In this observations, hexagonal close-packed arrays of 91 and 37 bolometers were used at each wavelength. The discovery of SMGs provided a various potentials of blank-field surveys with the Max-Planck Millimeter Bolometer (MAMBO; Kreysa et al. 1999) on the IRAM 30 m telescope, Bolocam (Haig et al., 2004) on the Caltech Submillimeter Observatory (CSO) and AzTEC (Wilson et al., 2008) on the Atacama Submillimeter Telescope Experiment (ASTE). These wide-field surveys produce a large amount of SMG sample, and that leads to an understanding the population of SMGs. Advanced millimeter- and submillimeter-wave detector technologies have shown a new possibility on an understanding of the distant Universe.

Figure 1.1 shows the multicolor images of GOODS 850-5 which is a hyperluminous submillimeter galaxy in the GOODS-N (Wang et al., 2009). From Fig. 1.1, GOODS 850-5 is not detected in the Advanced Camera for Surveys (ACS) and the Near Infrared Camera and Multi-Object Spectrometer (NICMOS) on the *Hubble Space Telescope* (*HST*), and the Multi-Object InfraRed Camera and Spectrograph (MOIRCS) on the SUBARU telescope. But it is clearly detected in the IRAC 3.6 $-$ 8 μm and the MIPS 24 μm images on *Spitzer*

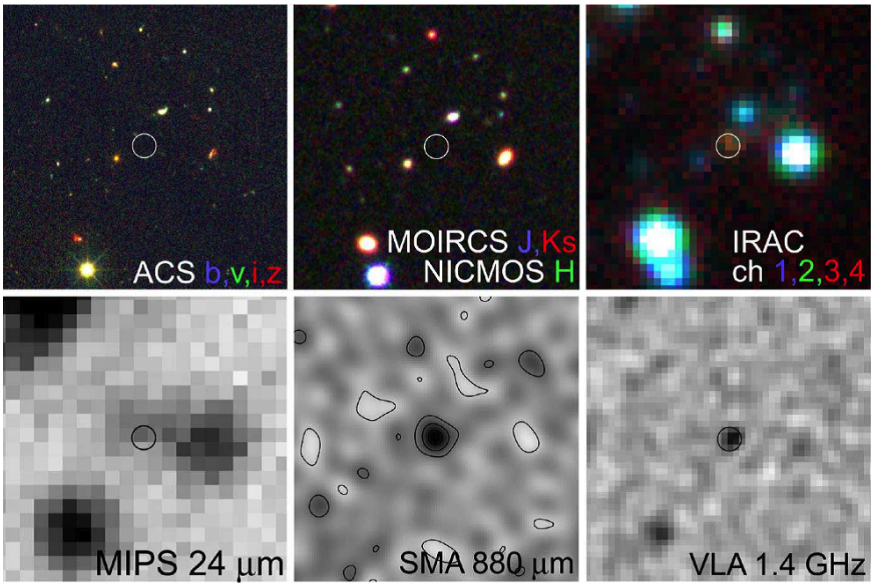

Figure 1.1: Multicolor images of GOODS 850-5 (Wang et al., 2009). GOODS 850-5 is a hyperluminous submillimeter galaxy in the GOODS-N. White circles correspond to the position of GOODS 850-5. Each panel has a 24″ width.

telescope, the Submillimeter Array (SMA) 880 μm image and the Very Large Array (VLA) 1.4 GHz image.

The evolution of galaxy formations is better understood with the redshift distribution of SMGs. However, it is difficult to determine the redshift of SMGs from single-wavelength observation. Moreover, it is very difficult to identify a clear counterpart for spectroscopic follow-up because the positional accuracy of submillimeter wave images are comparatively poor. Under such environment, multi-band observation by using large-format millimeter- and submillimeter-wave cameras is important for determining the spectrum energy distributions (SEDs) of SMGs. Figure 1.2 shows the photometric redshift distribution of 74 SMGs which were detected at 870 μm by the Large APEX BOlometer CAmera (LABOCA; Siringo et al. 2008) observations in the Extended Chandra Deep Field South (ECDFS) (Wardlow et al., 2011). From those results, it is obvious that the redshifts of almost all galaxies are greater than unity, and that the median value of the redshift distribution is likely to be of $2 - 3$. This result is consistent with the other observations (Clements et al., 2008; Dye et al., 2008; Chapman et al., 2005).

Figure 1.3(A) shows the predicted flux density of a SMG as a function of redshift (Blain et al., 2002). As shown in Fig. 1.3(A), the flux density which is almost inde-

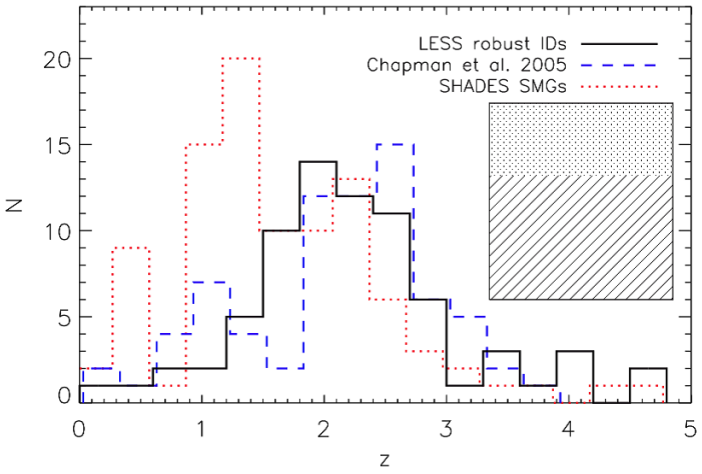

Figure 1.2: The photometric redshift distribution of 74 SMGs which were detected at 870 μm by the LABOCA observations in the Extended *Chandra* Deep Field South (black solid line) (Wardlow et al., 2011). This figure includes the photometric redshift distribution of SCUBA Half-Degree Extragalactic Survey (SHADES) SMGs (Clements et al., 2008; Dye et al., 2008), and the spectroscopic redshift distribution of SMGs from Chapman et al. (2005). The median redshift of SMGs in LABOCA ECDFS Submillimeter Survey (LESS) is $z = 2.2 \pm 0.1$.

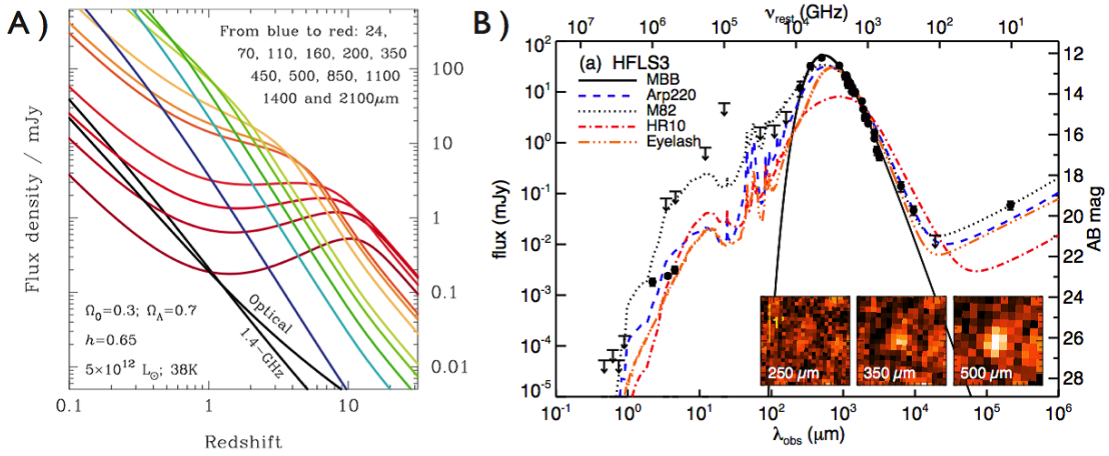

Figure 1.3: (**A**) The predicted flux density of a dusty starburst galaxy (SMG) as a function of redshift in various millimeter/submillimeter-wave atmospheric windows (Blain et al., 2002). From blue to red lines correspond to flux density of 24, 70, 110, 160, 200, 350, 450, 500, 850, 1100, 1400 and 2100 μm. From the millimeter- and submillimeter-wave observations of 350 — 2100 μm, the flux density which is almost independent of redshift is obtained. (**B**) Spectral energy distribution (SED) and *Herschel*/SPIRE images of HFLS3 (Riechers et al., 2013). HFLS3 was identified as a very high redshift (z = 6.3369) source. *Herschel*/SPIRE images of 250-, 350-, and 500-μm bands are shown (inset).

pendent of redshift is obtained from the observations at the wavelength of 850 $-$ 1100 μm. Thus if SMGs exist at higher redshifts, observations at millimeter wavelengths are a powerful way to find them. On the other hand, recently, SMGs at high redshifts have been detected from submillimeter-wave observations. Figure 1.3(B) shows the SED and $Herschel$/SPIRE images of HFLS3, which corresponds to high-redshift SMG at z〜6.34 (Riechers et al., 2013). This SMG was very bright at submillimeter wavelength because the peak frequency of dust emission is around 600 GHz. Thus the submillimeter-wave observations are suitable for the detection of the high-redshift ($z \sim 6$) SMGs.

From these reasons, both millimeter- and submillimeter-wavelength observations are required to detect the SMGs at wide-ranging redshifts. A significant point of both observations are summarized as follows.

Millimeter-Wave Range (around 200 GHz) Observations

- A large number of SMG can be detected due to the negative K-correction.
- A large-format camera in the millimeter-wave band is also suitable for observing the 2.7 K cosmic microwave background radiation (CMB), which has a peak emission around 200 GHz.
- In addition, deeper understanding of the evolution of galaxies and galaxy clusters is expected from observations of the thermal and kinetic Sunyaev $-$ Zel'dovich effects (Vanderlinde et al., 2010; Marriage et al., 2011; Sayers et al., 2013).

Submillimeter-Wave Range (around 800 GHz) Observations

- A high-redshift ($z \sim 6$) SMG can be detected because the peak frequency of dust emission from these sources is around 800 GHz (see Fig. 1.3(B)).
- The observations at this frequency bands are useful in determining of the photometric redshift.

Table 1.1: The millimeter/submillimeter-wave single dish telescopes around the world.

Telescope	Dish Diameter [m]	Location	Altitude [m]
ASTE	10	Atacama Desert, Northern Chile	4860
NRO	45	Nobeyama, Japan	1350
APEX	12	Atacama Desert, Northern Chile	5100
JCMT	15	Mauna Kea, Hawaii	4092
IRAM	30	Pico Veleta, Spain	2850
CSO	10	Mauna Kea, Hawaii	4070
ACT	6	Atacama Desert, Northern Chile	5190
SPT	10	South Pole, Anterctica	2835

1.2 Wide Field-of-View Observations

As discussed previously, the advanced millimeter/submillimeter-wave instruments such as large-format camera will offer new insight into the history of galaxy formation. A combination of wide field-of-view (FoV) and background-limited sensitivity makes in sufficient to enable the surveys for radio emissions from unknown distant galaxies. For this purpose, construction of ground-based telescopes such as the Cerro Chajnantor Atacama Telescope (CCAT; Sebring 2010), and Antarctica terahertz telescope (Imada et al., in prep, Tsuzuki et al., 2014), as well as the development of large-format cameras are planned around the world.

Tables 1.1 and 1.2 show the existing single dish telescopes and large-format millimeter/submillimeter wave cameras, respectively. The number of detectors for astronomical observations has exponentially increased, as shown in Fig. 1.4. Many array detectors, such as Microwave Kinetic Inductance Detector and Transition Edge Sensor, have been developed all over the world with various detection schemes. Recent developments of the large formatted millimeter/submillimeter cameras (the number of pixels > 1000), such as SCUBA2 (Holland et al., 2013) on JCMT, the Multiwavelength Submillimeter kinetic Inductance Camera (MUSIC; Maloney et al. 2010) on CSO, SPT-SZ (Ruhl et al., 2004) on South Pole Telescope (SPT) and A-MKID on Atacama Pathfinder Experiment (APEX) will open a window to large and deep surveys at millimeter/submillimeter wavelength.

Wide-field observations with a large-format camera play a complementary role with high angular and high frequency resolution observations with the Atacama Large Millimeter/submillimeter Array (ALMA; Wootten & Thompson 2009)whose early science

Table 1.2: Summary of developed millimeter/submillimeter-wave cameras.

	Frequency [GHz]	Number of Pixels	Telescope
SCUBA	350 / 650	37 / 91	JCMT
SCUBA-2	350 / 650	5120 / 5120	JCMT
AzTEC	270	144	ASTE/JCMT
MUSTANG	90	64	GBT
Bolocam	143 or 270	144	CSO
SHARC-2	850	384	CSO
MUSIC	150 / 220 / 300 / 350	576 / 576 / 576 / 576	CSO
MAMBO	250	37	IRAM
GISMO	150	128	IRAM
NIKA	150	30 & 42	IRAM
NIKA-2	150 / 240	144 / 256	IRAM
LABOCA	345	295	APEX
APEX-SZ	150	330	APEX
ArTeMiS	670 / 850 / 1500	2304 / 2304 / 1152	APEX
A-MKID	350 / 850	3520 / 21600	APEX
PolarBEAR	150	1274	PolarBEAR
SPT-SZ	95 / 150 / 220	160 / 640 / 160	SPT
SPTpol	90 / 150	180 / 588	SPT
MBAC	145 / 215 / 280	1024 / 1024 / 1024	ACT
ACTPol	90 / 150	∼ 1000 / ∼ 2000	ACT

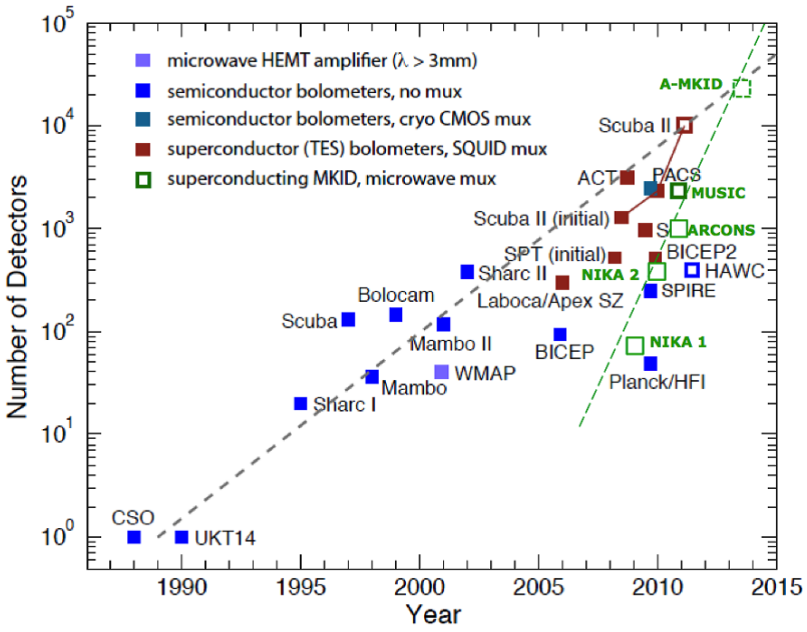

Figure 1.4: Increasing the number of detectors for astronomy. This figure is from J. Baselmans.

observations have just started.

1.3 Antarctica as a Site for Astronomy

The radio-waves, especially millimeter- and submillimeter-waves, are absorbed by water vapor in the atmosphere. Therefore, the followings are required to observe the weak signals from distant galaxies at millimeter- and submillimeter-waves on the ground:

- millimeter/submillimeter observations can be obtained only at dry and high-altitude sites.
- atmospheric stability, cloud amount and wind speed are very important because these weather conditions affect pointing of telescopes and practical observational time.

From these reasons, the Atacama desert in northern Chile and the Mauna Kea in Hawaii have been commonly used for astronomical observations because of its high altitude and transmittance.

The Antarctic plateau may be the best place for astronomical observations at millimeter- and submillimeter-waves, and terahertz bands because is the highest, driest and coldest of the continents on the Earth. Figure 1.5 shows the Antarctic continent and sites. The sites where astronomical work has taken place or is under consideration are South Pole, Domes A, C, and Fuji (Saunders et al., 2009). The Japanese Antarctic station, Dome Fuji station (77°19'South, 39°42'East) is located at an altitude of 3800 m on a plateau halfway between the South Pole and the Showa Station (Ishii et al., 2010). The distance from the Syowa station is about 1000 km. The annual average temperature and the lowest temperature were $-$ 54.4 °C and $-$ 79.7 °C, respectively (Yamanouchi et al., 2003). Therefore, very small optical depth is expected at Dome Fuji station. The characteristics of Dome Fuji are summarized in the followings.

Wind Speed

Strong wind condition (typically $>$10 ms^{-1}) leads to a variety of problems in a large diameter ($>$ 10 m) telescope, such as oscillations of main reflector and a pointing errors. According to Burton (2010), the Antarctic atmospheric circulation pattern centers about

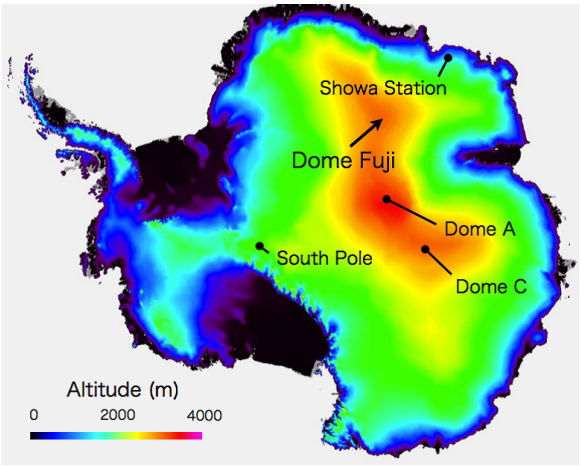

Figure 1.5: The Antarctic continent and the location of Dome Fuji.

the South Pole, and the dominant airflow is a slow settling from the atmosphere. This wind is katabatic in origin, starting from the highest points and picking up speed as it falls towards the coast, under gravity. Over the highest parts of the plateau typical wind speeds are only $1 - 2\ \mathrm{ms}^{-1}$.

Precipitable Water Vapor

The atmospheric attenuation is mainly determined by the amount of water vapor and oxygen. The PWV of dry and high altitude sites such as Mauna Kea in Hawaii falls to 1 mm on the best of days. The PWV level of Atacama desert in Northern Chile occasionally reaches as low as 300 μm (Burton, 2010). Figure 1.6(A) shows the nocturnal fractional cloud cover from satellite instruments (Saunders et al., 2009). Blue color corresponds to the region that has least cloud amounts. Figure 1.6(B) shows the predicted winter PWV in Antarctica (Swain & Gallée, 2006). Purple color shows the area that has least PWV level. This area correspond to the high-alititude region. PWV quantiles of Domes A, C, Fuji and South Pole from the MHS experiment on the NOAA-18 satellite were summarized in Table 1.3 (Saunders et al., 2009). It is clear that the PWV levels of Domes A, C, and F are smaller than that of South Pole. In addition, there is little difference in PWV levels between Domes A and Fuji. At Dome Fuji station, annual average PWV below 300 μm, and PWV in ten percent of winter below 100 μm. This excellent PWV is one of the most advantageous points over the other sites on Earth and that leads to the efficient

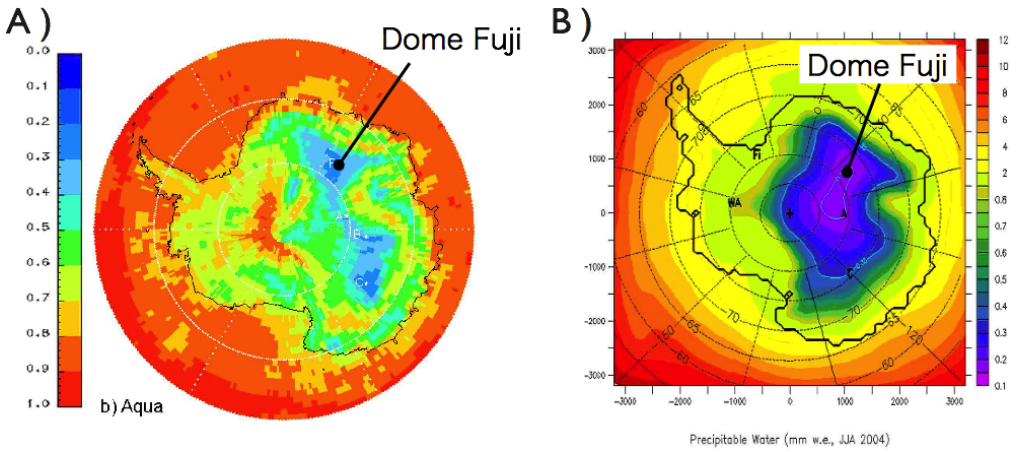

Figure 1.6: (**A**) Nocturnal fractional cloud cover from satellite instruments, Aqua CERES-MODIS, for 18 September — 11 November 2003 (Saunders et al., 2009). (**B**) Predicted winter precipitable water vapor (PWV) in Antarctica (Swain & Gallée, 2006).

Table 1.3: Precipitable water vapor (PWV) quantiles of Domes A, C, Fuji and South Pole from the MHS sensor, for 2008 (Saunders et al., 2009). Units are microns. ' Winter 'means days 120 — 300.

	Annual med.	Winter med.	Winter 25%	Winter 10%
Dome Fuji	279	163	114	90
Dome A	233	141	103	71
Dome C	342	235	146	113
South Pole	437	324	258	203

observation at millimeter- and submillimeter-wave and terahertz bands.

Atmospheric Stability

The combination of low temperature, high altitude and low cloud amount, a very small optical depth and its stability is expected at the Dome Fuji station. Recently, the 220-GHz optical depth at Dome Fuji in summer season was measured by the tipping radiometer (Ishii et al., 2010). Also the optical depth at Atacama Desert was measured from 1995 to 2004.

Figure 1.7 shows the measured optical depths at these sites (Ishii et al., 2010). (a), (b) and (c) of Fig. 1.7 correspond to the data of Dome Fuji in summer (17 December 2006 — 14 January 2007), Atacama Desert in best summer (17 December 2002 — 14 January 2003) and Atacama Desert in best winter (17 August 1999 — 14 September 1999). As shown in

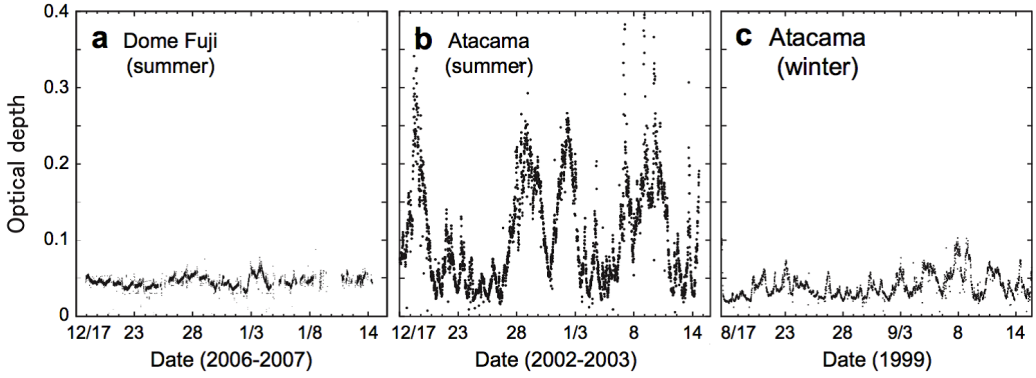

Figure 1.7: Comparison of variations in the 220/225 GHz optical depth between Dome Fuji and the Atacama ALMA site (Ishii et al., 2010). (**a**) Dome Fuji in summer (17 December 2006 — 14 January 2007), (**b**) Atacama in best summer (17 December 2002 — 14 January 2003), and (**c**) Atacama in best winter (17 August 1999 — 14 September 1999).

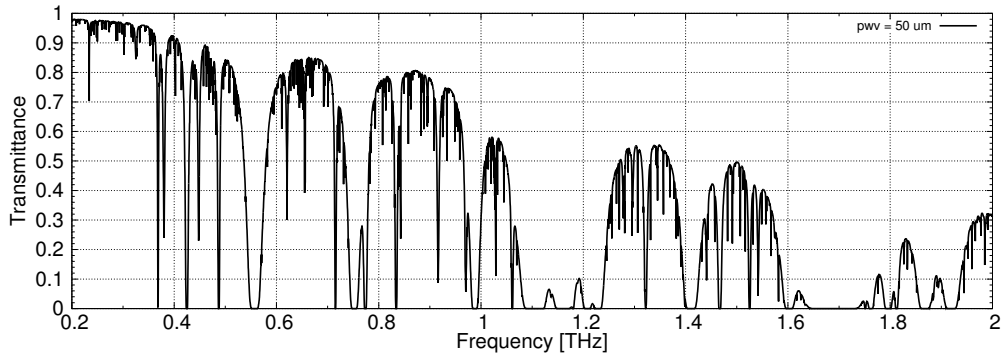

Figure 1.8: Simulated spectrum of the atmospheric-transmittance at Dome Fuji under the expected best conditions; pwv = 50 μm (Ishii et al., 2010).

Fig. 1.7(a), the measured 220-GHz optical depth at Dome Fuji was less than 0.06. This implies that submillimeter observations would be always possible even summer of Dome Fuji station (Ishii, 2011). From Fig. 1.7(a), an average of the optical depth was 0.045 and its standard deviation was 0.007 during the total period of its measurements. This small deviation indicates that the optical depth was very stable at Dome Fuji station. Also, the average summer optical depth of 0.045 corresponds to the PWV of 0.6 mm (Ishii, 2011).

Transmittance

Ishii et al. (2010) showed the simulated spectrum for the case of the 50 μm PWV which is expected at Dome Fuji station in winter. Figure 1.8 shows the simulated transmittance as a function of frequency. Under the best condition in winter at the Dome Fuji station,

the transmittance is better than 80% at atmospheric windows up to 1 THz. In addition, it should be noted that the several THz windows such as 850- and 1500-GHz bands open. These windows are only available at the Antarctic continent in winter on the Earth.

From these reasons, the Dome Fuji station is expected as one of the best site on the Earth for millimeter-wave and terahertz astronomical observations. We plan to install the large-format camera on the Antarctic 10-m terahertz telescope that will be constructed at the Dome Fuji station, and will perform the wide blank-field surveys for the detection of the unknown distant galaxies.

1.4 Goals and Overview of this Thesis

The primary goal of this thesis includes the development and the evaluation of a large-format (around 1000 pixels) millimeter-wave camera, and the design of a wide field (around 10000 pixels) submillimeter-wave camera for the Antarctica terahertz telescope. Sub-goals of this thesis are summarized in the following lists:

- Chapter 2: Review of the superconducting direct detector and optical element for millimeter/submillimeter-wave camera.
- Chapter 3: Measurement of optical properties of lens material by using Fourier transform spectrometer, and the development of an extended hemispherical lens array for 220- and 440-GHz band observations.
- Chapter 4: Measurement of the forward transmission (S_{21}) response of an MKID array, and 220- and 440-GHz band far-field beam patterns of the extended hemispherical silicon lens array fed by the double-slot antennas at 0.3 K.
- Chapter 5: Electromagnetic field simulation of a close-packed lens array for high-frequency (near terahertz) band and study the effect of misalignment between a silicon lens and a double-slot antenna.
- Chapter 6: Design, fabrication and transmission measurement of an anti-reflection coating layer for cryogenic silicon and alumina lenses.

- Chapter 7: Development of a 220-GHz band 608 pixel camera and its wide field-of-view re-imaging optics operating at 0.1 K by using a dilution refrigerator.
- Chapter 8: Design of the Antarctic 10-m terahertz telescope and its 1 degree field-of-view re-imaging optics, and 850-GHz band submillimeter-wave camera as a first-generation instrument.
- Chapter 9: Summarize the work described in this thesis.

2

Millimeter/Submillimeter-Wave Kinetic Inductance Detector Camera

2.1 Superconducting Detectors for Direct Photon Detection

To observe unknown distant galaxies and Sunyaev-Zel'dovich effects toward massive galaxy clusters, it is necessary to develop a large-format camera with more than 1000 pixels. Many types of direct detector array have been developed all over the world with various detection scheme. In this section, some types of superconducting direct detectors are introduced.

Superconducting-Insulator-Superconducting Photon Detector

Superconducting-insulator-superconducting (SIS) junctions, or superconducting tunnel junctions (STJ), have been widely used as mixers for the millimeter- and submillimeter-wave heterodyne receivers (Zmuidzinas & Richards, 2004). In addition, SIS junctions also act as a direct detector for photon detection by using photon assisted tunneling of a quasi-particle. Basic principle of the SIS photon detector is the same as for the SIS heterodyne mixers. In case of direct detectors, an incident photon changes current-voltage (I-V) characteristics and the change of DC current correspond to the power of the incident photon.

Typically the SIS junctions are made of Nb/Al/AlOx/Al/Nb layers (Matsuo et al., 2006). Niobium SIS junctions have a superconducting gap energy (2Δ) of about 3 meV which corresponds to the frequency of about 700 GHz. In this case, the frequency up to 700 GHz can be detected by photon assisted tunneling process. Low leakage-current of SIS photon detector leads to the high-sensitivity detection. Ariyoshi et al. (2005) reported the residual leakage current of 100 pA at 0.3 K with noise equivalent power (NEP) of about 10^{-16} W/$\sqrt{\mathrm{Hz}}$. This sensitivity is enough for the ground-based millimeter- and submillimeter-wave observations with background-limited performance.

Transition Edge Sensor

A superconducting transition-edge sensor (TES; Irwin 1995) is composed of a superconducting thin film operated in the very narrow temperature region between the superconducting and the normal state. Transition temperature of superconducting thin film is typically $100 - 300$ mK, and transition range is typically in the order of milli-Kelvin. While in its transition from superconducting state to normal state, a large change of resis-

tance is caused by a small change of temperature. The sharp transition leads to the high sensitivity. However, it provides lower saturation energy and is difficult to control the bias point of many detectors.

TES is often operated with voltage-bias, and is thermally connected to a cold stage whose temperature is below the superconducting transition temperature. When energy of incident photons is absorbed into the TES, its temperature rises causing its resistance to increase. The increase of resistance decreases the current flowing through the TES. The change of current is measured by the superconducting quantum interference device (SQUID) amplifiers. A multiplexed readout of TES arrays is realized by using SQUID amplifiers. Large-format TES arrays with SQUID amplifiers are currently used in several experiments such as CMB observations (Ruhl et al., 2004; Lee et al., 2008).

Microwave Kinetic Inductance Detector

Microwave kinetic inductance detectors (MKIDs) (Day et al., 2003) with superconducting microresonators are a promising technology for large-format ($>$1000 pixels) cameras (Zmuidzinas, 2012). MKIDs consist of superconducting resonators whose resonance frequencies are distributed in the microwave range, typically $1 - 12$ GHz. Incident photons, which have higher energy than the superconducting gap energy (2Δ), break Cooper pairs and create quasi-particles in the resonator. The increase in the number of quasi-particles induces a change in the surface impedance of the superconducting film, which decreases the resonance frequency and the quality factor of the resonator. Millimeter and submillimeter wave signals are observed by monitoring the shift of the resonance frequency.

2.2 Principle of the Microwave Kinetic Inductance Detector

A simple MKID consists of a quarter-wavelength resonator with coplanar waveguide (CPW) geometry that is capacitively coupled to a CPW feed line. Major advantages of MKIDs over other superconducting detectors, such as TES and SIS photon detectors are:

- In the case of a coplanar waveguide (CPW) resonator, the fabrication process is simple and that leads to high detector yield.

Table 2.1: Superconducting materials suitable for millimeter/submillimeter-range direct detectors.

	Critical Temperature [K]	Gap Energy [GHz]
Nb	9.23	680
Pb	7.19	530
V	5.3	390
Ta	4.39	320
Re	1.70	125
Al	1.20	90
Ti	0.45	35
Hf	0.165	12

- A cryogenic part of the measurement system is very simple configuration. A hundreds of pixels can be read out with only two coaxial cables and one cold low-noise amplifier, and that leads to a reduction of the thermal load on the MKID camera.
- A read out of large-format arrays using frequency domain multiplexing is easily achievable.
- A broadband radiation from the millimeter-wave to the X-ray can be detected. Because the MKID is a superconducting pair breaking detector which can detect photons with higher energies than a superconducting gap energy (2Δ).
- When we use an aluminum as a superconducting thin film, high sensitivity with NEP of about 10^{-19} W/$\sqrt{\mathrm{Hz}}$ has been demonstrated (De Visser et al., 2012).

From these reasons, MKID has been widely developed in the millimeter and sub-millimeter wave ranges (Monfardini et al., 2011; Yates et al., 2011; Neto et al., 2009; Maloney et al., 2010), and was chosen as a detecting device for our cameras.

In order to break a Cooper pair and to excite quasi-particles, the energy E_g is required. The energy E_g is expressed as follows,

$$E_g = 2\Delta(T), \tag{2.1}$$

where $2\Delta(T)$ is the gap energy of the superconductor. The gap energy $\Delta(T)$ is represented as follows,

$$2\Delta(0) = 3.528kT_c, \tag{2.2}$$

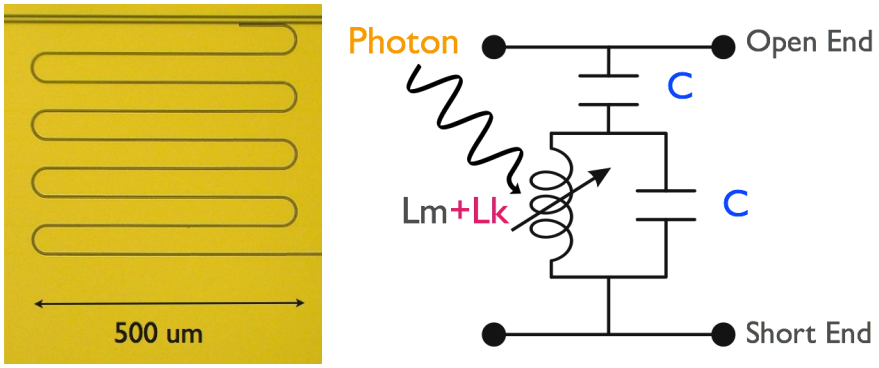

Figure 2.1: (*Left*) A micrograph of a superconducting resonator. The bottom-right end of the superconducting resonator is terminated by a shorted end and an opposite side of resonator is open end. The open end of the resonator is capacitively coupled to the feed line. (*Right*) The equivalent circuit of the quarter-wavelength resonator.

where k and T_c correspond to the Boltzmann constant and superconducting critical temperature, respectively. Critical temperature and corresponding gap energy of the various superconductors are summarized in Table 2.1. MKID detects photons with higher energies than a superconducting gap energy 2Δ. In case of aluminum MKID, it detects photons at frequencies higher than 90 GHz.

2.2.1 Quarter-wavelength Resonators

The quarter-wavelength resonator consists of a quarter-wavelength section of transmission line and a series combination of a coupling capacitor. A micrograph of a superconducting quarter-wavelength resonator is shown in the left panel of Fig. 2.1. The bottom-right end of the superconducting resonator is terminated by a shorted end. The opposite side of resonator is open end. The open end of the resonator is capacitively coupled to the feed line. The equivalent circuit of the quarter-wavelength resonator is shown in the right panel of Fig. 2.1.

Coplanar waveguide (CPW) was used as a transmission line of a quarter-wavelength resonator. The CPW has an advantage over other transmission lines such as microstrip line: the fabrication process is simple because CPW line consists of dielectric substrate and single superconducting film. A center line and planes on both sides of the central line correspond to a transmission line and ground planes, respectively. Figure 2.2 shows a geometry of CPW and its electric field distribution. The effective dielectric constant ϵ_{eff}

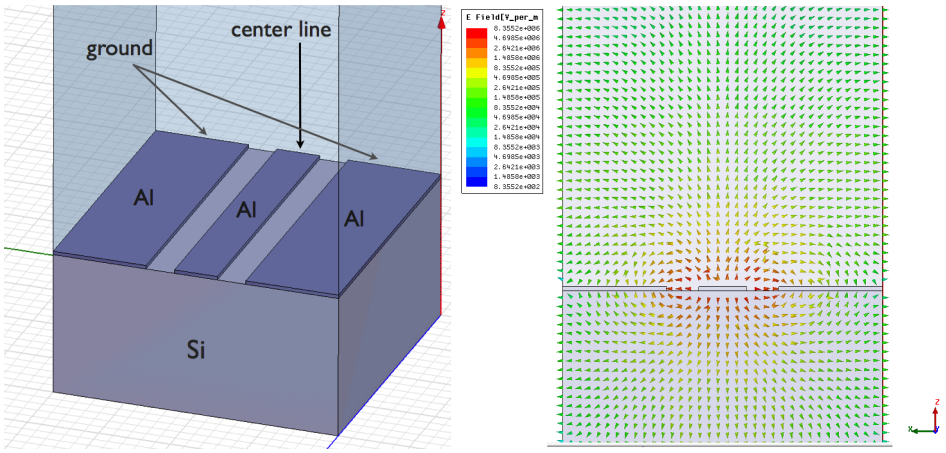

Figure 2.2: (*Left*) A geometry of coplanar waveguide (CPW) with a center line width of S, and gap width of W. S and W of our superconducting resonator are 3 μm and 2 μm, respectively. (*Right*) A cross section of the CPW. The electric field vector is depicted by the color arrows.

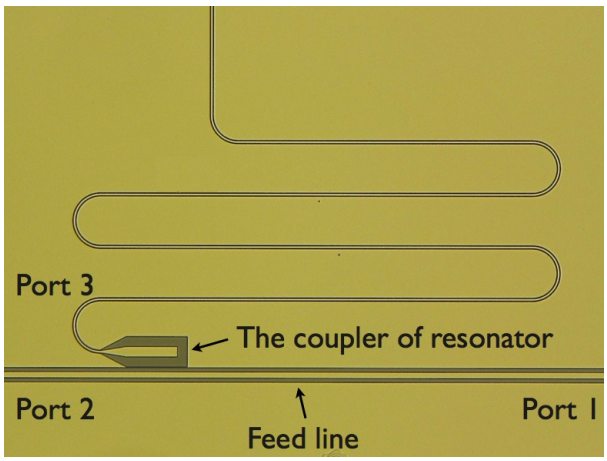

Figure 2.3: A microscopic picture of a feed line and a coupler part of a resonator. The light and dark parts correspond to the aluminum film and the silicon wafer, respectively. The thickness of aluminum film is approximately 150 nm.

of CPW line is defined as

$$\epsilon_{eff} = \frac{\epsilon_{sub} + 1}{2}, \tag{2.3}$$

where ϵ_{sub} is the dielectric constant of substrate. Also, effective wavelength inside CPW line is defined as

$$\lambda_{eff} = \frac{\lambda_{air}}{\sqrt{\epsilon_{eff}}}. \tag{2.4}$$

To design the CPW type quarter-wavelength resonator, these parameters are used.

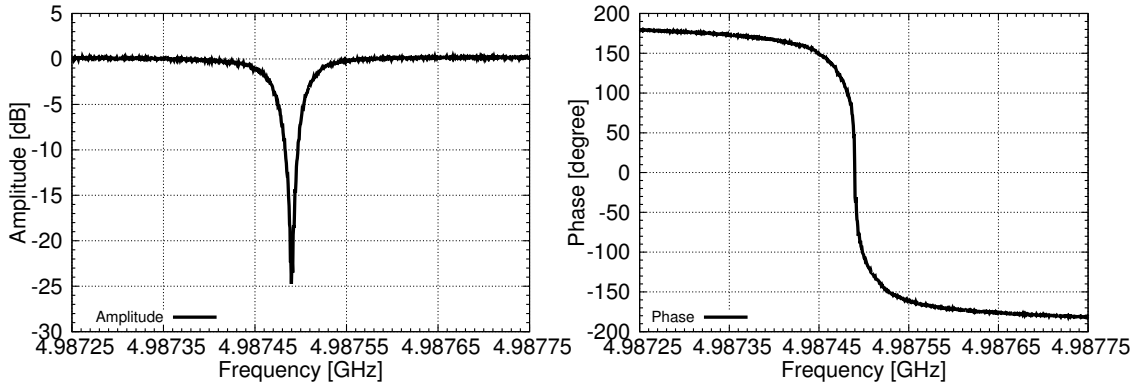

Figure 2.4: (*Left*) Amplitude and (*Right*) phase responses of the superconducting resonator. Measured temperature was 100 mK and whose resonant frequency was 4.9875 GHz.

Figure 2.3 shows an extended figure of coupler part of a resonator. The light and dark parts correspond to the aluminum film and the silicon wafer, respectively. The coupling energy is defined as

$$Q_c = \frac{\pi}{2|S_{13}|^2}, \tag{2.5}$$

where S_{13} is the scattering matrix element which indicates the energy transmission from feed line to coupler. The coupling energy depends on the width and the length of coupler part, and the distance between feed line and coupler.

The resonance frequency is determined by the length of resonator. The resonant frequency ω_0 of a quarter-wavelength resonator of length l is given by,

$$\omega_0 = \frac{2\pi}{4l\sqrt{(L_g + L_k)C}}, \tag{2.6}$$

where L_k, L_g and C correspond to the kinetic inductance, the geometric inductance and capacitance per unit length, respectively. Incident photons, which have higher energy than the superconducting gap energy, break Cooper pairs and that leads to a change of the kinetic inductance. The change of the resonant frequency is expressed as follows.

$$\omega_0 - \Delta\omega_0 = \frac{2\pi}{4l\sqrt{(L_g + L_k + \Delta L_k)C}}. \tag{2.7}$$

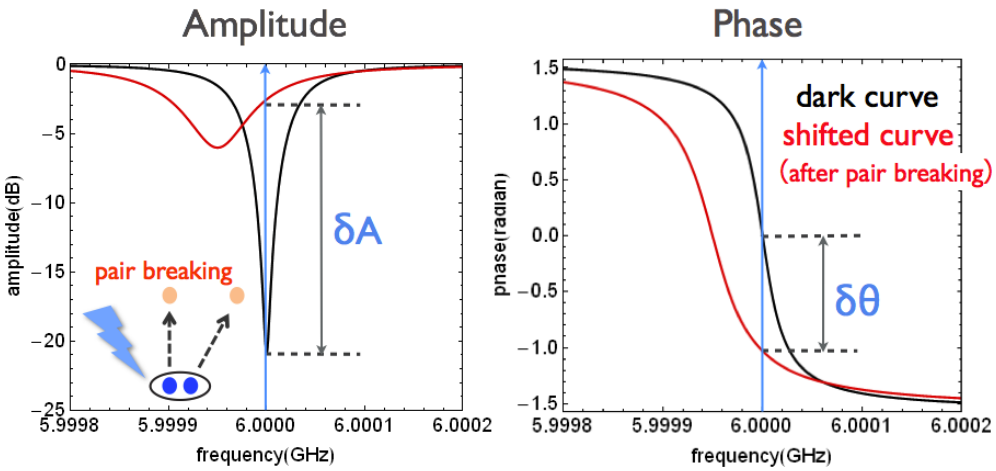

Figure 2.5: A incident photon with energy $h\nu$ breaks Cooper pair, and that leads to the creation of the quasi-particles (inset). The increase in the number of quasi-particles induces a change in the surface impedance of the superconducting film. Consequently the resonance frequency of the resonator (amplitude and phase readout) shifts.

2.2.2 Amplitude and Phase Readout

The real and the imaginary parts of forward transmission spectrum (S_{21}) are measured by using a homodyne detection scheme. Amplitude and phase responses of MKID are described as follows;

$$A = \sqrt{\mathrm{Re}(S_{21})^2 + \mathrm{Im}(S_{21})^2}, \tag{2.8}$$

$$\theta = \tan^{-1} \frac{\mathrm{Im}(S_{21})}{\mathrm{Re}(S_{21})}, \tag{2.9}$$

where, $\mathrm{Re}(S_{21})$ and $\mathrm{Im}(S_{21})$ are the real and the imaginary parts of forward transmission spectrum S_{21}. Figure 2.4 shows the amplitude and the phase responses of the superconducting aluminum quarter-wavelength resonator. Measured temperature was 100 mK and its resonant frequency was 4.9875 GHz. When the incident photons break Cooper pairs and create quasi-particles in the resonator, the resonance frequency changes slightly as shown in Fig. 2.5. The black and red lines are the resonance curves before and after pair-breaking, respectively. Radio wave signals from unknown distant galaxies are observed by monitoring the shift of the resonance frequency.

2.2.3 Quality Factor

Sharpness of the resonance is defined by quality factor of a resonator. The loaded quality factor Q_l, which corresponds to total quality factor of quarter-wave resonator, is expressed as

$$\frac{1}{Q_l} = \frac{1}{Q_c} + \frac{1}{Q_i}, \tag{2.10}$$

where Q_c is a coupling quality factor between a feed line and the resonator, and is given by Eq. 2.5. Q_i is an internal quality factor which is determined by the losses in the superconducting film. The higher Q_i is desirable to improve the sensitivity of the superconducting resonator. Therefore, high-quality superconducting aluminum films have been fabricated using a molecular beam epitaxy system (Naruse et al., 2012; Naruse, 2012). The resonators made from high-quality films have internal quality factors reaching values on the order of 10^6. To obtain the highest loaded quality factor, the condition Q_c = Q_i is required. Therefore, Q_c is designed with 10^5 to 10^6.

2.2.4 Multiplexing Readout

To reduce the number of cryogenic wires, multiplexing readout technique is very important for large-format array. Basically, there are two types of multiplexing readout techniques: time-domain multiplexing (TDM) and frequency-domain multiplexing (FDM). In case of TDM, total available time is divided into several detectors. On the other hand, in case of FDM, total frequency bands are divided into several detectors. This technique has been demonstrated by integrating SQUIDs with TES (Lanting et al., 2004; Irwin & Hilton, 2005).

In case of MKID, it is possible to fabricate a large number of resonators ($>$ 1000 resonators) with slightly different resonant frequency and to couple all the one feed line. A concept of frequency-domain multiplexing of MKID array is shown in Fig. 2.6. The three resonators have slightly different transmission line length, and which are connected to one feed line. Consequently, three resonators are multiplexed in the frequency domain. It is a great advantage over other direct detectors. As discussed previously in section 2.2.3, a resonance of MKID has a high quality factor of order 10^6. If the quality factor of order 10^6 and $\sim$ 2 MHz detector spacing, it is possible to readout a 3000 pixel MKID array with $\sim$ 6 GHz bandwidth by using only two coaxial cables and a low noise amplifier

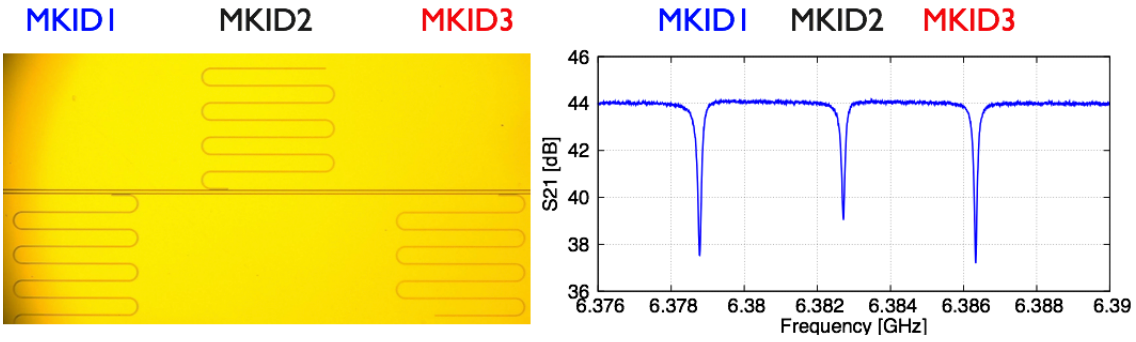

Figure 2.6: A concept of frequency multiplexing of MKIDs.

with HEMT technology.

2.2.5 Noise

The theoretical noise limit of MKIDs is dominated by the random generation of quasi-particles and the subsequent recombination, generation-recombination noise. The generation-recombination noise limited Noise Equivalent Power (NEP) is described as follow (Sergeev et al., 2002).

$$NEP_{gr}(T) = \frac{2\Delta}{\eta}\sqrt{\frac{N_{qp}(T)}{\tau_{qp}(T)}} \quad [\mathrm{W}/\sqrt{\mathrm{Hz}}], \tag{2.11}$$

where Δ is the superconducting energy gap, η is conversion efficiency of incident photon energy into quasi-particles and typically ~ 0.6 (Kozorezov et al., 2000), N_{qp} is the quasi-particle number of thermal excitations, τ is quasi-particle recombination lifetime, and T is the bath temperature of the MKIDs. As will be noted from Eq. 2.11, the reduction of the quasi-particles density and the extension of the quasi-particle lifetime lead a good sensitivity of a MKID.

The quasi-particle number of thermal excitations (N_{qp}) is given by:

$$N_{qp} = n_{qp}V, \tag{2.12}$$

where n_{qp} is the density of quasiparticles and V is the volume of MKID. In the thermal equilibrium state, the temperature dependence of the quasiparticle density (n_{qp}) is given by (Bardeen et al., 1957):

Table 2.2: The critical temperature (T_c), the absolute single spin density at the Fermi level ($N^a(0)$) and the characteristic electron-phonon interaction time (τ_0) of niobium, tantalum, and aluminum films.

	T_c [K]	N^a [$eV^{-1}m^{-3}$] (McMillan, 1968)	τ_0 [ns] (Kaplan et al., 1976)
Nb	9.25	$7.60 \cdot 10^{28}$	0.149
Ta	4.47	$6.43 \cdot 10^{28}$	1.78
Al	1.175	$1.72 \cdot 10^{28}$	438

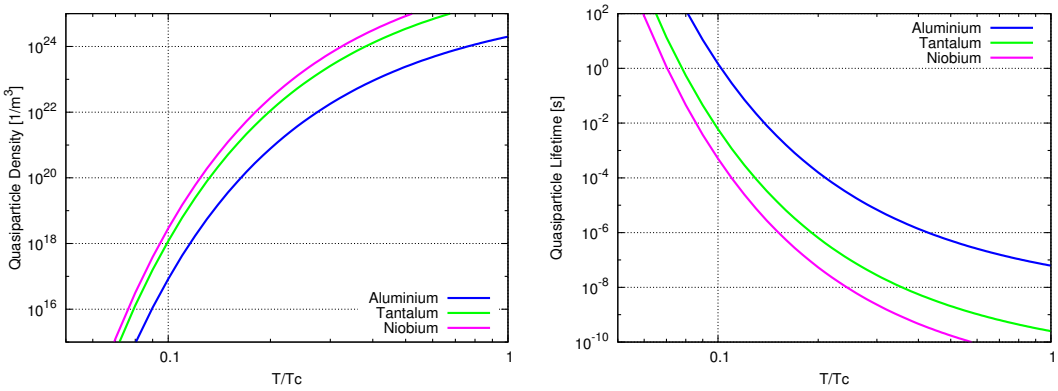

Figure 2.7: (*Left*) The temperature dependence of the quasiparticle density and (*Right*) the recombination time of aluminum, tantalum, and niobium films.

$$n_{qp}(T) = 2N^a(0) \int_{\Delta}^{\infty} N(E) f(E) dE \simeq 2N^a(0) \sqrt{2\pi kT\Delta} \exp\left(\frac{-\Delta}{kT}\right), \tag{2.13}$$

where $N^a(0)$ is the absolute single spin electron density of states at the Fermi level, E is the quasiparticle energy with respect to the Fermi energy, f is the Fermi function and k is the Boltzmann constant. The temperature dependence of quasi-particle recombination lifetime is given by (Kaplan et al., 1976):

$$\frac{1}{\tau_{qp}(T)} = \frac{\sqrt{\pi}}{\tau_0} \left(\frac{2\Delta}{kT_c}\right)^{5/2} \left(\frac{T}{T_c}\right)^{1/2} \exp(-\Delta/kT), \tag{2.14}$$

where τ_0 is a characteristic electron-phonon interaction time. The characteristic properties are summarized in Table 2.2. The quasiparticle density of aluminum, tantalum, and niobium as a function of temperature is shown in the left panel of Fig. 2.7. In this calculation, typical MKID volume (center-line part of CPW resonator) of 5 mm in length, 3 μm

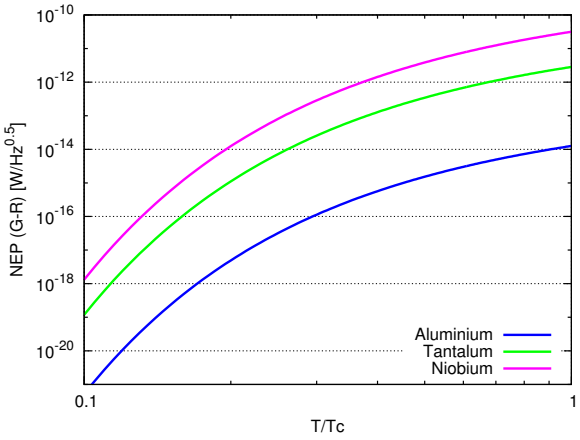

Figure 2.8: The temperature dependence of the generation-recombination limited NEP of aluminum, tantalum, and niobium films.

in width, and 100 nm in thickness was used. The quasi-particle lifetime of aluminum, tantalum, and niobium as a function of temperature is shown in the right panel of Fig. 2.7.

Figure 2.8 shows the generation-recombination noise limited NEP of aluminum, tantalum, and niobium as a function of temperature. Using Eqs. 2.13 and 2.14, it is shown that the generation-recombination noise limited NEP decreases exponentially with decreasing temperature: $NEP_{gr} \propto e^{-\Delta/kT}$.

In addition to the generation-recombination noise, two types of the additional noise have been known. In case of an amplitude readout, the system noise is limited by a HEMT low-noise amplifier.

Recently, a low-noise superconducting amplifier with niobium titanium nitride has been developed (Eom et al., 2012). Nitride superconductors, such as titanium nitride and niobium titanium nitride, are a large resistance, low dissipation medium. It also shows large non-linearity that can be used to realize a broadband quantum-limited parametric amplifier, which is important component to improve the sensitivity of MKIDs with amplitude readout.

On the other hand, in case of phase readout, excess noise is caused by two level systems (TLS) in dielectric material (Phillips, 1987). The TLS is considered to be located in a dielectric wafer and oxidized surface of the superconductor. To reduce the TLS noise, many studies have been reported (Noroozian et al., 2009; Gao et al., 2008a,b).

2.3 Millimeter-Wave Camera Optics

2.3.1 Coupling Type

There are two methods to couple photons to a detector from the optical system of the telescope; planar antenna coupled and directly coupled from air (absorber). In this section, these two coupling systems and their focusing elements with a horn and a dielectric lens are discussed from the view point of their beam pattern, ease of detector coupling, cost and ease of fabrication.

Absorber Coupling

To directly couple the photons to a detector from the telescope, there are various types of detectors such as TES and lumped element kinetic inductance detector (LEKID; Doyle et al. 2008). These devices act as direct photon absorbers. In addition, these devices can be integrated into a compact filled array geometry with high filling factor, and Nyquist sampling is allowed. Absorber type detectors produce the isotropic beam. Therefore, their system requires high-quality cold aperture stops to reduce the stray light and the input noise. In consequence, a cryostat including the cold optics becomes extremely large. For example, SCUBA-2 is a 10000 pixel camera using TES bolometers. The dimensions of the SCUBA-2 cryostat, which consists of 10000 pixel detectors and cryogenic optics, are 2.3 m $\times$ 1.7 m $\times$ 2.1 m, and a weight of 3400 kg (Holland et al., 2013).

Planer Antenna Coupling

A CPW quarter-wave resonator is well matched with a planar antenna that is used to couple photons from the telescope optics to the MKIDs. It is possible to form the detector and the antenna with one superconducting film and one etching process. In general, a planar antenna produces broad beam pattern with symmetrical main beam and low side-lobe level. Therefore, most planar antennas require additional focusing elements for efficient coupling to the telescope optics, such as substrate lenses or feed horns. For the developing of large-format millimeter/sub-millimeter wave cameras, integration density of the detectors, quality of beam patterns, weight, cost and machinability should be considered.

2.3.2 Focusing Elements

Horn Coupling

One advantage of using a feed horn is its high-quality beam patterns. For example, corrugated feed horns have a symmetrical main beam, and achieve low sidelobe level and low cross-polarization level (e.g. Naruse et al. 2009a). Therefore, feed horn array has been widely used for many astronomical observations such as Cosmic Microwave Background experiments (Yoon et al., 2006; Niemack et al., 2010). However, their fabrication method such as electroforming becomes complicated and expensive because the corrugation structure is complicated for large focal-plane arrays.

Lens Coupling

In the case of lens systems, there are two options: a single large lens with multiple antennas (Filipovic et al., 1997) or a single small lens for each antenna. The case of a single large lens with multiple antennas has the following disadvantages: the peak values of the main beam drop, side-lobe levels increase and the beam widths broaden for detector positions away from the lens axis (Naruse et al., 2009b). Optical aberrations also limit the size of the array. In addition, a bigger single lens leads to larger dielectric loss and larger heat capacity. Therefore, lens array systems have several advantages over a single large lens system.

Recently, platelet corrugated horn arrays (Nibarger et al., 2012) and smooth-walled drilled horn arrays (Leech et al., 2012) have been developed. Lens arrays have a few advantages over these horn arrays: 1) a lens array has much smaller volume/mass than a platelet corrugated horn arrays and smooth-walled drilled horn arrays. It is preferable at low temperature of less than 1 K; 2) platelet-corrugated horn arrays require the high-alignment accuracy of many plates, gold plate on the inner surface, and a back short for some detectors. The metal horn arrays have a concern on alignment between detector substrate and the horn at low temperature (< 1 K) because of the different thermal expansion coefficients, especially for a larger array. From these considerations, we adopted the lens array and planar antennas as the optical system for the millimeter and sub-millimeter wave cameras.

2.4 Camera Design of This Thesis

MKIDs are very promising to use for large-format arrays due to their intrinsic frequency multiplexing capability and a good sensitivity for radiation detection from the millimeter-wave to the X-ray. The superconducting aluminum film is suitable for our purpose because the Al-based MKIDs can detect photons at frequencies higher than 90 GHz. Also, high sensitivity with NEP of about 10^{-19} W$/\sqrt{\text{Hz}}$ can be ideally achieved. The optical design of our camera is based on a planar antenna and a dielectric lens array. A planar antenna such as double-slot antenna on a dielectric lens produces a symmetrical beam pattern with low side-lobe level, and its assembly is quite simple. From these considerations, we adopted the lens-antenna coupled MKID as a camera system for millimeter- and submillimeter-wave observations.

3

Development of the Direct Machined Silicon Lens Array

3.1 Introduction

Dielectric materials for substrate lens need to satisfy the following requirements:

1. low dielectric loss in the millimeter and submillimeter-wave bands
2. refractive index close to that of the silicon substrate ($n \sim 3.4$) on which superconducting CPW resonators are patterned to minimize the reflection loss between the substrate and the lens
3. high thermal conductivity
4. possibility to shape the lenses.

The dielectric loss tangent of optical property is an important parameter for lens materials. Figure 3.1 shows an absorption loss in a dielectric lens as a function of a lens thickness. The results of various dielectric loss tangents were shown. As will be noted from Fig. 3.1, larger lens diameter induces higher absorption loss. For example, the dielectric loss tangent should be lower than 10^{-3} to get a high transmittance inside a 3λ (λ is the target wavelength) diameter lens of 95% in the millimeter- and submillimeter-wave band. For these reasons, polycrystalline silicon, alumina (Al_2O_3), and aluminum nitride (AlN) were chosen as dielectric materials for the high refractive index lens. High-purity samples, silicon with 11N, alumina with 4N, and aluminum nitride with above 94% purity, were selected to measure absorption loss as a candidate of the substrate lens.

3.2 Optical Properies of Dielectric Materials

3.2.1 Measurement Setup

A Fourier transform spectrometer (FTS) was used for measurements of the refractive index and the dielectric loss tangent of lens materials. The interferometer is a standard Martin-Puplett type with a polarizing beam splitter, two polarizers, two corner reflectors, and a mercury lamp, as shown in Fig 3.2 (Matsuo et al., 1998). One of the corner reflectors is driven continuously to change the optical pass length. Figure 3.3 shows a block diagram of the Martin-Puplett type FTS. An InSb bolometer was used for the measurements.

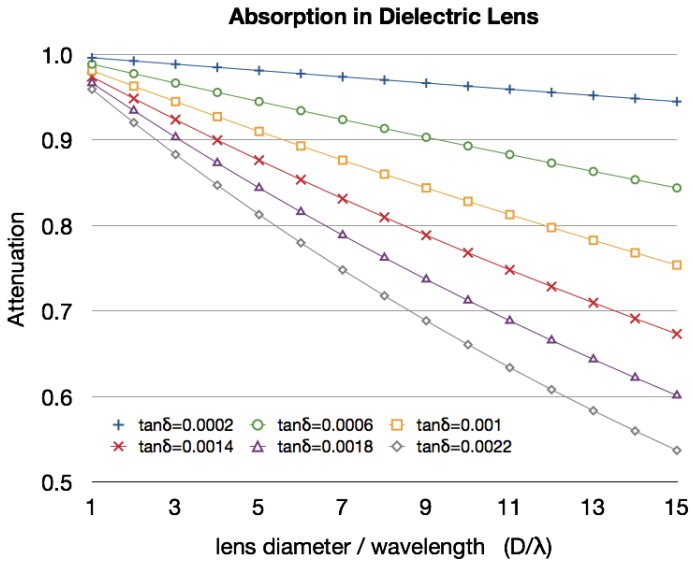

Figure 3.1: Absorption loss in a dielectric lens as a function of a lens thickness. The results of various dielectric loss tangents were shown. In this calculation, the lens form was assumed to be hemispherical shape.

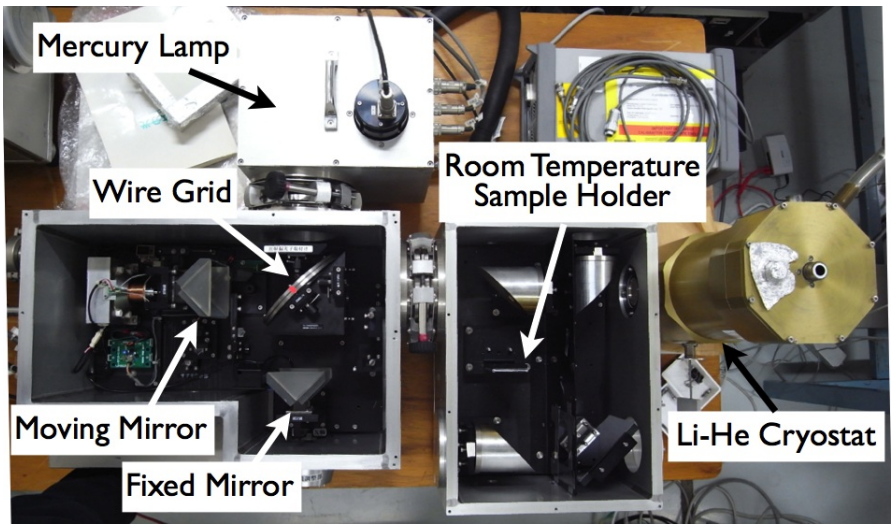

Figure 3.2: A Martin-Puplett type Fourier transform spectrometer for optical property measurement of various lens materials (Matsuo et al., 1998).

Figure 3.4 shows a photograph of the inside of the liquid-helium cryostat. The left panel of Fig. 3.4 shows a rotating sample holder mounted on the 4 K cold stage. The holder has four holes, one is used for reference signal, and three holes are used for dielectric sample materials. The right panel of Fig. 3.4 shows a side view of the sample holder. The signals passed through a dielectric material (sample measurement) or through-hole

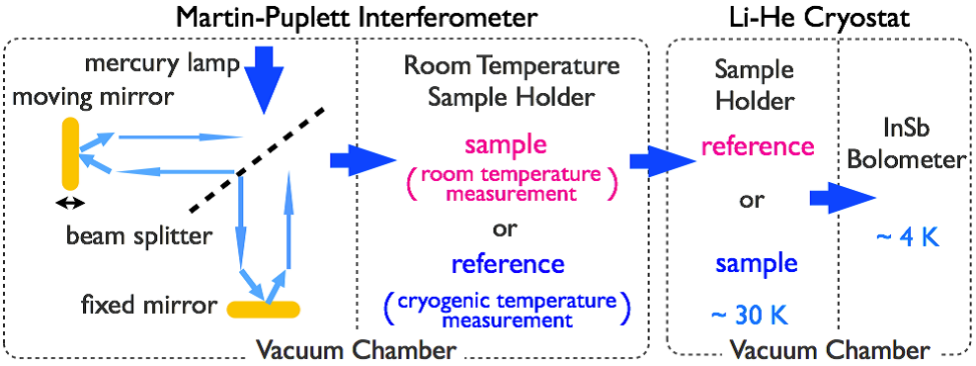

Figure 3.3: A block diagram of the Martin-Puplett type Fourier transform spectrometer. Pink- and blue-letters indicate the setup of ambient and cryogenic temperature measurements, respectively.

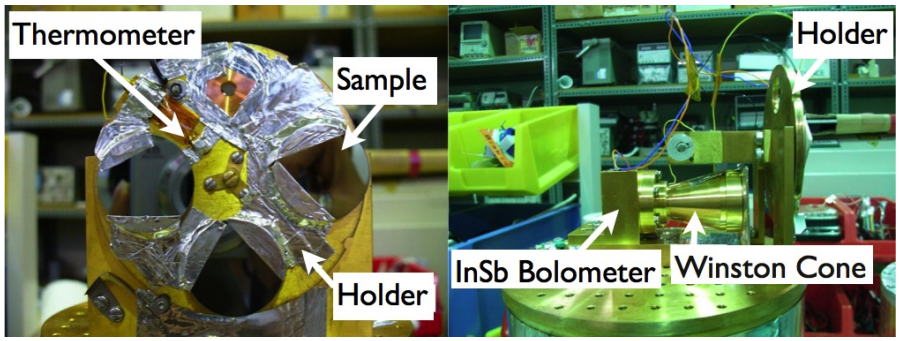

Figure 3.4: Photographs of the inside of the liquid-helium cryostat. (*Left*) The sample holder mounted on the 4 K cold stage. The holder has four holes, one is used for reference signal, and three holes are used for a sample materials. (*Right*) Side view of the sample holder. The signals passed through sample or through-hole (reference) at the holder. Then, the signals were focused with the winston cone and detected by an InSb bolometer.

(reference measurement) at the holder. Then, the signals were focused with the winston cone and detected by an InSb bolometer.

The Martin-Puplett type FTS was designed to optimize millimeter and terahertz-wave efficiencies with a short optical path and a large beam size to minimize diffraction losses (Matsuo et al., 1998). The FTS was operated in rapid scan speed of 8 mm/s to remove low frequency fluctuations of the detector noise. A high frequency resolution of 0.5 cm^{-1} (15 GHz) was selected to obtain the interference fringe of high refractive index materials. Approximately 30 continuous scans were integrated to get enough signal-to-noise ratio. The repeatability of the detector response was measured by repeated transmittance measurements of the dielectric material samples and showed a sensitivity fluctuation of less

than 2%.

3.2.2 Data Analysis

The refractive index and dielectric loss tangent are derived from an analysis method presented by Loewenstein & Smith (1971) and Tsunawaki et al. (2004). The interference fringes corresponding to the sample thickness are observed when heterochromatic light is passed through a plane parallel dielectric sample and then dispersed. In other words, the fringes are caused by the multiple reflections of light within the sample. To determine a refractive index and a dielectric loss tangent of dielectric materials, a transmitted energy is needed. At first, the transmitted amplitude a_t is given by

$$\begin{aligned} a_t &= a_{t1} + a_{t2} + a_{t3} + \cdots \cdots \\ &= t^2\mu e^{j\delta} + r^2t^2\mu^3 e^{j3\delta} + r^4t^2\mu^5 e^{j5\delta} + r^6t^2\mu^7 e^{j7\delta} + \cdots \cdots, \end{aligned} \tag{3.1}$$

where

$$\delta = 2\pi nd\nu\cos\theta, \tag{3.2}$$

$$\mu = \exp(-2\pi\nu kd/\cos\theta). \tag{3.3}$$

δ and μ are phase difference and attenuation rate within a sample, respectively. θ, k, n, d and ν correspond to refracting angle, extinction coefficient, refractive index of sample, sample thickness and frequency, respectively. r and t are Fresnel coefficients for reflection and transmission at a single surface. These are defined as

$$r^2 = \frac{(n-1)^2}{(n+1)^2}. \tag{3.4}$$

$$t^2 = \frac{4n}{(n+1)^2}. \tag{3.5}$$

Note that r^2 and t^2 meet the following equation; r^2+t^2 =1. The transmitted energy T_S is given by squaring the amplitude:

$$\begin{aligned} T_S &= a_t a_t^* \\ &= \frac{t^4\mu^2}{1-r^4\mu^4} + \frac{2r^2t^4\mu^4}{1-r^4\mu^4}\cos 2\delta + \frac{2r^4t^4\mu^6}{1-r^4\mu^4}\cos 4\delta + \frac{2r^6t^4\mu^8}{1-r^4\mu^4}\cos 6\delta \cdots\cdots \end{aligned} \tag{3.6}$$

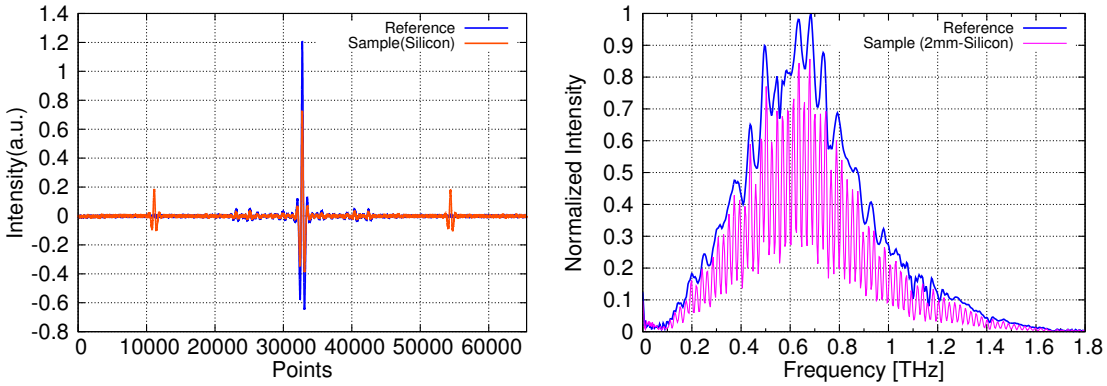

Figure 3.5: (*Left*) Measured interferograms. Blue and orange lines correspond to the reference and sample (2-mm thick silicon) signals, respectively. Interferogram of sample has the peak due to the multiple reflections inside the sample. (*Right*) The frequency spectra of reference and sample. These spectra were obtained by the Fourier transform of the interferograms. From spectrum of reference, InSb bolometer has high sensitivity for the frequency range of 0.2 — 1.6 THz.

Let $I(h)$ be a heterochromatic interference fringe called interferogram, and let $B(\sigma)$ be a spectrum intensity as a function of wavenumber σ. Here h is a optical pass length. An interferogram is observed when the two beams are combined together. The relationship between $I(h)$ and $B(\sigma)$ is as follows.

$$I(h) - I(0)/2 = 2\int_0^\infty B(\sigma)\cos(2\pi\sigma h)d\sigma. \tag{3.7}$$

$$B(\sigma) = 2\int_0^\infty [I(h) - I(0)/2]\cos(2\pi\sigma h)dh. \tag{3.8}$$

The term of $I(0)/2$ is bias component of a interferogram. From these equations, spectrum response $B(\sigma)$ is obtained by the Fourier transform of the interferogram $I(h)$. The left panel of Fig. 3.5 shows the measured interferogram of sample and reference. As shown in the results, interference peaks derived from multiple reflections within a sample were clearly detected in interferogram of sample but not in reference. The right panel of Fig. 3.5 shows the frequency spectra of the reference and a sample. These spectra were obtained by the Fourier transform of the measured interferograms. The interference fringes of a sample spectrum corresponding to the thickness of the flat samples are caused by multiple reflections within the samples. The frequency spectrum of reference signal corresponds to the detector response. From spectrum of reference, the InSb bolometer has

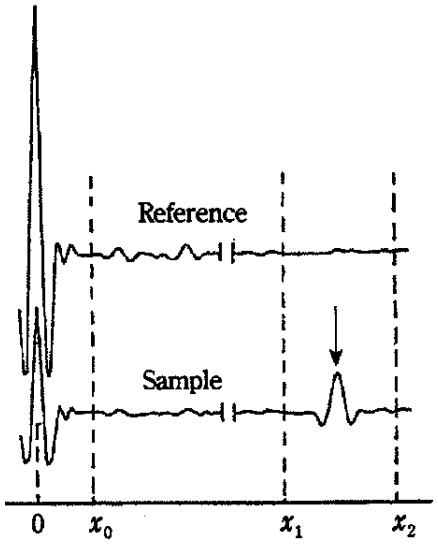

Figure 3.6: Reference and sample interferograms for a material (Tsunawaki et al., 2004). The arrow indicates the peak that contain detailed information about multiple reflections inside a sample. x_0, x_1 and x_2 show the range of the Fourier transform.

high sensitivity for the frequency range of 0.2 — 1.6 THz.

Figure 3.6 shows the reference and sample interferograms for a material (Tsunawaki et al., 2004). The arrow indicates the peak that contain detailed information about multiple reflections inside a sample. The left and middle panels of Fig. 3.7 show the calculated transmission spectrums of $FT[I_S(x_1)]/FT[I_R(x_1)]$ and $FT[I_S(x_2)]/FT[I_R(x_2)]$. S and R correspond to the sample and reference, and x_1 and x_2 showed the range of the Fourier transform as shown in Fig. 3.6. The transmission spectrum of $FT[I_S(x_2)]/FT[I_R(x_2)]$ includes the Fabry-Perot fringes which derived from the peak of sample interferogram. The Fabry-Perot fringes can be isolated by using a following equation,

$$T = \frac{FT[I_S(x_2)]}{FT[I_R(x_2)]} - \frac{FT[I_S(x_1)]}{FT[I_R(x_1)]}. \tag{3.9}$$

The fringe spacing depends only upon the sample thickness and the refractive index. The refractive index of sample is given by

$$n = \frac{1}{2d\Delta k}, \tag{3.10}$$

where d is a sample thickness and Δk is a fringe spacing of zero crossings as a function

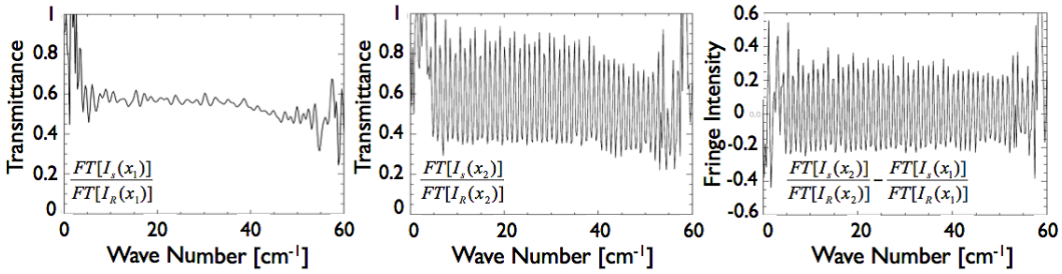

Figure 3.7: (*Left*) Calculated result of $FT[I_S(x_1)]/FT[I_R(x_1)]$. The transmission spectrum does not include the Fabry-Perot fringes. (*Middle*) Calculated result of $FT[I_S(x_2)]/FT[I_R(x_2)]$. The transmission spectrum includes the Fabry-Perot fringes. (*Right*) Calculated result of $FT[I_S(x_2)]/FT[I_R(x_2)] - FT[I_S(x_1)]/FT[I_R(x_1)]$. This spectrum provides only information about Fabry-Perot fringes.

of wavenumber. The precise measurements of the sample thickness and zero-crossing of Fabry-Perot fringes are important for accurate determination of the refractive index of the sample.

On the other hand, the fringe amplitude depends also on the absorption coefficient. First, background spectrum T_0, which is obtained by the Fourier transform of an interferogram up to point 0 (x_0), is defined as

$$T_0 = \frac{FT[I_S(x_0)]}{FT[I_R(x_0)]}. \tag{3.11}$$

The relation between the background spectrum T_0 and the first term of the transmitted energy T_S is defined by using Eq. 3.6 as follow,

$$T_0 = \frac{t^4\mu^2}{1 - r^4\mu^4}. \tag{3.12}$$

Deforming the Eq. 3.12, a following equation is obtained,

$$r^4\mu^4 + \frac{t^4}{T_0}\mu^2 - 1 = 0. \tag{3.13}$$

The attenuation rate μ is obtained by solving the Eq. 3.13. Using the Beer-Lambert law, the absorption coefficient α is determined by the following equation,

$$\alpha = -\ln(\mu^2)/d. \tag{3.14}$$

Finally, the dielectric loss tangent (tan δ) is calculated from,

$$\tan\delta = \frac{\alpha}{2n\pi k}, \tag{3.15}$$

where n and k are the refractive index and the wavenumber, respectively. It is possible to determine both refractive index and dielectric loss tangent from single transmittance measurement of lens sample.

The analysis for determining a refractive index and dielectric loss tangent is summarized as follows.

1. Positions of x_0, x_1 and x_2 of interferogram are determined, as shown in Fig. 3.6.
2. The frequency spectrums at each position are obtained by the Fourier transform of the interferograms.
3. The equation of $FT[I_S(x_2)]/FT[I_R(x_2)]$-$FT[I_S(x_1)]/FT[I_R(x_1)]$ is calculated to obtain a Fabry-Perot fringes.
4. The wavenumber at zero-cross positions of Fabry-Perot fringe are determined to get the refractive index of lens sample.
5. The refractive index is calculated by using Eq. 3.10.
6. The attenuation rate μ is derived from Eq. 3.13. The absorption coefficient α is determined by using μ and sample thickness, as shown in Eq. 3.14.
7. By using Eq. 3.15, transform the absorption coefficient into the dielectric loss tangent of the lens sample.

3.2.3 Temperature and Purity Dependence of Transmittance

Figure 3.8 shows the temperature and sample-purity dependence of transmittance. A high-purity (4N purity) alumina was used for temperature dependence measurements. Also 4N (AJPF) and 2N (A9951LD) purity alumina were used for purity dependence measurements. The high transmittance is obtained by cooled and high-purity samples. The measured transmittance indicates as follows.

1. The dielectric loss is reduced at low temperature.

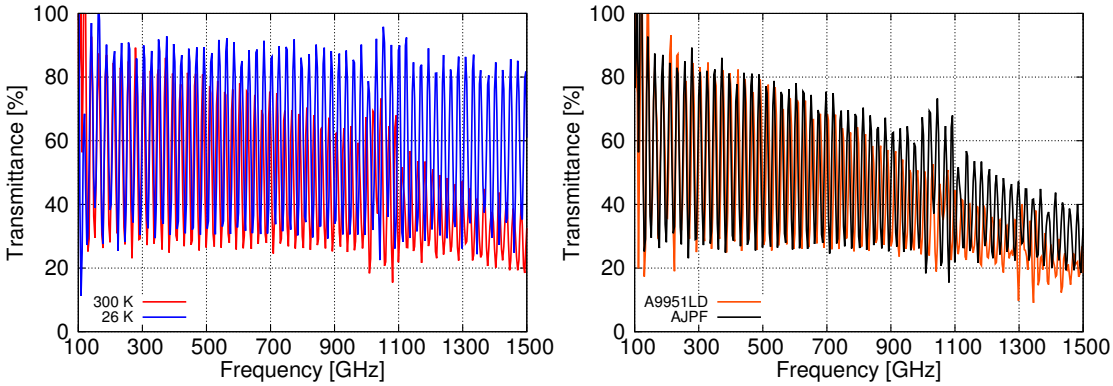

Figure 3.8: (*Left*) Temperature dependence of transmittance. The sample was high-purity (4N purity) alumina. (*Right*) Sample purity dependence of transmittance at ambient temperature. Black and orange lines correspond to the 4N (AJPF) and 2N (A9951LD) purity alumina, respectively.

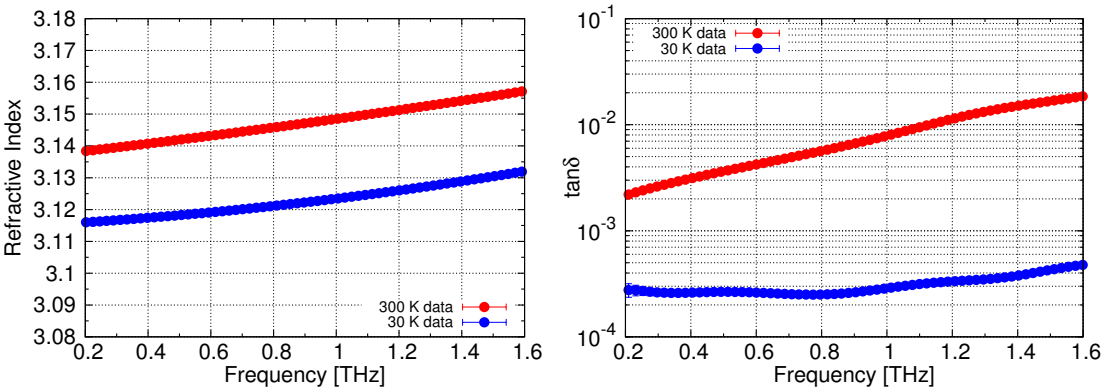

Figure 3.9: (*Left*) Refractive index and (*Right*) dielectric loss tangent of the high-purity (4N purity) alumina. Blue and red lines correspond to 30 K and 300 K data, respectively. According to the results, the refractive index was slightly changed by temperature and the dielectric loss tangent was drastically reduced at cryogenic temperature.

2. High-purity samples have lower loss than low-purity ones.

Figure 3.9 shows the refractive index and dielectric loss tangent of the high-purity (4N purity) alumina. Blue and red lines correspond to 30 K and 300 K data, respectively. The data were taken by fitting the measured refractive indices and dielectric loss tangents which were derived from the analysis shown in previous section. According to the results, the refractive index was slightly changed by temperature and the dielectric loss tangent was drastically reduced at cryogenic temperature.

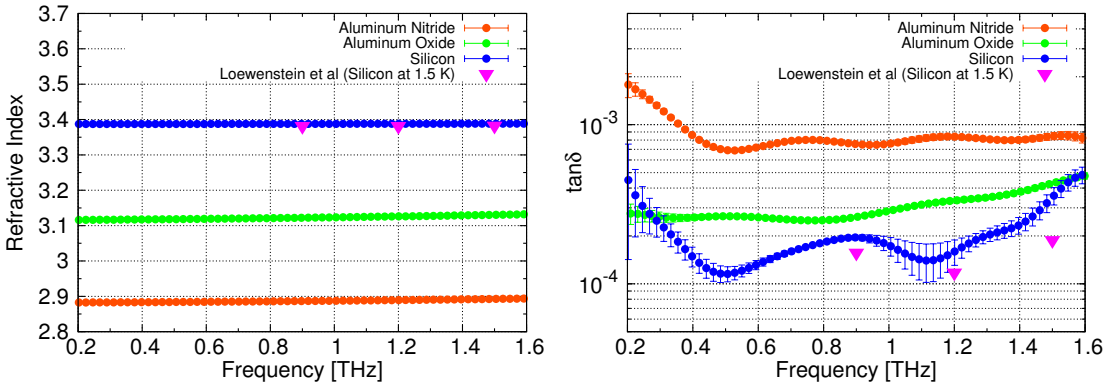

Figure 3.10: Measurements of the optical properties of lens materials. (*Left*) Refractive index and (*Right*) dielectric loss tangent of polycrystalline silicon (11N purity), alumina (4N purity), and aluminum nitride ($> 94\%$ purity). Measured temperature was 15 K. Measurement results are in good agreement with the other data (Loewenstein et al., 1973).

3.2.4 Optical Properties of Samples

Figure 3.10 shows the measurement results of the refractive index and the dielectric loss tangent at 15 K. The measured data are in good agreement with the other data (Loewenstein et al., 1973). The error bars are 1-σ error, which was determined by the multiple transmittance measurements. Large error bars around 1 THz were caused by absorption of water vapor in the air.

High-purity silicon and alumina are suitable for focusing devices because of their high-refractive index, high thermal conductivity, and low dielectric loss tangent in the millimeter- and submillimeter-wave range. In our camera, high-purity (11N purity) polycrystalline silicon is the most suitable for lens material because the high-resistivity silicon substrate was used for the MKID array. Absorption loss inside the 3λ- (= 4.09 mm) diameter lens for the 220-GHz band is only 1% at cryogenic temperatures.

Polycrystalline silicon has a few advantages over single-crystalline silicon for the substrate lens:

1. it is easier to process polycrystalline silicon than single-crystalline silicon, because single-crystalline silicon breaks easily along crystal orientation.

2. polycrystalline silicon is cheaper than single-crystalline silicon.

However, in case of silicon, the high refractive index in the millimeter/submillimeter-wave region leads to a reflection at each silicon/vacuum interface of approximately R

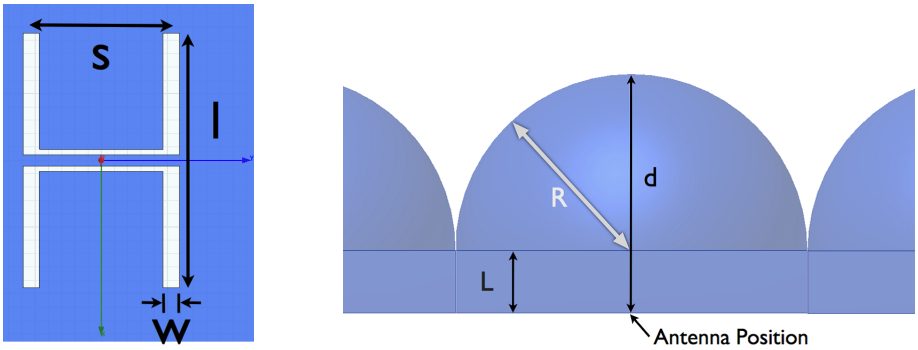

Figure 3.11: (*Left*) A schematic of a double-slot antenna. s, l and w correspond to the slot separation, antenna length and antenna width, respectively. (*Right*) Shape and design parameters of an extended hemispherical lens. L, R, and d correspond to the extension thickness, lens radius, and the distance between the antenna and the lens top, respectively.

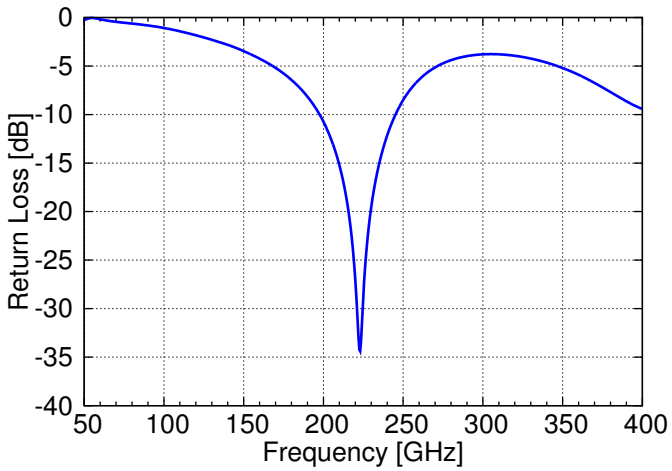

Figure 3.12: The return loss (S_{11}) of a double-slot antenna in the 220-GHz band calculated with the 3-D full-wave electromagnetic field simulator HFSS.

= $[(n - 1)/(n + 1)]^2 \approx 30\%$ per surface. Therefore, when we use high refractive index materials, anti-reflection (AR) coatings are critical. In chapter 6, two types of AR coatings for silicon and alumina lenses are discussed.

3.3 Optical Design of Lens and Planar Antenna

3.3.1 Double Slot Antennas

Double-slot antennas have been widely used in millimeter and submillimeter-wave range, because of their symmetrical beam patterns and capability of polarization measurements (Filipovic et al., 1993; Chattopadhyay & Zmuidzinas, 1998; Van der Vorst, 1999). In addition, a double-slot antenna on a substrate lens produces a symmetrical beam pattern with low side-lobe level, and its assembly is quite simple. Thus, this configuration has been used for astronomical observations (Zmuidzinas & LeDuc, 1992; Arnold et al., 2012).

The double-slot antenna is patterned at the end of the quarter-wave resonator, which is on the opposite side of the feed line. According to Filipovic et al. (1993), the far-field beam patterns of the double-slot antennas are calculated assuming a sinusoidal magnetic current distribution on the slot antenna. The mean wavelength in the double-slot antennas is defined as

$$\lambda_m = \frac{\lambda_0}{\sqrt{\epsilon_m}}, \tag{3.16}$$

where ϵ_m is a mean dielectric constant and which is given by (1 + ϵ_r)/2. The ϵ_r is the dielectric constant of a silicon wafer and equals approximately 11.7. The normalized far-field beam pattern of double-slot antennas is described by the following equation (Filipovic et al., 1993),

$$\frac{\sin\theta[\cos(k_{diel} l\cos\theta) - \cos(k_m l)]}{(k_m)^2 - (k_{diel})^2\cos^2\theta} \cdot \cos(k_{diel}\frac{s}{2}\sin\theta\cos\phi), \tag{3.17}$$

where l and s correspond to the antenna length and antenna separation, respectively. k_{diel} and k_m are defined by

$$k_{diel} = \frac{2\pi}{\lambda_{diel}}. \tag{3.18}$$

$$k_m = \frac{2\pi}{\lambda_m} = \frac{2\pi}{\lambda_0}\cdot\sqrt{\frac{1+\epsilon_r}{2}}. \tag{3.19}$$

The left panel of Fig. 3.11 shows a schematic of a double-slot antenna. s, l and w correspond to the slot separation, antenna length and antenna width, respectively. The geometrical parameters of the double-slot antenna were optimized for a target frequency to minimize return loss (S_{11}) and to achieve symmetrical beam patterns and low side-

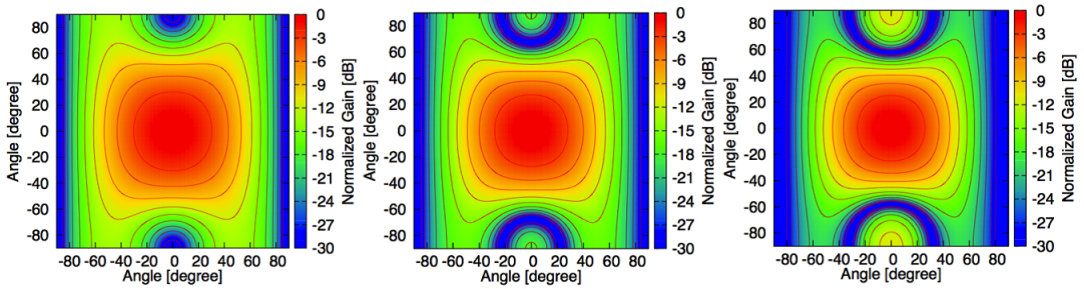

Figure 3.13: The simulated beam patterns of the double-slot antenna at (*Left*) 200 GHz, (*Middle*) 220 GHz, and (*Right*) 240 GHz. The contours were every 3 dB steps.

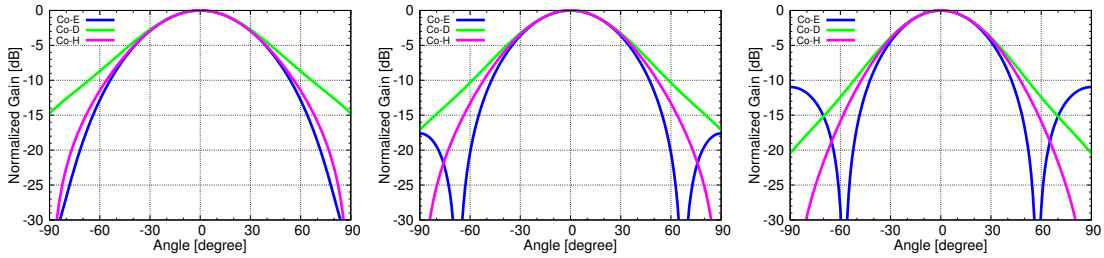

Figure 3.14: Cross section of the beam patterns represented in figure 3.13. Blue, green and pink lines correspond to the E-, D- and H-plane, respectively. The left, middle and right panels correspond to 200 GHz, 220 GHz and 240 GHz patterns.

lobe levels. The return loss (S_{11}) of a double-slot antenna in the 220-GHz band was calculated with a 3-D full-wave electromagnetic field simulator HFSS. The numerical calculations of beam patterns are based on Eq. 3.17 (Filipovic et al., 1993). The optimized parameters for the 220-GHz band were 382 μm in length, 25 μm in width, and 212 μm in slot separation. Figure 3.12 shows the simulated result of the return loss (S_{11}). The antenna bandwidth ($-$ 10 dB return loss level) was around 20%. Figure 3.13 shows the two-dimensional simulated far-field beam patterns of the double-slot antenna at 200, 220 and 240-GHz, and its cross section are displayed in Fig. 3.14. The horizontal and vertical axes of two-dimensional maps correspond to the one-dimensional patterns of H- and E-planes, respectively. The half-power beam width (HPBW) of the beam patterns at 220 GHz is about 60 degree.

3.3.2 Design of Extended Hemispherical Lens

We used a silicon hemispherical lens with a silicon extension to form an extended hemispherical lens to increase the gain of the antenna and to produce the circular symmetry

beam patterns in combination with a double-slot antenna. The design of an extended hemispherical silicon lens was based on Filipovic et al. (1993). The equation of an ellipse in the xy-plane is,

$$\left(\frac{x}{a}\right)^2 + \left(\frac{y}{b}\right)^2 = 1, \tag{3.20}$$

where a and b correspond to a minor and major axes of ellipse, respectively. The geometrical foci of ellipse are located at $y = \pm c$, and c is defined by,

$$c = \sqrt{b^2 - a^2}. \tag{3.21}$$

Also, the eccentricity e of the ellipse is expressed as a function of the refractive index n of lens by the following equation.

$$e = \frac{\sqrt{b^2 - a^2}}{b} = \frac{1}{n}. \tag{3.22}$$

Therefore, b and c are represented as follows.

$$b = \frac{a}{\sqrt{1 - \frac{1}{n^2}}}. \tag{3.23}$$

$$c = \frac{b}{n} = \frac{a}{n\sqrt{1 - \frac{1}{n^2}}}. \tag{3.24}$$

Figure 3.11 shows the shape and design parameters of the extended hemispherical lens. The distance from the top of an extended hemisphere to the bottom of its extension, which corresponds to d in Fig. 3.11, is equal to R + L, where R and L are the lens radius and the extension thickness, respectively. Additionally, the distance from the top of an ellipse to its focus is equal to b + c. These distances must be equal to form the extended hemispherical lens. Therefore, the extension thickness L is expressed as follows.

$$L = b + c - R. \tag{3.25}$$

A minor axis of ellipse a is expressed as a function of the radius of a hemispherical lens R: a=gR. The parameter g is optimized to adjust the surface geometry of the elliptical and the extended hemispherical lens. Therefore, b, c and L are expressed as functions

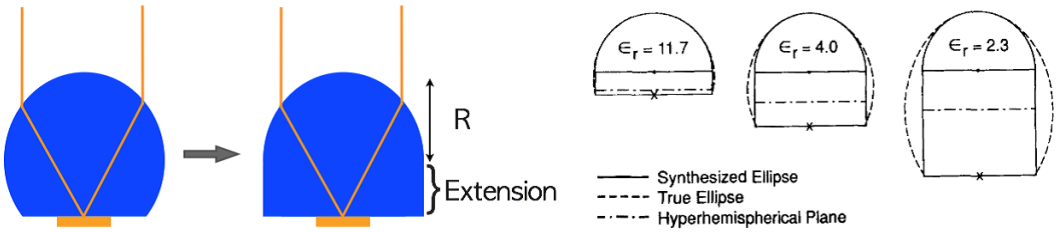

Figure 3.15: (*Left*) Different types of dielectric lens configurations. Left is a true ellipse lens, and right is an extended hemispherical lens. (*Right*) Various types of lenses with a hemispherical lens and a planar plate. (Filipovic et al., 1993). Solid, narrow-dash and wide-dash lines correspond to the extended hemispherical, true ellipse and hyper-hemispherical lenses, respectively. Dielectric constant of ϵ_r=2.3, 3.8 and 11.7 correspond to the polyethylene, quartz and silicon. The extended hemisphere lens is a very good geometrical approximation to an elliptical lens at high refractive index such as silicon.

of g, R and n,

$$b = \frac{gR}{\sqrt{1-\frac{1}{n^2}}}, c = \frac{gR}{n\sqrt{1-\frac{1}{n^2}}}, \tag{3.26}$$

$$L = b + c - R = \left(\frac{g}{\sqrt{1-\frac{1}{n^2}}} + \frac{g}{n\sqrt{1-\frac{1}{n^2}}} - 1 \right) R. \tag{3.27}$$

In case of a silicon lens, the fitted value is g∼1.03 (Filipovic et al., 1993). From Eq. 3.27, the corresponding extension thickness at synthesized elliptical position is L/R∼0.39. The left panel of Fig. 3.15 shows a true ellipse lens and an extended hemispherical lens. As shown in the right panel of Fig. 3.15, the extended hemisphere lens is a very good geometrical approximation to an elliptical lens at high refractive index such as silicon (Filipovic et al., 1993).

In conclusion of this section, the advantages of using an extended hemispherical lens are summarized as follows.

1. A double-slot antenna on an extended hemispherical lens produces a symmetrical beam pattern with low side-lobe level.

2. Its assembly is quite simple.

3. The dielectric half-space increases front-to-back ratio to $\epsilon^{3/2}$: 1 (Filipovic et al., 1993). In the case of silicon, the front-to-back ratio is improved to approximately

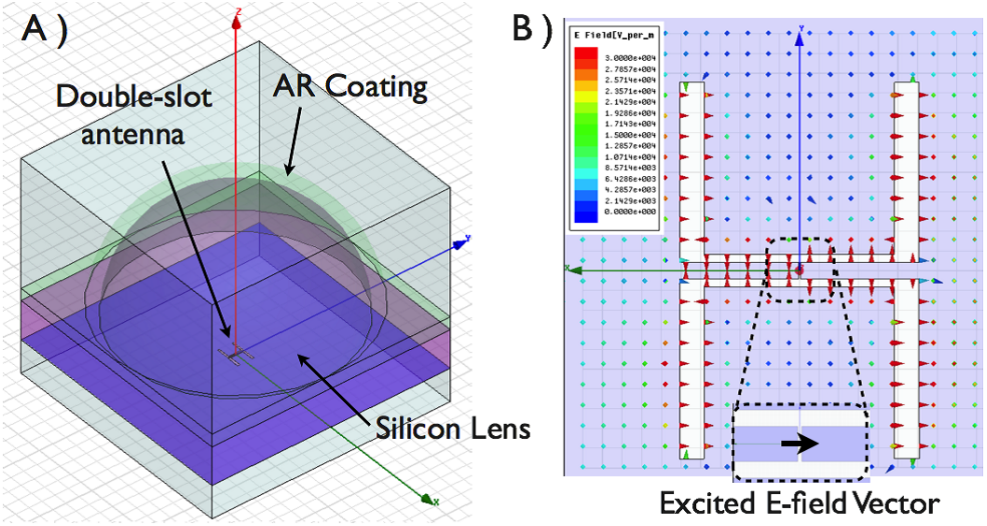

Figure 3.16: (**A**) Simulated model of an extended hemispherical silicon lens antenna with HFSS. The double-slot antenna is located at the focus of the antireflection coated silicon lens. (**B**) Electric field distribution of a double-slot antenna. Color arrows showed the electric field inside the slots, and black arrow indicates the excited electric field vector.

10:1 due to its high dielectric constant.

Simulation Model

To determine the parameters such as lens diameter and an extension thickness, the far-field beam patterns of an extended hemispherical silicon lens fed by a double-slot antenna were calculated with HFSS. The right panel of Fig. 3.11 shows the shape and design parameters of the extended hemispherical lens. Here L and R correspond to the extension thickness and the lens radius, respectively. The left panel of Fig. 3.16 shows a simulated model of an extended hemispherical silicon lens fed by a double-slot antenna with HFSS. The model consists of silicon lens (purple part), perfect matching anti-reflection coating (green part) and double-slot antenna which is located at the focus of the lens. The right panel of Fig. 3.16 shows the electric field inside the slots. The arrow size indicates the magnitude of an electric field.

Half-Power Beam Width at 220 GHz

Figure 3.17 shows the simulated half-power beam width (HPBW) of various lens diameter as a function of extension thickness. When the extension thickness becomes large,

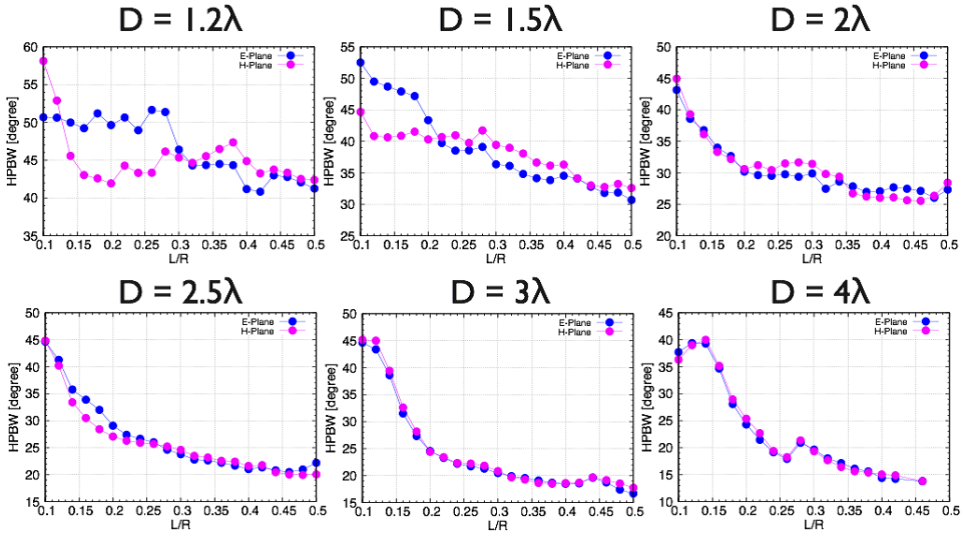

Figure 3.17: Simulated half-power beam width of various lens diameter as a function of extension thickness. Blue and pink points correspond to the E- and H-plane, respectively.

the beam width progressively narrows in every lens diameter. In case of 1.2 λ (λ : the target wavelength) diameter lens, symmetrical beam patterns are obtained when the extension thickness is approximately L/R = 0.35 and higher than 0.44. Also in case of the 1.5 λ diameter lens, symmetrical beam patterns are obtained when the extension thickness higher than L/R = 0.22. In case of 2 $-$ 4 λ lenses, the extension thickness of L/R = 0.1 to 0.5 is efficient.

Beam Patterns at 220 GHz

Figure 3.18 shows simulated beam patterns of various lens diameter as a function of extension thickness. The lens diameters of 1.2, 2 and 3 λ are displayed. The extension thickness is optimized considering the beam pattern quality, such as sidelobe level and symmetry of the main beam. As shown in Fig. 3.17, the mainlobe of beam patterns gradually narrows when the extension thickness becomes large. The first sidelobe levels of every lens were varied from $-$ 15 dB to less than $-$ 25 dB. In the condition of around L/R = 0.34 to 0.36 the sidelobe and cross-polarization levels were minimized, and the condition was chosen for the our camera.

Figure 3.19 shows the relation between the HPBW and the lens diameter which was normalized by wavelength. In this simulation, the extension thickness was fixed at L/R

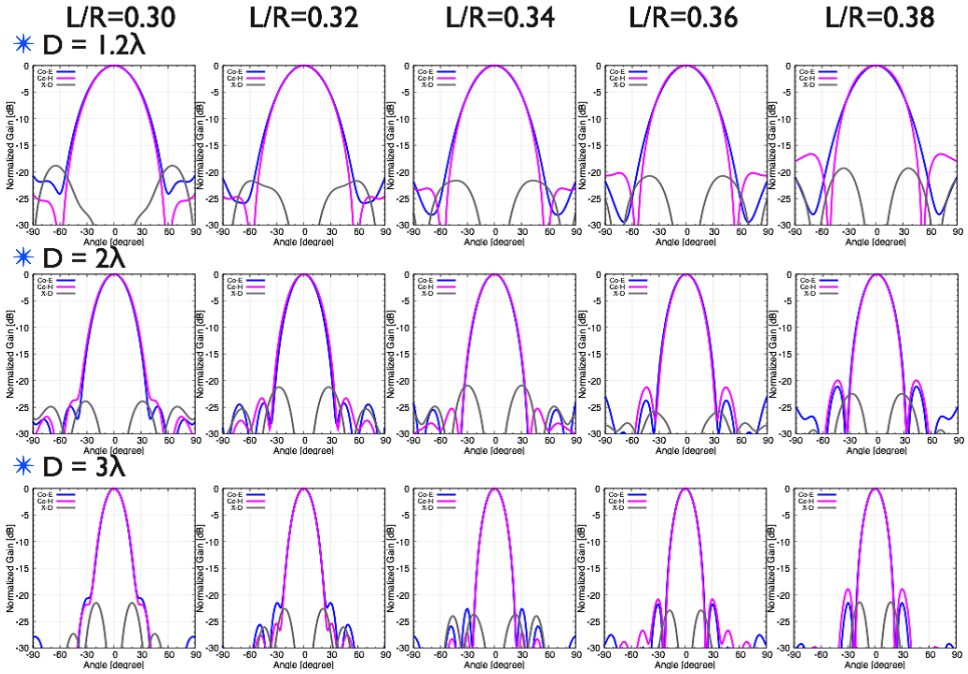

Figure 3.18: Simulated beam patterns of various lens diameters as a function of extension thickness. Blue, pink and gray lines correspond to the co-polarization of E- and H-planes and the cross-polarization of D-plane, respectively. In the condition of around $L/R = 0.34$ to 0.36 the sidelobe was minimized.

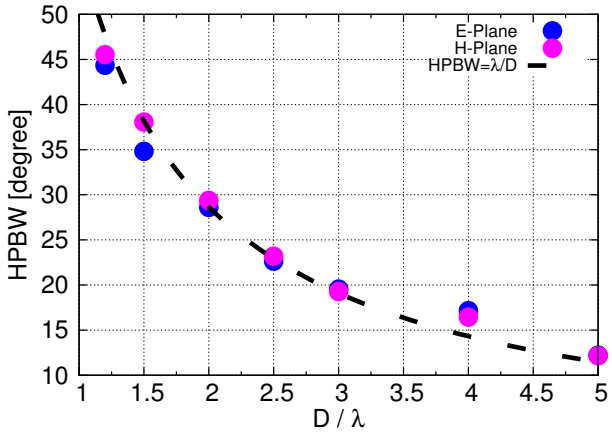

Figure 3.19: Simulated half-power beam width (HPBW) as a function of lens diameter. The extension thickness was fixed at $L/R = 0.36$. The simulated HPBW follows the relationship of λ/D (black dot line), where λ is the target wavelength and D is the lens diameter.

= 0.36. The HPBW of 1.2, 2 and 3 λ diameter lens were approximately 45, 30 and 20 degree, respectively. The simulated HPBW follows the relationship of λ/D (black dot line), where λ is the target wavelength and D is the lens diameter. For realizing a large

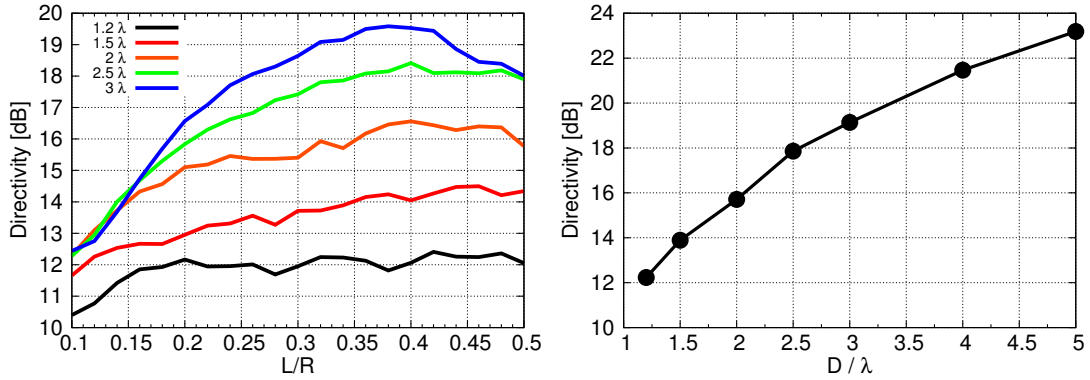

Figure 3.20: (*Left*) Simulated directivity of various lens diameter as a function of extension thickness. In the condition of around L/R = 0.39 the directivity was maximized. (*Right*) The directivity as a function of lens diameter. The extension thickness was fixed at L/R = 0.36.

format camera, small diameter lenses are required to increase the integration density of detectors and to reduce the area of cryogenic part. The increasing the diameter of dielectric lens induces the large-absorption loss and low-integration density. So, the lens diameter and the extension thickness are determined as three times the target wavelength and L/R = 0.36, respectively. The corresponding dimensions of the lens diameter and the extension thickness are 4.09 mm and 0.73 mm, respectively.

Directivity at 220 GHz

The left panel of Fig. 3.20 shows the simulated directivity of various lens diameter as a function of extension thickness, and the right panel of Fig. 3.20 shows the directivity as a function of lens diameter. In this calculations, the extension thickness was fixed at L/R = 0.36. The increasing the diameter of dielectric lens induces the high directivity because the large diameter lens can efficiently concentrate the signals.

In case of 3 λ diameter lens, the calculated directivity has a broad peak of approximately 19.6 dB centered at around L/R = 0.39. The peak position agrees well with a synthesized elliptical position (L/R = 0.39).

Design Summary of 220 GHz-band Lens Array

As discussed in the previous section, the lens diameter and the extension thickness were determined as three times the target wavelength and L/R = 0.36, respectively. Figure

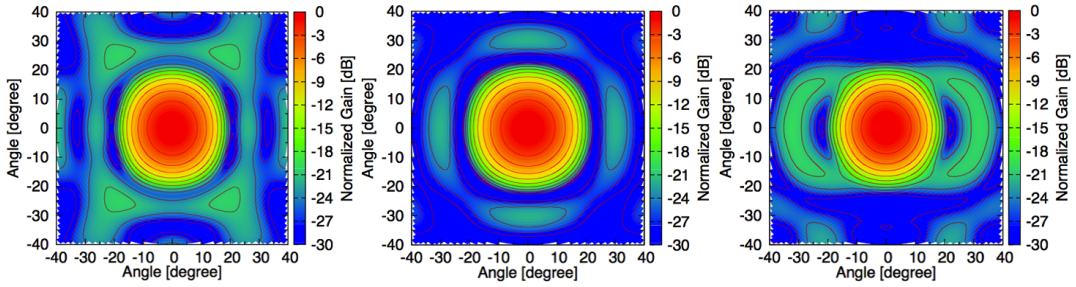

Figure 3.21: The simulated beam patterns of the extended hemispherical silicon lens fed by the double-slot antenna at (*Left*) 200 GHz, (*Middle*) 220 GHz, and (*Right*) 240 GHz. The lens diameter and the extension thickness are three times the target wavelength (3λ) and $L/R = 0.36$, respectively. The contours were every 3 dB steps.

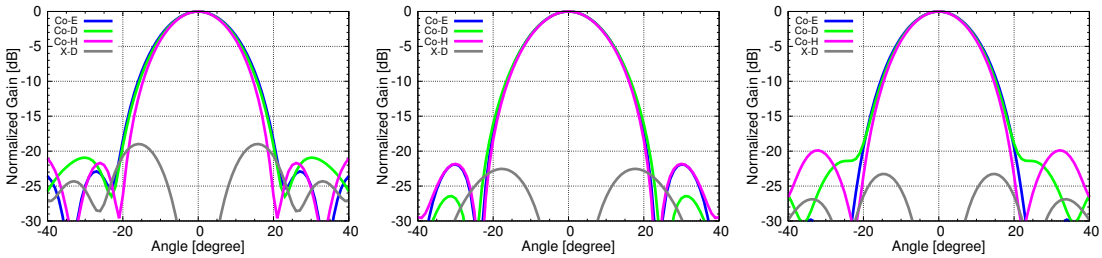

Figure 3.22: Cross section of the beam patterns represented in figure 3.21. Blue, green, pink and gray lines correspond to the co-polarization of E-, D-, and H-planes and the cross-polarization of D-plane, respectively. The left, middle and right panels correspond to 200 GHz, 220 GHz and 240 GHz patterns.

3.21 shows the two-dimensional simulated far-field beam patterns of the extended hemispherical silicon lens fed by the double-slot antenna at 200, 220 and 240-GHz, and its cross section are displayed in Fig. 3.22. The circular symmetry beam patterns and low sidelobe and cross-polarization levels ($-$ 20 dB) were obtained with 20% bandwidth of 200 $-$ 240 GHz. The bandwidth of 20 % correspond to the $-$ 10 dB return loss level of double-slot antenna, as shown in Fig. 3.12. From Fig 3.1, an absorption loss inside the 3λ- (= 4.09 mm) diameter lens for the 220-GHz band is only 1% because the dielectric loss tangent of high-purity silicon was 2×10^{-4} at cryogenic temperatures.

3.4 Optical Design for 440-GHz band

Figure 3.23 shows the simulated return loss (S_{11}) of 440-GHz band double-slot antenna. The antenna bandwidth ($-$ 10 dB return loss level) was approximately 20% of 400 $-$ 480

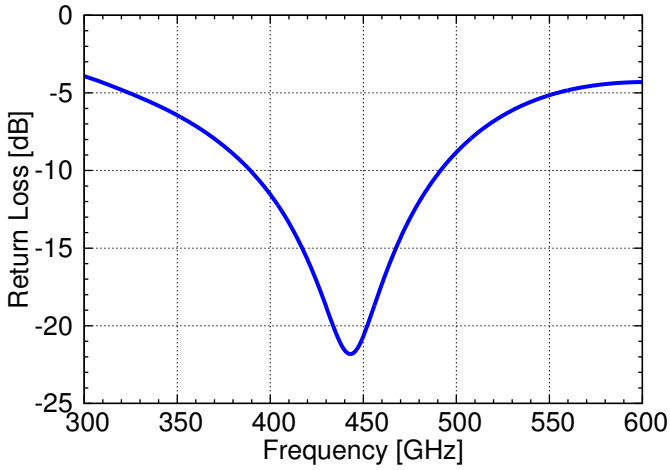

Figure 3.23: The return loss (S_{11}) of a double-slot antenna in the 440-GHz band calculated with the 3-D full-wave electromagnetic field simulator HFSS.

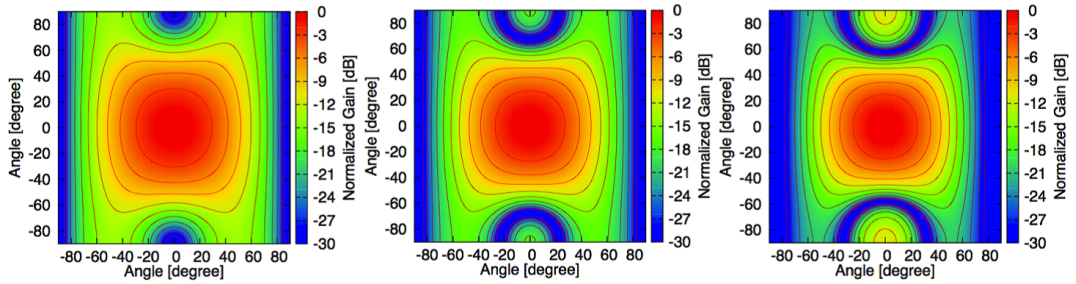

Figure 3.24: The simulated beam patterns of the double-slot antenna at (*Left*) 400 GHz, (*Middle*) 440 GHz, and (*Right*) 480 GHz. The contours were every 3 dB steps.

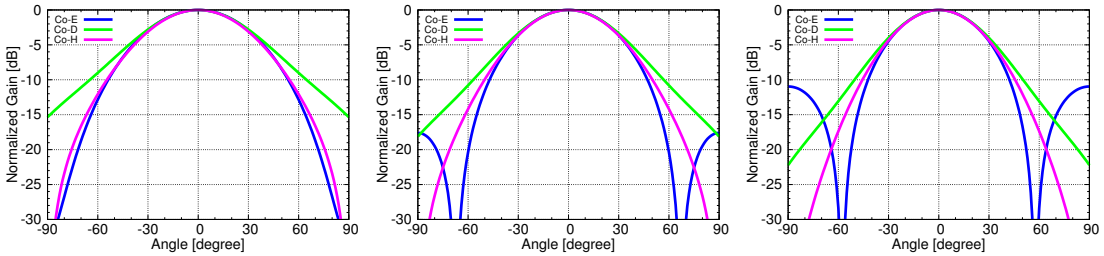

Figure 3.25: Cross section of the beam patterns represented in figure 3.24. Blue, green and pink lines correspond to the E-, D- and H-plane, respectively. The left, middle and right panels correspond to 400 GHz, 440 GHz and 480 GHz patterns.

GHz. The length, width and the slot separation for the 440-GHz band are 198 μm, 16 μm, and 110 μm, respectively. Figure 3.24 shows the two-dimensional simulated far-field beam patterns of the double-slot antenna at 400, 440 and 480-GHz, and its cross section

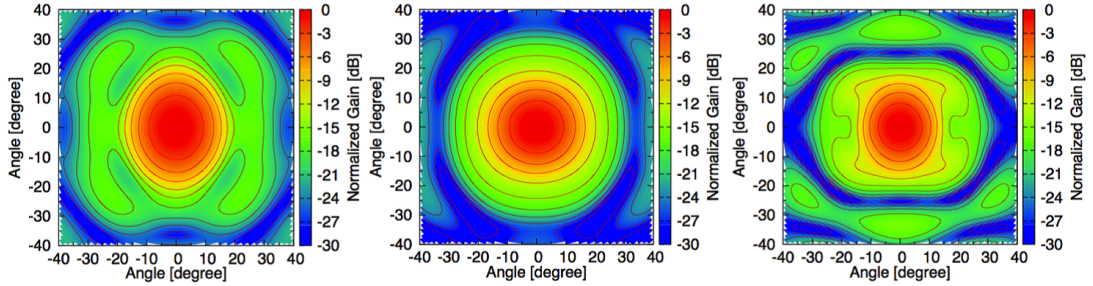

Figure 3.26: The simulated beam patterns of the extended hemispherical silicon lens fed by the double-slot antenna at (*Left*) 400 GHz, (*Middle*) 440 GHz, and (*Right*) 480 GHz. The contours were every 3 dB steps.

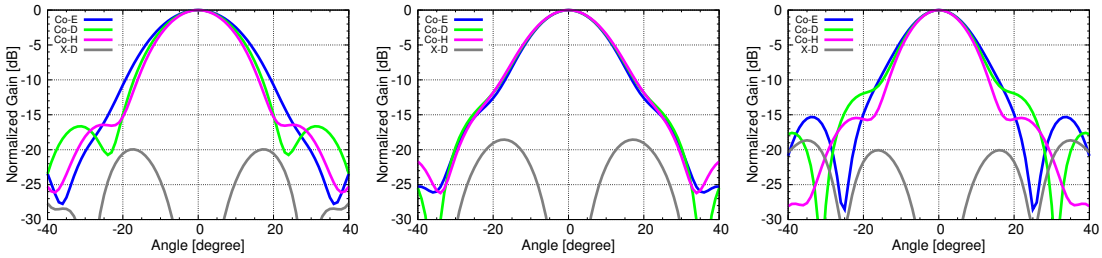

Figure 3.27: Cross section of the beam patterns represented in figure 3.26. Blue, green, pink and gray lines correspond to the co-polarization of E-, D-, and H-planes and the cross-polarization of D-plane, respectively. The left, middle and right panels correspond to 200 GHz, 220 GHz and 240 GHz patterns.

are displayed in Fig. 3.25. The numerical calculations of beam patterns are based on Eq. 3.17. The horizontal and vertical axes of two-dimensional maps correspond to the one-dimensional patterns of H- and E-planes, respectively. The half-power beam width (HPBW) of the beam patterns at 440 GHz is about 60 degree.

The design parameters for 440-GHz band lens array is basically the same as 220-GHz band. The lens diameter and the extension thickness were determined as three times the target wavelength and L/R = 0.36, respectively. The corresponding dimensions of the lens diameter and the extension thickness are 2.04 mm and 0.37 mm, respectively. However, as shown in Fig. 3.29, the extension thickness consists of the support plate and silicon substrate. Therefore, it is impossible to fabricate the extension thickness of 0.37 mm because the thickness of silicon substrate is 0.38 mm. So the extension thickness of 440-GHz array was changed to 0.48 mm (L/R = 0.47) which consists of support plate thickness of 0.1 mm and silicon substrate thickness of 0.38 mm. Figure 3.26 shows the

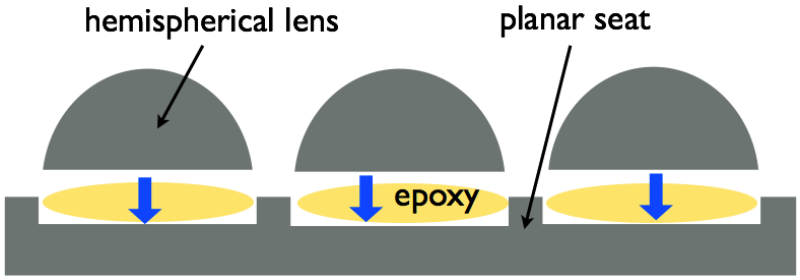

Figure 3.28: A schematic of silicon lens array with individual silicon lenses and planar seat. Lens and seat are attached with epoxy.

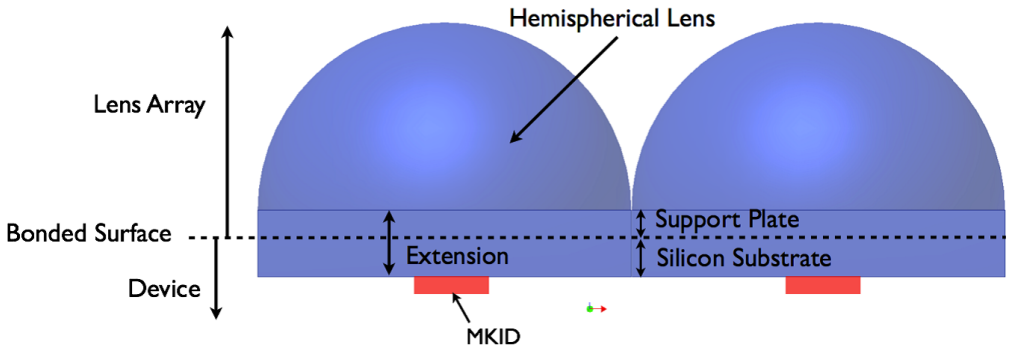

Figure 3.29: Geometry of extended hemispherical silicon lens array coupled to the MKID. The upper part of a dotted line shows the silicon lens array which was machined by a high-speed spindle and the bottom part shows the MKID substrate.

two-dimensional simulated far-field beam patterns of the extended hemispherical silicon lens fed by the double-slot antenna at 400, 440 and 480-GHz, and its cross section are displayed in Fig. 3.27. The circular symmetry beam patterns and low sidelobe and cross-polarization levels ($-$ 15 dB) were obtained with 20% bandwidth of 400 $-$ 480 GHz.

3.5 Lens Array Fabrication

The silicon lens arrays for 220 GHz and 440 GHz have 9 and 102 pixels, respectively. A small diameter lens array has been fabricated with techniques such as photolithography or laser machining (Yates et al., 2009; Llombart et al., 2010, 2011). As shown in Fig. 3.28, the individual silicon lens on the seat needs special care with epoxy for bonding the lens. To keep alignment between individual lenses and the seat, it is necessary to maintain high accuracy of the individual lens and the seat. So when the pixel number increases or observing frequencies are higher, the integrated lens array has advantages.

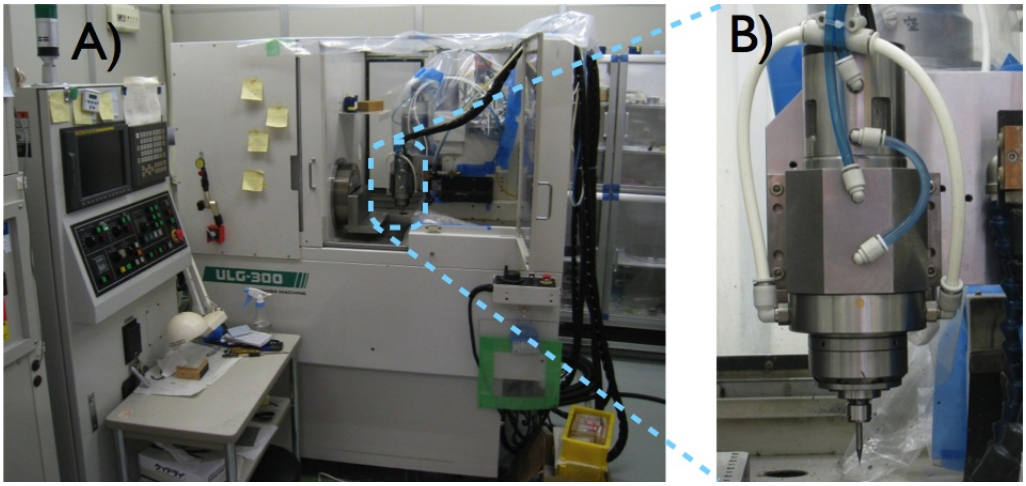

Figure 3.30: (**A**) Photograph of the Toshiba ULG-300C, an ultra-precision machine, for machining the silicon lens array. (**B**) The high-speed spindle (ABC-20M) on the Toshiba ULG-300C.

Ultra-precision cutting by using ball-end mills was tried as another efficient technique to process high-purity polycrystalline silicon in the shape of the lens (Mitsui et al., 2014). The fundamental fabrication method for each frequency band is basically the same, so only the fabrication method for the 220-GHz band lens array is described here. Geometry of extended hemispherical silicon lens array coupled to the MKID is shown in Fig. 3.29. The lens diameter and the lens spacing were 4.09 mm and 0.3 mm, respectively. The total extension thickness of 0.73 mm was divided into support plate of 0.35 mm thickness and the silicon substrate of 0.38 mm thickness.

To achieve 0.3 mm in lens spacing and obtain a surface accuracy on the order of μm, a small diameter end mill was needed. In addition, it required a rotating speed of more than several tens of thousands rpm to keep the cutting velocity of the end mill. Therefore, a combination of the ultra-precise processing machine, Toshiba ULG-300, and the high-speed spindle, Toshiba ABC-20M, has been used for this process. Figure 3.30 shows a photograph of the Toshiba ULG-300 and the Toshiba ABC-20M. The end mills are made of TiAlN coated ceramic with a radius of 0.5 mm and 0.15 mm. The machining processes of lens array are as follows:

1. Cut grooves of 4.39 mm spacing with a depth around 100 μm on high-purity polycrystalline silicon block, whose dimensions were 18 mm in length, 13.5 mm in width and 2.6 mm in thickness. The spacing of 4.39 mm corresponds to the antenna spac-

Table 3.1: Processing conditions of the 220-GHz and 440-GHz bands silicon lens array (Mitsui et al., 2014).

	220-GHz band Lens Array	440-GHz band Lens Array
Rotating Speed [rpm]	40000	40000
Rotation Unbalance [nm]	Below 10	Below 10
Cutting Feed Rate [mm/min]	$100 - 120$	100
Cutting Depth [μm]	$20 - 100$	$20 - 50$

Table 3.2: The fabrication time (only machine running time) and the number of used end-mills of lens array for each frequency bands (Mitsui et al., 2014).

	Fabrication Time (per pixel) [min]	Fabrication Time (total) [hours]	No. of Used End-mills
220-GHz band Array	53.3	8	3
440-GHz band Array	20.6	35	5

ing.

2. Shape it into a cylindrical form without changing the depth.

3. By repeating these processes and changing the radius of the cylindrical form in small steps, multiple-stage cylindrical forms are created.

4. Finally, process it into a hemispheric shape from the bottom.

Table 3.1 shows the processing conditions of the silicon lens array. Figure 3.31 shows the fabrication process of the silicon lens array. Wax was used to fix the lens array on the machining board. However, in this case, there is a possibility to break the lens array when removing the lens array from the machining board, because the extension thickness is very thin. This was fixed by stacking down several tens of wires, whose diameters are 0.2 mm, between the lens array and the machining board. This process reduces the contact area and the lens were taken out without problems.

According to Leech et al. (2012), a smooth-walled 37 pixel horn array for 230 GHz was constructed using a standard 5 axis CNC milling machine, taking around two days to manufacture. In our study, it took about 45 hours to process the 102 pixel lens array for the 440-GHz band, including the time to exchange the worn-out end mill. It took about

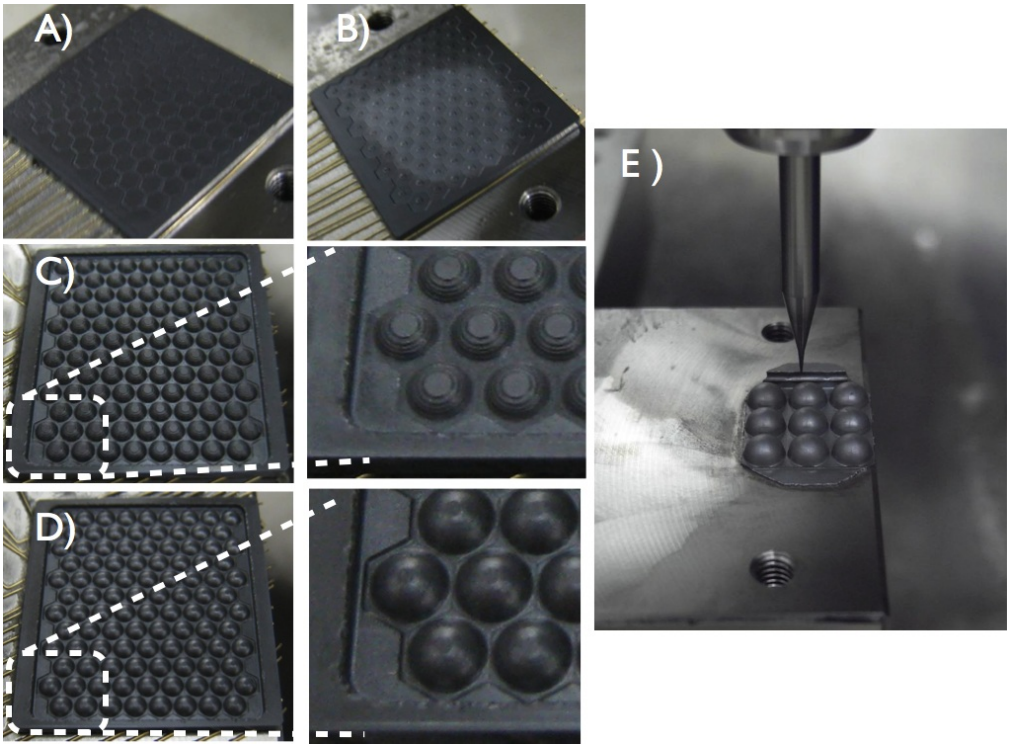

Figure 3.31: The fabrication process of the silicon lens array. (**A**) The high-purity polycrystalline silicon block, whose dimensions were 24 mm in length, 26 mm in width and 1.07 mm in thickness, on the several tens of wires. (**B**) Fabrication of the first stage of the cylindrical geometry. The depth was approximately 50 μm. (**C**) By repeating process of (B) and changing the radius of the cylindrical form in small steps, multiple-stage cylindrical forms are fabricated. (**D**) The 102 pixel lens array after finish processing. (**E**) Completed 9 pixel silicon lens array on the machining board with the TiAlN coated end-mill of 0.15 mm in radius.

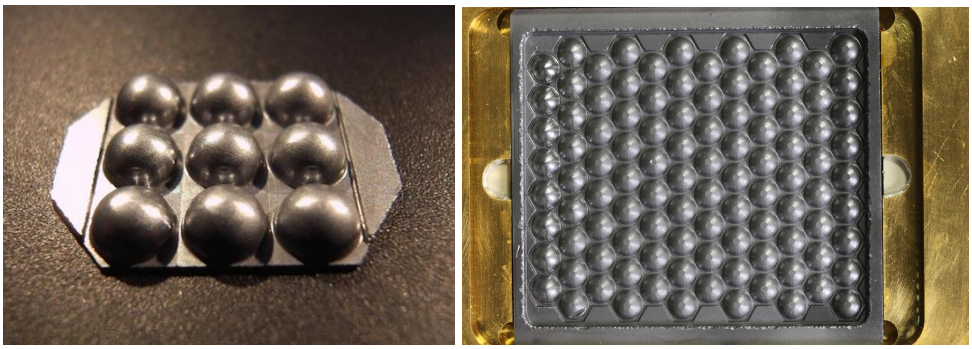

Figure 3.32: (*Left*) Completed 9 pixel silicon lens array in 220-GHz band. (*Right*) Completed 102 pixel silicon lens array in 440-GHz band.

2 hours to change an end mill. On fabrication of the 102 pixel lens array, two ball-end mills with the radius of 0.15 mm and three the radius of 0.1 mm were used. Figure 3.32

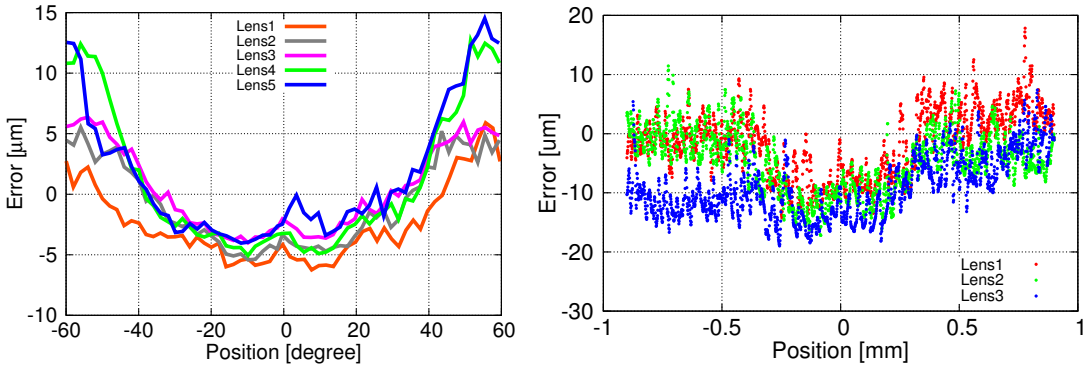

Figure 3.33: (*Left*) Measured shape errors of the lens array for the 220-GHz band. The vertical axis shows the shape error from the designed value and the horizontal axis shows the angle from the center of the lens. (*Right*) Measured shape errors of the lens array for the 440-GHz band. The vertical axis shows the shape error from the designed value and the horizontal axis shows the distance from the center of the lens.

Table 3.3: Summary of measured extension thickness and surface roughness.

	Support Plate (Design) [μm]	Support Plate (Measured) [μm]	Surface roughness (r.m.s.) [μm]
220 GHz-band 9 pixels	350	370	0.7
440 GHz-band 102 pixels	100	280	2.5

shows the completed 9 and 102 pixel silicon lens array for 220- and 440-GHz band. The configurations of 9 and 102 pixel array were grid and hexagonal shape, respectively.

3.6 Evaluations of Lens Array

Shape Measurement

A three-dimensional coordinate measuring machine, Mitutoyo LEGEX 910, was used to measure the shape of the lenses. This machine comes into contact with the measured object with a ruby ball, so small scratches on the lens surface are unavoidable. However, the depth of scratches was measured to be less than 2 μm. The left panel of Fig. 3.33 shows the results of the shape measurement of five lenses of the lens array for the 220-GHz band. The shape error is typically less than 10 μm peak-to-valley or 3 μm in rms. The results of the shape measurement of three lenses of the lens array for the 440-GHz band were also shown in the right panel of Fig. 3.33. The shape error is typically less

than 20 μm peak-to-valley or 6 μm in rms. These errors were caused by pressure exerted during fabrication.

Surface Roughness and Extension Thickness

The surface roughness of the top of the lens and the thickness of the support plate were measured by using the non-contact three-dimensional measuring machine: Mitaka Kohki NH- 3SP. The measurement results of surface roughness and support plate of lens array for each frequency band were summarized in Table 3.3. The average surface roughness of the top of the lens in 220- and 440-GHz band were around 0.7 μm and 2.5 μm in rms, respectively. These values are small enough for use in the millimeter-and submillimeter-wave range. The thickness of support plate of the 220-GHz band lens array was 0.37 mm, which was 0.02 mm thicker than the designed value of 0.35 mm. The extension thickness affects beam pattern qualities such as sidelobe level and symmetry of the main beam. However, simulation results showed that these error values are within acceptable limits and do not affect the beam patterns much. On the other hand, the support plate thickness of the 440-GHz band lens array was 0.28 mm, which was 0.18 mm thicker than the designed value of 0.1 mm. It seems to affect the beam pattern since the measurement result was three times thicker than the designed value. Furthermore, the processing results of two lenses showed that the process limitation of the extension thickness would be around 300 μm.

4

Beam Pattern Measurements of Millimeter/Submillimeter-Wave KID Camera

This chapter includes material accepted for publication in IEEE Transactions on Terahertz Science and Technology, as "Beam Pattern Measurements of Millimeter-Wave Kinetic Inductance Detector Camera With Direct Machined Silicon Lens Array"
by T. Nitta, M. Naruse, Y. Sekimoto, K. Mitsui, N. Okada, K. Karatsu, M. Sekine, H. Matsuo, T. Noguchi, Y. Uzawa, M. Seta, and N. Nakai

4.1 Introduction

The optical system of the MKID cameras is based on double-slot antennas and the extended hemispherical silicon lens array as described in the previous chapter. The aim of this chapter is to measure the beam patterns of 220- and 440-GHz band cameras. A setup of the beam pattern measurement and the evaluation results of the MKID array at 0.3 K are also discussed.

4.2 Measurement System

4.2.1 0.3 K Sorption Cooler

A cryostat must cool down the MKIDs to temperatures below Tc, in order for the material to become superconductor. A ^{3}He sorption cooler mounted on a liquid helium (^{4}He) bath was used for beam pattern measurements of MKID cameras. The cooling operation of sorption cooler is as follows:

1. Pre-cooling
   Pre-cooling of 4 K and 77 K tanks with liquid-nitrogen. The temperatures at 4 K and 0.3 K stages are monitored by using silicon and germanium thermometer, respectively.

2. Liquid-helium supply
   After the pre-cooling with liquid-nitrogen, the 4 K and 0.3 K stages are cooled down to 4.2 K by supplying liquid-helium. Turn on a heat switch during supplying liquid-helium.

3. ^{3}He gas control
   The 4 K and 0.3 K stages are cooled by evaporative cooling with a vacuum pump which consists of a rotary and mechanical booster pump. When the temperature of 0.3 K stage reaches 2 K, current of several mA is applied to the heater at the sorption cooler. An activated charcoal, which is located inside the sorption cooler, releases ^{3}He-gas when it is heated to about 30 K. The heater current is turned off when temperature at the sorption cooler reached to 30 K.

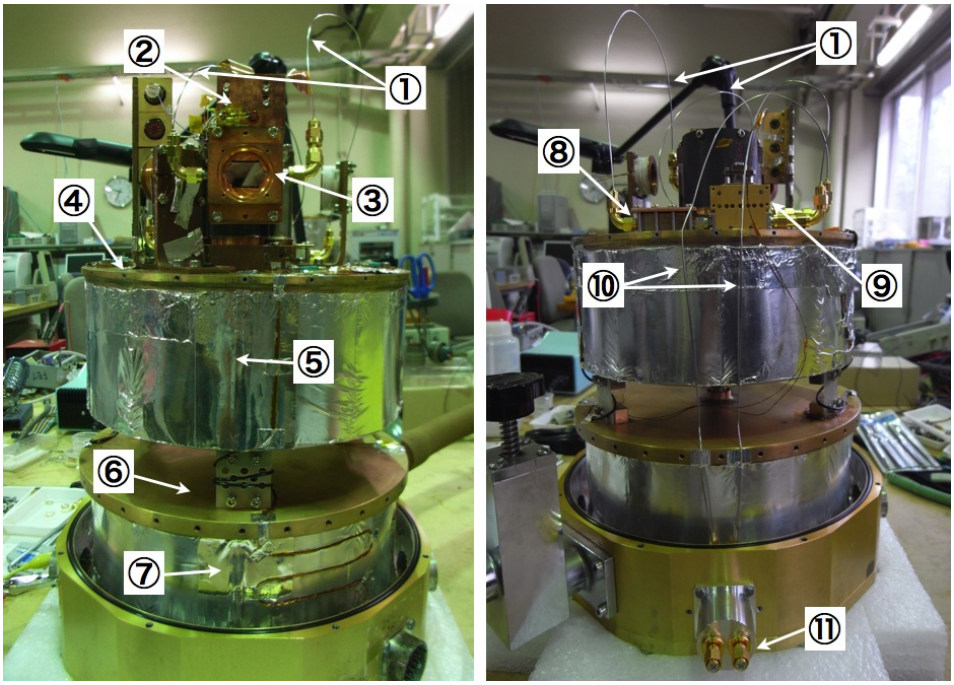

Figure 4.1: A photograph of the inside of the 0.3 K sorption cooler. 1: 0.86 mm diameter CuNi SMA cables (0.3 K — 4 K). 2: 0.3 K cold stage. 3: sample box of MKID camera. 4: 4 K cold stage. 5: Liquid-helium tank. 6: 77 K cold stage. 7: Liquid-nitrogen tank. 8: Cold isolator. 9: Cold low-noise amplifier. 10: 0.86 mm diameter CuNi SMA cables (4 K — 300 K). 11: Input and output SMA connectors.

4. Evaporative cooling

   When the 0.3 K stage temperature is cooled below 2 K, a heat switch of the 0.3 K stage and the sorption cooler are turn off and on, respectively. In the result, the sorption pump starts to absorb the ^{3}He and decreases the vapor pressure. The 0.3 K stage is cooled by evaporative cooling and the stage temperature reaches 0.3 K. It takes about two hours to operate the He-gas control.

Temperature of the cold stage was kept at around 0.3 K and the holding time is about 8 hours. Figure 4.1 shows a photograph of the inside of the 0.3 K sorption cooler. We use a copper-based sample box with two SMA connectors for readout of the microwave signals. The MKID sample box is connected with 0.86 mm diameter CuNi coaxial cables to a high electron mobility transistor (HEMT) amplifier on the 4 K stage. The CuNi has low thermal conductivity. Therefore, the choice for thin CuNi coaxial cable is to reduce the thermal load on the MKID sample box (Barends, 2009). The MKID camera was mounted on the 0.3 K cold stage, as shown in Fig. 4.1.

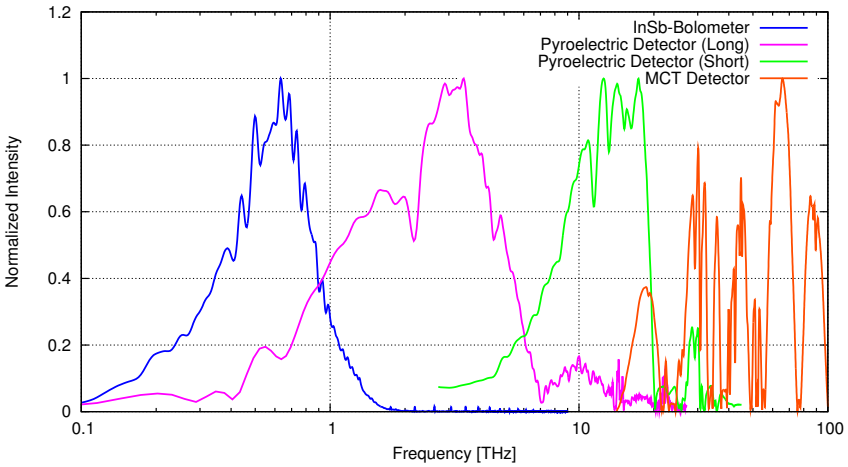

Figure 4.2: Frequency response of various types of detectors for FTS transmittance measurements.

Table 4.1: Setup of the detectors for a wide-bands transmittance measurements.

Detector Type	Beam Splitter	Operation Temperature [K]	Resolution [GHz]	Frequency Range [THz]
InSb Bolometer	Wire-grid	4	15	0.15 - 1.8
Pyroelectric Detector (Long)	Wire-grid	300	120	1.5 - 6
Pyroelectric Detector (Short)	Mylar	300	240	5 - 20
MCT Detector	Mylar	77	240	15 - 100

A merit of cryostat with a cryogen and sorption cooler is less affected by external magnetic field because the cryostat without the mechanical cooler such as a Gifford-McMahon cooler. However, a cryostat has no magnetic shield near the 0.3 K stage. So the beam pattern measurements were performed in a magnetic shield room of permalloy to remove the effect of the magnetic field from the measurement instruments and terrestrial magnetism.

A power of 0.52 W from a blackbody spectrum at 300 K is incident on the vacuum window of 38 mm diameter. This power is cut successively by IR blocking filters, a single ZITEX G-115 filter at ambient temperature, a double black polyethylene filters at 77 K, a single black polyethylene filter and a 1-THz low-pass filter at 4 K.

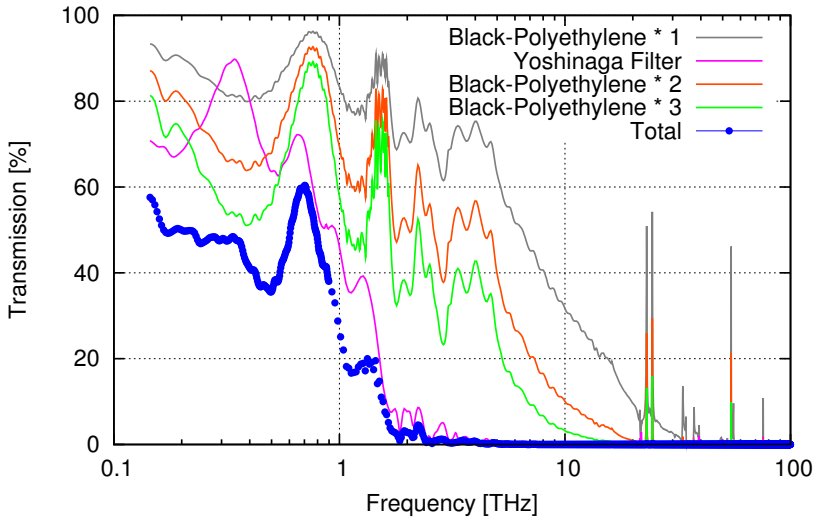

Figure 4.3: Total transmittance of IR blocking filters chain for a 0.3 K optical measurement system. Blue line corresponds to the total filter transmittance.

Table 4.2: Summary of the detailed information about the filter chain.

	Measured Value
Cutoff Frequency of Filter Stack	1 THz
Leakage at IR Region	$< 10^{-12}$
Transmittance of Total Filters at 220 GHz	48%
Transmittance of Total Filters at 440 GHz	38%

4.3 IR Blocking Filter

4.3.1 Detector Response

Infrared (IR) blocking filters are an important component for millimeter- and submillimeter wave receivers because the peak wavelength of the 300 K blackbody spectrum is around 10 μm (= frequency of 30 THz). The low-pass filters, which have high transmittance at millimeter-wave range and high cutoff at mid- to near-IR region, were needed to reduce a thermal load from outside of the vacuum window. There are various types of IR blocking filters such as absorption, reflection, interference and scattering types. A Fourier transform spectrometer and four types of detectors were used to measure the broadband transmittance of various low-pass filters at millimeter-wave to near-IR region. Figure 4.2 shows the frequency response of various types of detectors for FTS transmittance measurements. These four detectors can be measured in the frequency range of 0.2 — 100

THz (millimeter-wave to IR region). Setup of the FTS and detectors for a wide-bands transmittance measurements is summarized in Table 4.1.

4.3.2 Filter Transmittance

Five low-pass filters are used to reduce the 300 K radiation through the vacuum window. They are made of ZITEX (type G-115), black polyethylene for photographic paper, and a 1-THz low-pass filter. The thickness of ZITEX, black polyethylene and 1-THz low-pass filter were 400, 125, and 600 μm, respectively. The 1-THz low-pass filter is made from polyethylene sheet containing reststrahlen crystals powder (Yamada et al., 1962). Figure 4.3 shows the total transmittance of IR blocking filter chain for a 0.3 K optical measurement system. The IR blocking filter chain was composed of a signal ZITEX filter at ambient temperate, a double black polyethylene filters at 77 K, and a single black polyethylene filter and a 1-THz low-pass filter at 4 K. A blue line in the Fig. 4.3 corresponds to the total filter transmittance. Total transmittance of these filters at 220 and 440-GHz bands were about 48% and 38%, respectively. As shown in Table 4.2, leakage at IR Region was less than 10^{-12} and its cutoff performance was enough for cooling the MKID camera to 0.3 K.

4.4 Beam Pattern Measurements at 220 GHz bands

4.4.1 9 pixel MKID Camera

The MKID cameras are composed of direct-machined silicon lens arrays and Al-based MKIDs which can detect photons at frequencies higher than 90 GHz. The MKIDs were quarter-wavelength CPW resonators coupled to a CPW feed line with a 8 μm wide gap and 12 μm central line, which connects all pixels. A shorted end of the CPW line acts as the feed to a single-polarization sensitive double-slot antenna placed in the geometrical focus of a silicon lens mounted to the back of the detector substrate.

Epitaxial Al(111) film has been grown on a Si(111) wafer by using molecular beam epitaxy (MBE) (Naruse, 2012; Naruse et al., 2012). The Al film with 150 nm thickness was patterned into quarter wavelength CPW resonators by wet etching process. The CPW geometry had a 3 μm-wide central line and 2 μm-wide gaps. The MKID substrate was glued to the sample box by using varnish. Metallic surface of the sample box on

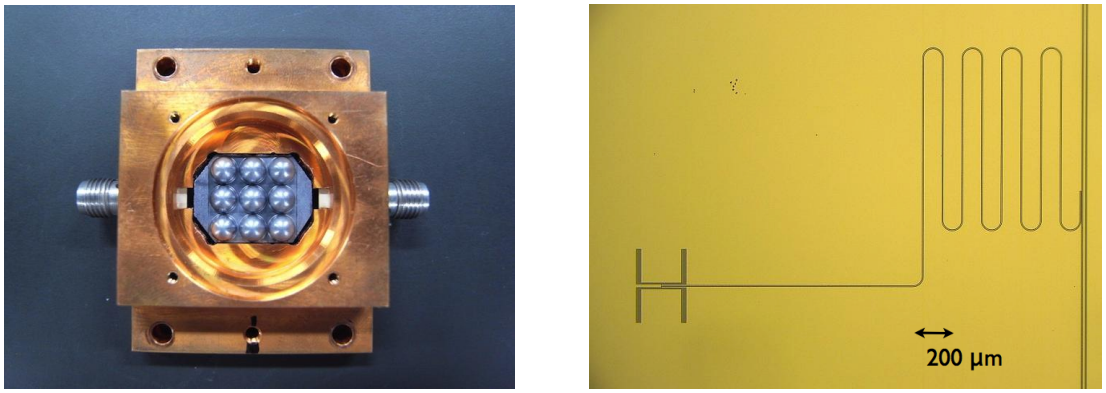

Figure 4.4: (*Left*) A photograph of the 9 pixel MKID camera for 220-GHz band. The sample box was made of oxygen-free copper and has two SMA connectors for readout of the microwave signals. (*Right*) Microscopic picture of a double-slot antenna coupled to quarter-wave CPW resonator. The light and dark parts correspond to the aluminum film and the silicon wafer, respectively.

the opposite side of the lens array was coated with a mixture of Stycast 2850FTJ and approximately 1 mm size silicon carbide grains to form an absorber to absorb stray light (Barends, 2009; Baselmans et al., 2012).

An SMA connector was connected to a microwave board which acts as transition between the feed line of the MKID array and the SMA connector. Al wires of 20 μm diameter were bonded for the electrical connection. Additional bonding wires were arranged at sides of CPW to have a well-defined ground.

Figure 4.4 shows a photograph of 9 pixel MKID camera for 220-GHz band and a double-slot antenna coupled to a quarter-wave CPW resonator. The double-slot antenna is patterned at the end of the quarter-wave resonator, which is on the opposite side of the feed line. The light and dark parts of device picture correspond to the aluminum film and the silicon wafer, respectively.

4.4.2 MKID Response at 0.3 K

Input Power Dependence

To optimize the ideal feed power to the MKID, the output power of a VNA was swept (see Fig. 4.8). The left panel of Fig. 4.5 shows the feed microwave power dependence of the MKID resonator response at 0.3 K. A low feed power leads to a noisy signal, whereas too large power shows non linear effects. In our measurement setup, the attenuation

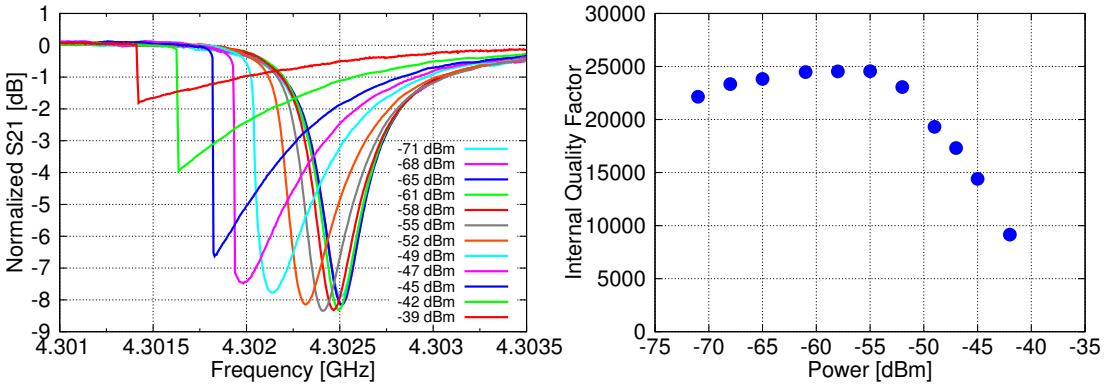

Figure 4.5: (*Left*) Feed microwave power dependence of the MKID response at 0.3 K. (*Right*) Internal quality factor versus the microwave power level in the feed line. From measured results, optimum microwave power at 0.3 K was around − 55 dBm.

Table 4.3: Various quality factors of 9 pixel MKIDs at 0.3 K

MKID No.	Q_l	Q_i	Q_c
1	29121	35860	154968
2	24332	27936	188619
3	6677	10958	17093
4	18352	22901	92396
5	41761	60955	132624
6	8734	27830	12729
7	18115	30030	45658
8	—	—	—
9	14113	29584	26987

between VNA and input SMA connector of MKID sample box given by the CuNi coaxial cables was measured to be about 16 dB at 5 GHz. So the feed power is calculated as,

$$\mathrm{P_{KID}[dBm]} = \mathrm{P_{VNA}[dBm]} - 16\mathrm{[dB]}. \tag{4.1}$$

The feed power displayed in Fig 4.5 corresponds to $\mathrm{P_{KID}[dBm]}$. The right panel of Fig. 4.5 shows the internal quality factor as a function of the feed microwave power. The optimized feed power was determined to be $\mathrm{P_{KID}}$ = − 55 dBm. In this case, the value of internal quality factor becomes the maximum.

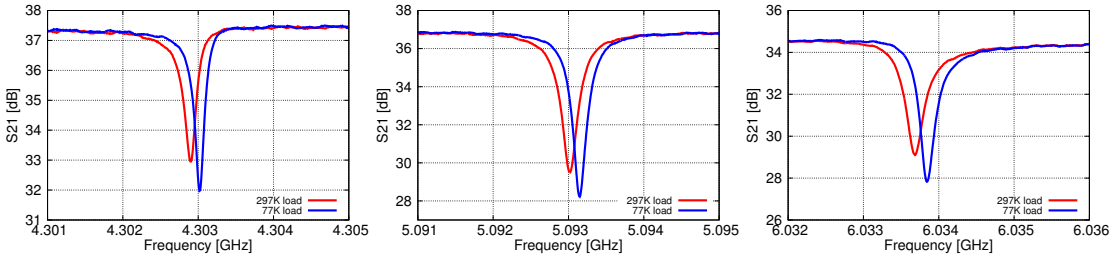

Figure 4.6: Hot and cold load responses of the 3 MKIDs at 0.3 K.

Quality Factor

For determining the quality factor and resonant frequency we measure the forward transmission S_{21} with a vector network analyzer. Resonant parameters, such as resonant frequency and each quality factor, are derived by fitting the S_{21} spectrum with a Lorentzian model. Loaded, internal, and coupling quality factors of 9 pixel MKID array were summarized in Table 4.3. Typical internal quality factors at 0.3 K of 9 pixel MKID array were around 30000.

Hot/Cold Response

To confirm overall response of the MKID array, optical responses of the MKID array were measured by using hot (300 K blackbody absorber with ECOSORB) and cold loads (77 K blackbody absorber sunk in liquid nitrogen). Figure 4.6 shows the hot and cold load responses of the three resonators at 0.3 K. Hot and cold loads were located in front of the vacuum window of the cryostat. As shown in Fig. 4.6, blackbody radiations of 77 K and 300 K were distinguished by MKIDs array. In addition, these results demonstrate that the MKIDs have large dynamic range because they were not saturated with the 77 K blackbody source, and that lead to efficient astronomical observations with easy calibration.

4.4.3 Beam Patterns

Beam patterns of the MKID array were measured with an external CW source. The left panel of Fig. 4.7 shows a photograph of the outside of the magnetic-shield room. Some instruments for beam pattern measurements are displayed. The right panel of Fig. 4.7 shows a photograph of the inside of the magnetic-shield room. A 0.3 K cryostat and millimeter-/submillimeter-wave external CW source are displayed. Figure 4.8 shows a

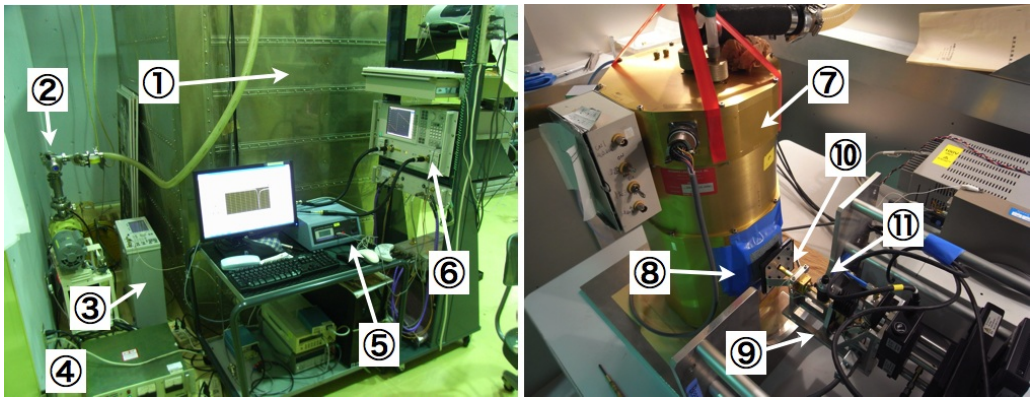

Figure 4.7: (*Left*) A photograph of the outside of the magnetic-shield room. 1: Magnetic-shield room. 2: Vacuum pump for decompression of the liquid-helium tank. 3: Signal generator. 4: Electrical power supply with noise reduction filters. 5: XYθ beam-scanner controller. 6: Vector network analyzer. (*Right*) A photograph of the inside of a magnetic-shield room. 7: 0.3 K cryostat. 8: Vacuum window. 9: XYθ beam-scanner. 10: Rectangular probe horn. 11: Power amplifier.

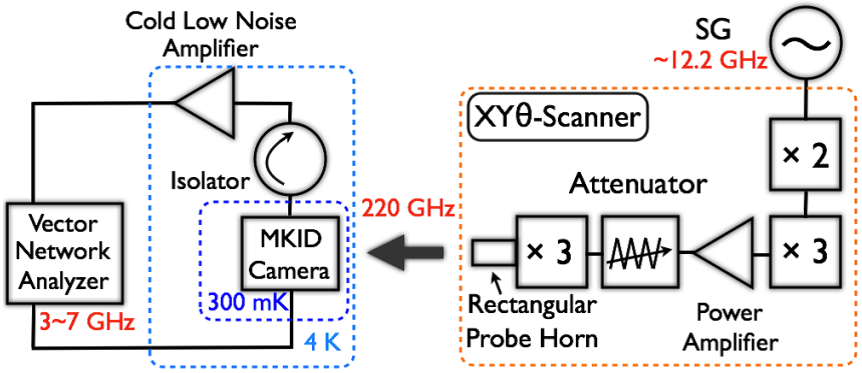

Figure 4.8: A block diagram of the beam pattern measurement system. The figure shows the measurement system for 220-GHz band. For 440-GHz band, the signal generator output about 14.7 GHz and the tripler behind the rectangular probe horn is exchanged with the quintupler. The position of the CW source is moved by an XYθ-scanner.

block diagram of the beam pattern measurement system. External CW sources for the 220- and 440-GHz bands were composed of a signal generator (100 kHz — 20 GHz), frequency multipliers, a power amplifier, an attenuator, and a rectangular open-ended waveguide (probe horn). The probe horn was fabricated with electro-forming to make thinner edge, which reduces standing wave. The electro-forming probe horn has good beam pattern and low standing wave (Naruse et al., 2009a). The probe horn was surrounded by electromagnetic absorber tiles (TK-RAM, Thomas-Keating Co.), as shown in

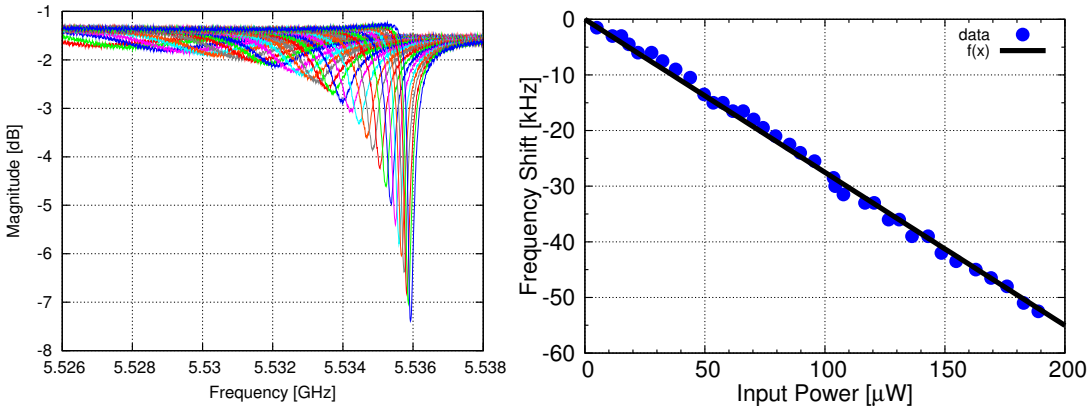

Figure 4.9: (*Left*) The S_{21} response to various external 220-GHz radiation powers. (*Right*) The resonant frequency shifts versus external 220-GHz radiation power. Blue points showed the measured data and black line was a linear fit.

Fig 4.7.

Power Response at 220 GHz

The millimeter- and submillimeter-wave external radiation sources emit 200 — 240 GHz and 400 — 480 GHz, respectively. The external radiation power to the MKID was adjusted by the gate voltage of a power amplifier, which was shown in the right panel of Fig. 4.7. The radiation power at 220-GHz was tunable from 0.3 μW to about 600 μW. Distance between the vacuum window and the probe horn was approximately 23 mm, and that between the device substrate and the probe horn was approximately 78 mm, respectively.

The resonant frequencies of MKIDs were measured from the S_{21} spectrum taken by a vector network analyzer. The left panel of Fig. 4.9 shows the S_{21} response of various external 220-GHz radiation power. Incident photons break cooper pairs and create quasiparticles in the MKID, and increasing the number of the quasiparticles induces changing the surface impedance of the MKID. In consequence, the resonant frequency slightly shifts. The right panel of Fig. 4.9 shows the resonant frequency shifts versus external 220-GHz radiation power. The data were derived from the left panel of Fig. 4.9. The shift of resonance frequency and the change of the amplitude of resonances correspond to detected power in an MKID.

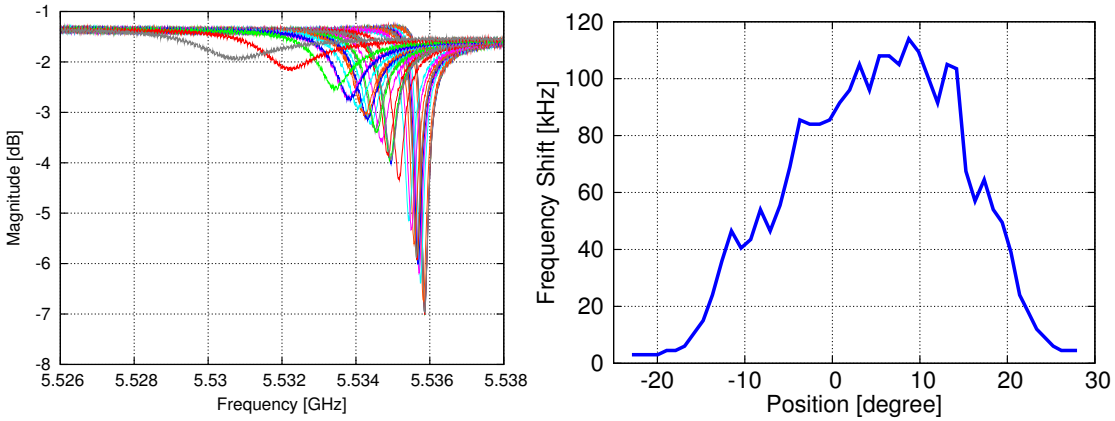

Figure 4.10: (*Left*) The S_{21} response to various position of the external radiated source. (*Right*) The resonant frequency shifts as a function of the external source position, which is controlled by a XYθ-scanner in front of the vacuum window of the cryostat.

Scan Data

In the same way as power response measurement, the detected power was recorded as a function of the position of the external source which was controlled by a $XY\theta$ scanner in front of the vacuum window of the cryostat. The XY stage of this scanner was used to measure the two-dimensional beam patterns. The XY scan area and the measurement interval were 72 mm $\times$ 84 mm and 1.5 mm, respectively. The θ stage of this scanner can be rotated from $-$ 90 degrees to 90 degrees and was used to measure the cross-polarization pattern and the alignment of the polarization. These stages were precisely controlled by stepping motors. The all instruments for the measurement of beam pattern were controlled via GPIB interface by LabView software.

The left and right panels of Fig. 4.10 show the S_{21} response of various positions of the external radiated source and the resonant frequency shifted as a function of the external source position, respectively. The beam pattern was calculated from the comparison of the data of resonance frequency shift as functions of the external radiation power and the position of $XY\theta$ scanner.

Co-Polarization Patterns

The measured results of 2D far-field co-polarization beam patterns of the extended hemispherical silicon lens array fed by the double-slot antennas at 220 GHz are shown in Fig.

4.11. A typical two-dimensional scan took approximately 3 hours. The dynamic range of this measurement system was about 20 dB, which is limited by the Al MKID's sensitivity at the measurement temperature of 0.3 K.

The measured results showed circular symmetrical patterns. While some pixels, MKID 2, 5, 9, showed asymmetrical patterns. The larger beam ellipticity was caused by the misalignment between the silicon lens and the double-slot antenna, and by reflection on the silicon lens array, because anti-reflection coating was not applied on the lens. Figure 4.12 shows the cross section of far-field beam patterns at 220 GHz. The dot and solid lines showed the simulated and the measured patterns, respectively. Figure 4.13 shows the 2D far-field beam patterns of the extended hemispherical silicon lens array fed by the double-slot antennas at 200 GHz, and its cross section patterns. The comparison of the measured beam patterns with the calculations showed good agreement. This proved that the silicon lens array, processed with the ultra-precision cutting, is capable of performing as the optical system of the millimeter and submillimeter-wave cameras. In chapter 6, anti-reflection coatings for silicon lens array were developed to reduce the reflection loss of about 30% between the air and the silicon.

Cross-Polarization Patterns

Figure 4.14 shows the measurement results of 2D far-field cross-polarization beam patterns of the extended hemispherical silicon lens array fed by the double-slot antennas at 220 GHz. The left and right panels of Fig. 4.14 correspond to MKID 2 and 3, respectively. The cross-polarization levels were derived from the integration values from -10 degrees to 10 degrees of each axis which correspond to the main lobe (-3 dB region) of co-polarization patterns. The integrated cross-polarization levels of both results were around -10 dB less than peak of the co-polarization patterns. The measured levels were higher than simulated levels of around -20 dB. It is considered to be caused by characteristic of IR blocking filters such as shape distortion and standing wave between filters.

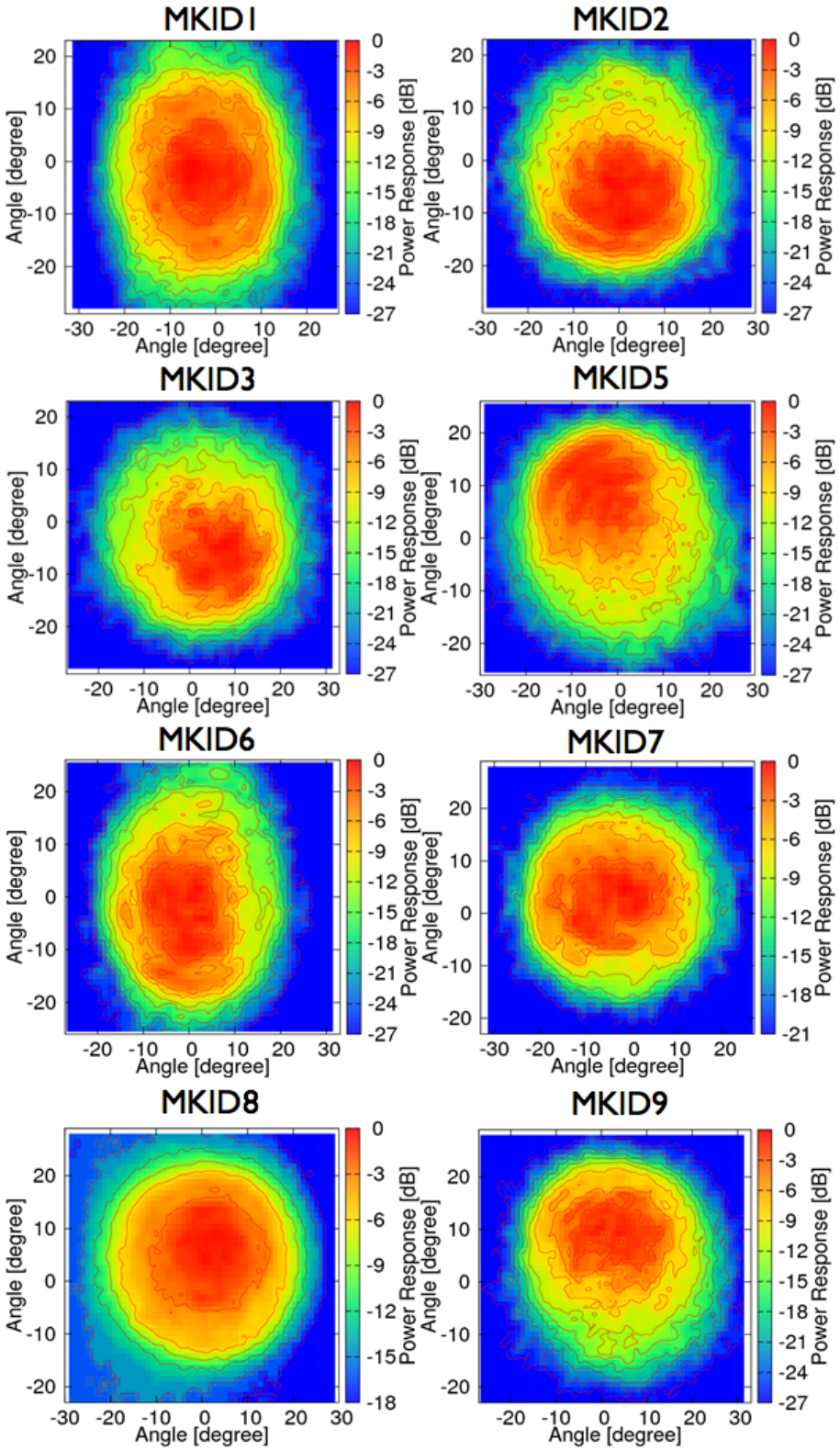

Figure 4.11: Measurement results of 2D far-field co-polarization beam patterns of the extended hemispherical silicon lens array fed by the double-slot antennas at 220 GHz. The contours were every 3 dB steps.

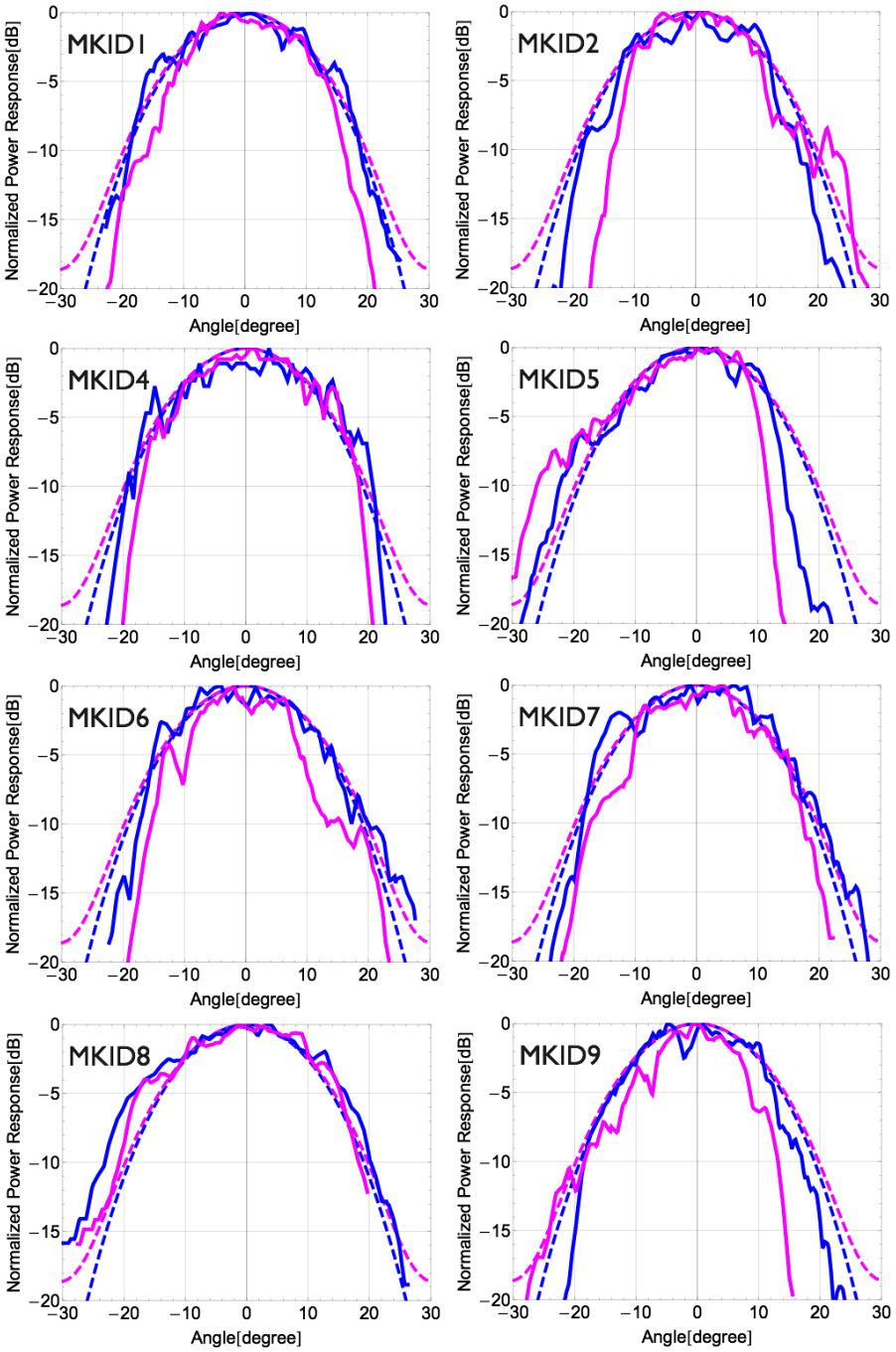

Figure 4.12: Measurement results of 1D far-field co-polarization beam patterns at 220 GHz obtained from eight Al MKIDs. The dot and solid lines showed the simulated and the measured patterns, respectively. Blue lines and pink lines correspond to the E-plane and the H-plane, respectively.

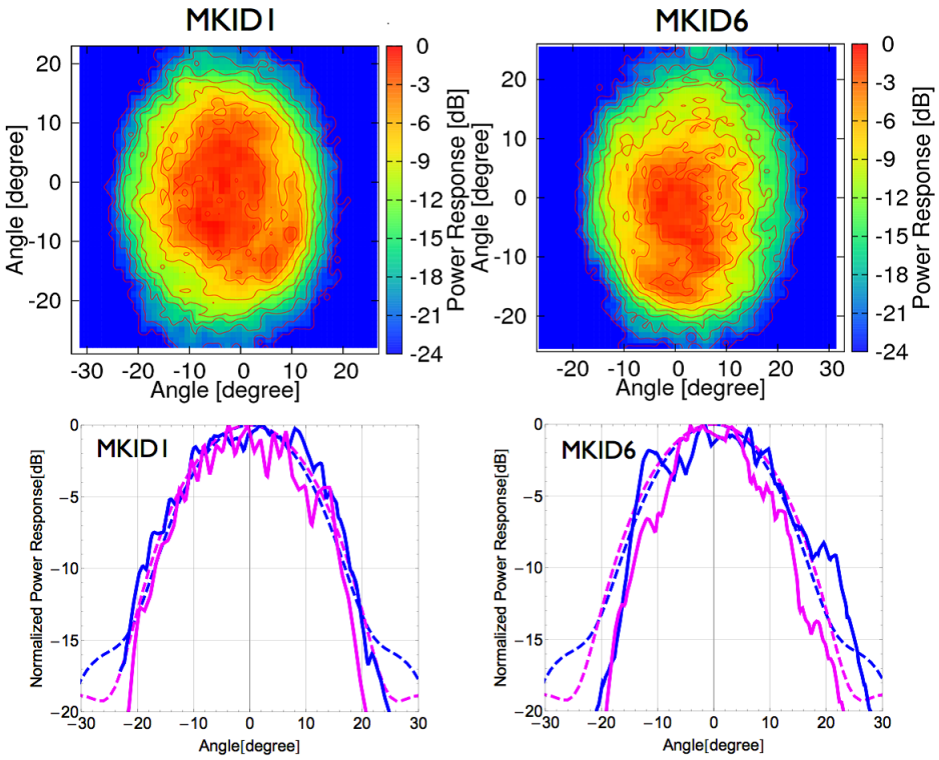

Figure 4.13: Measurement results of 2D (top) and 1D (bottom) far-field co-polarization beam patterns of the extended hemispherical silicon lens array fed by the double-slot antennas at 200 GHz. The contours were every 3 dB steps. The dot and solid lines showed the simulated and the measured patterns, respectively. Blue lines and pink lines correspond to the E-plane and the H-plane, respectively.

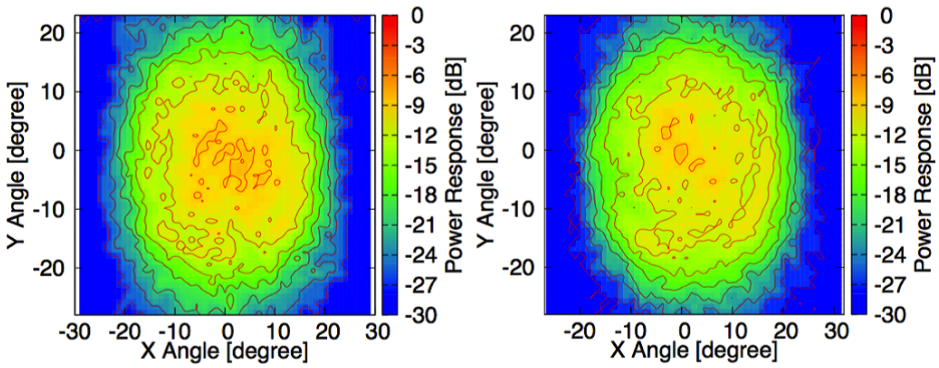

Figure 4.14: Measurement results of 2D far-field cross-polarization beam patterns of the extended hemispherical silicon lens array fed by the double-slot antennas at 220 GHz. The contours were every 3 dB steps.

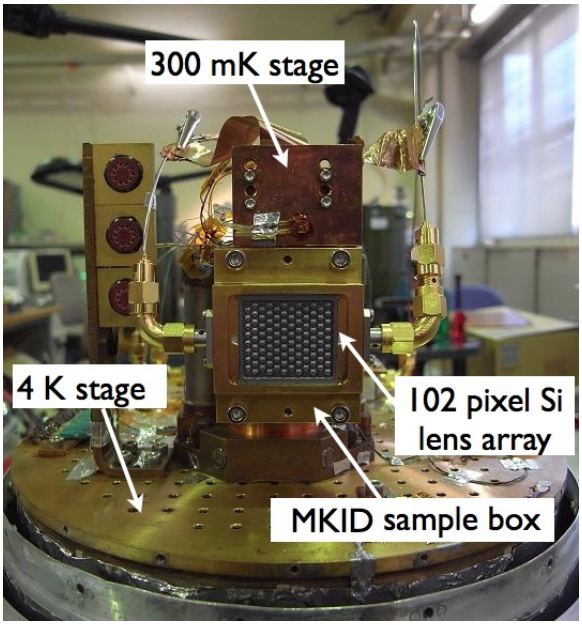

Figure 4.15: The 102 pixel sub-millimeter wave MKID camera for 440-GHz band mounted on the 0.3 K cold stage. The dimension of the silicon lens array was 24 mm $\times$ 26 mm.

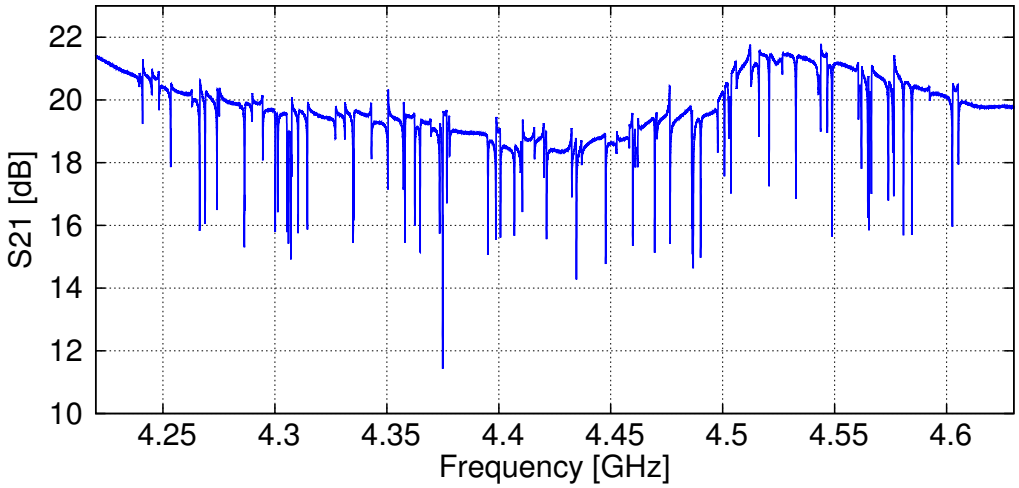

Figure 4.16: The S_{21} spectrum of 102 pixels MKID array at 0.3 K. The number of measured pixels were 90 (yield of $\sim$ 90%), and resonance frequencies falls into a 400 MHz band centered at 4.4 GHz. The typical internal quality factor at 0.3 K of this array was around 30000.

4.5 Beam Pattern Measurements at 440 GHz bands

In a similar way of 220-GHz band beam pattern measurements, 440-GHz band beam patterns of 102 pixel array were measured. Figure 4.15 shows the 102 pixel sub-millimeter

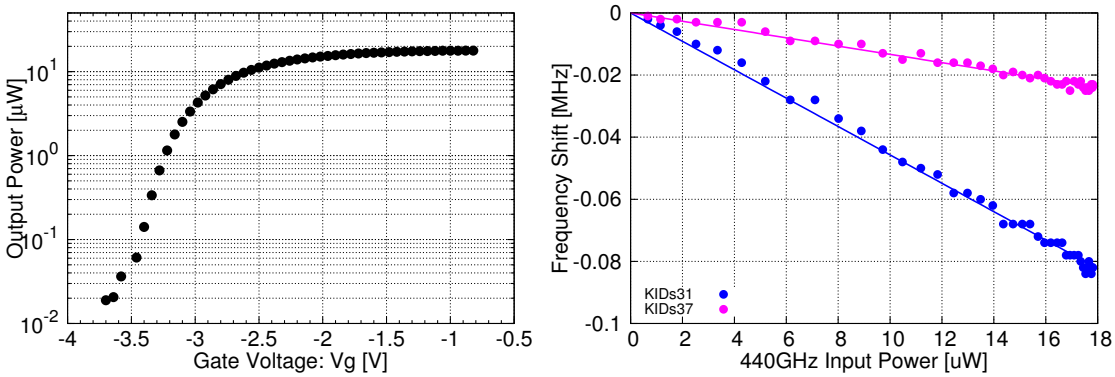

Figure 4.17: (*Left*) Output power control of external 440-GHz radiation source. This figure shows the 440-GHz output power as a function of gate voltage of power amplifier. (*Right*) The resonant frequency shifts versus external 440-GHz radiation power. Color points showed the measured data and solid lines were linear fits.

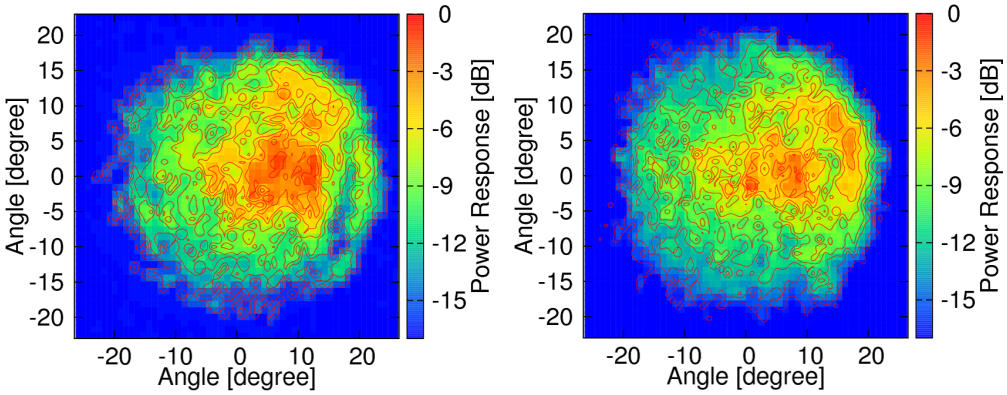

Figure 4.18: Measurement results of 2D far-field co-polarization beam patterns of the extended hemispherical silicon lens array fed by the double-slot antennas at 440 GHz. The contours were every 2 dB steps.

wave MKID camera for 440-GHz band mounted on the 0.3 K cold stage. Gold-plated copper sample box with two SMA connectors for readout of the microwave signals was used. Figure 4.16 shows the S_{21} spectrum of 102 pixels MKID array at 0.3 K. The number of measured pixels were 90 and high yield rate of around 90% was achieved. The resonance frequencies fell into a 400 MHz band centered at 4.4 GHz. A typical internal quality factor at 0.3 K of this array was around 30000.

The left panel of Fig. 4.17 shows output radiation power at 440 GHz as a function of gate voltage of a power amplifier which is a critical component of the external radiation source. The radiation power at 440 GHz was tunable from 20 nW to about 20 μW. The

right panel of Fig. 4.17 shows the resonant frequency shifts of two MKIDs as a function of the external 440-GHz radiation power. Points and solid lines correspond to the measured data and linear fits, respectively.

Figure 4.18 shows the measurement results of 2D far-field co-polarization beam patterns of the extended hemispherical silicon lens array fed by the double-slot antennas at 440 GHz. The results of two detectors were displayed. The measured results showed circular symmetrical patterns. However, the measured main beams which correspond to the center region of two-dimensional maps did not agree with the simulated patterns. This difference was likely to be caused by fabrication error of the extension thickness as discussed in Chapter 3. The extended hemispherical silicon lens for high-frequency bands or with a small diameter becomes structurally friable as the extension thickness decreases. In Chapter 5, we discussed a small-diameter silicon lens that uses only the upper surface of the lens to solve this issue.

5

Close-Packed Silicon Lens Antennas for High-Frequency-Band Camera

This chapter includes material accepted for publication in Journal of Low Temperature Physics, as "Close-Packed Silicon Lens Antennas for Millimeter-Wave MKID Camera" by T. Nitta, K. Karatsu, Y. Sekimoto, M. Naruse, M. Sekine, S. Sekiguchi, H. Matsuo, T. Noguchi, K. Mitsui, N. Okada, M. Seta, and N. Nakai

5.1 Introduction

A large-diameter ($>3\lambda$, where λ is the target wavelength) dielectric lens has been widely used in the millimeter- and submillimeter-wave range (Filipovic et al., 1993; Pearson et al., 2003). In the previous chapter, we demonstrated the 3λ-diameter lens for 220-GHz and 440-GHz bands. However, to realize a diffraction-limited wide field-of-view camera with 10000 pixels, a more highly integrated small-size ($<3\lambda$ diameter) lens array (Kasilingam & Rutledge, 1986; Godi et al., 2005) and fast focal plane are required.

Misalignment between lens and planar antenna causes beam distortion, such as elliptical beam patterns. The required beam quality depends on the application: CMB observations require a high-quality beam pattern, whereas ground-based high-z galaxy surveys require a reasonable beam with numerous pixels. We investigated the main beam symmetry, side-lobe level, cross-polarization level, and bandwidth of close-packed arrays with diameters of 1.2λ, 2λ, and 3λ, considering the effects of the surrounding lenses and the effect of misalignment between the silicon lens and double-slot antenna.

5.2 Height Dependence of Small-Diameter Silicon Lens

Effects of a gap between lenses on beam pattern were studied. Figure 5.1(A) shows the shape and design parameters of an extended hemispherical silicon lens. Here the extension thickness L is defined as $L = d - R$, where d is the distance between the antenna and the lens top, and R is the lens radius. In Chapter 3, the beam patterns of the extended hemispherical silicon lens fed by the double-slot antenna were calculated to optimize the extension thickness by using $HFSS$, as shown in Fig. 5.1(B). The length, width, and slot separation of the double-slot antenna for the 220-GHz band were 382, 25, and 218 μm, respectively. The antenna bandwidth (-10 dB return loss) was approximately 20%. The extension thickness was optimized with respect to the parameters of beam pattern quality, such as side-lobe level and main beam symmetry. It was determined to be $L/R = 0.34$ as shown in chapter 3.

The extended hemispherical silicon lens with a small diameter or high frequency becomes structurally friable as the extension thickness decreases. Thus, we adopted the small-diameter silicon lens that uses only the upper surface of the lens (Alonso-DelPino

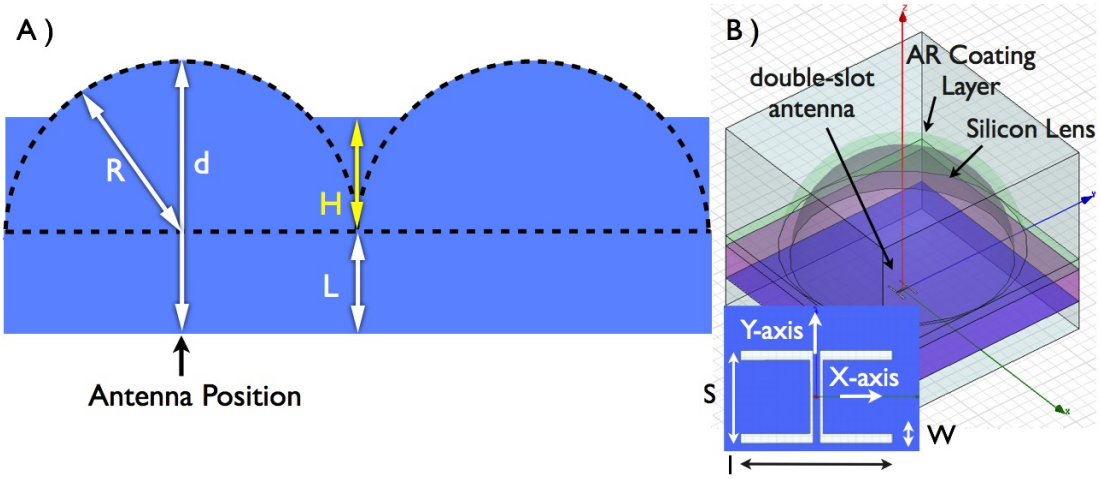

Figure 5.1: (**A**) Shape and design parameters of an extended hemispherical lens. L, R, and d correspond to the extension thickness, lens radius, and the distance between the antenna and the lens top, respectively. H is the length from the hemispherical lens center to top of the planar part. (**B**) Simulation model of an extended hemispherical silicon lens antenna. The double-slot antenna is located at the focus of the AR-coated silicon lens. s, l, and w correspond to the slot separation, antenna length, and antenna width, respectively.

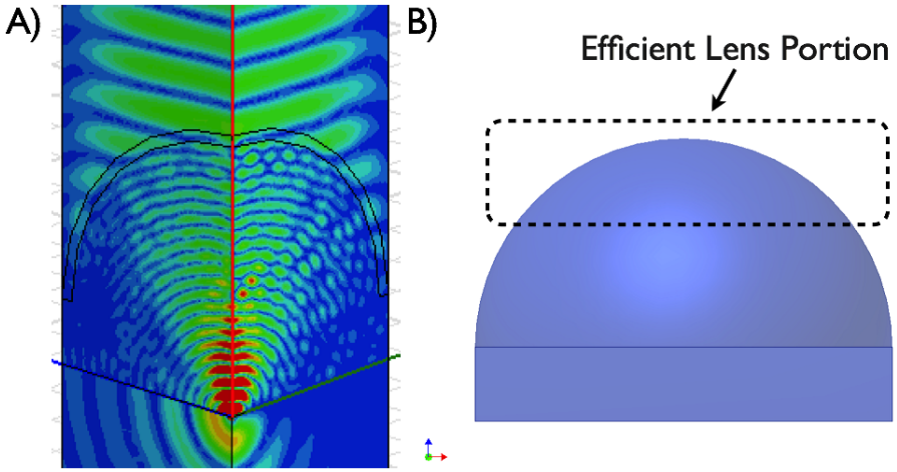

Figure 5.2: (**A**) Electric field distribution at 220 GHz of an extended hemispherical silicon lens. (**B**) Cross section of an extended hemispherical silicon lens. In general, the upper portion of the silicon lens is used effectively.

et al., 2013), as shown in Fig. 5.1(A). Figure 5.2(A) shows the electric field distribution inside an extended hemispherical silicon lens. As shown in Fig. 5.2(A), the electric field inside the lens is concentrated on its upper surface. In fact, rays reaching the lens-air interface at a low angle are not focused in useful directions (Baryshev et al., 2011). Therefore, the upper portion of the silicon lens is used effectively as shown in Fig. 5.2(B).

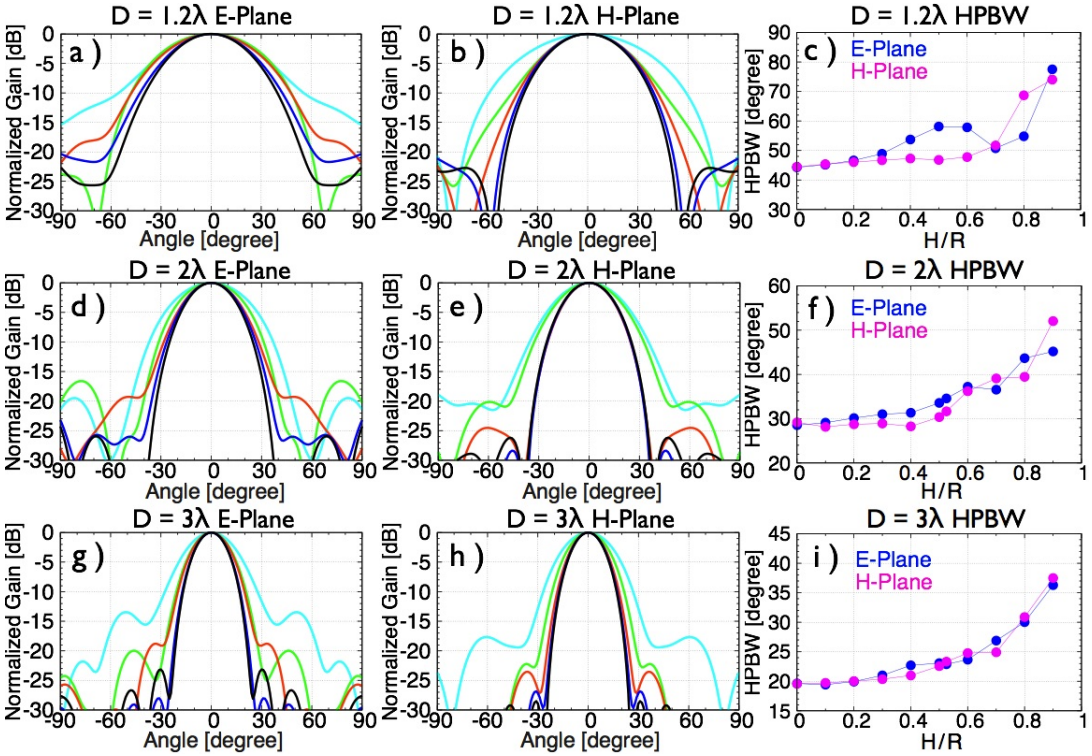

Figure 5.3: The gap height H dependence of normalized (**a**) E-plane and (**b**) H-plane beams at 220 GHz. Black, blue, orange, green, and light blue lines correspond to $H/R = 0$, 0.2, 0.4, 0.6, and 0.8, respectively. (**c**) Half-power beam width of E- and H-planes of 1.2λ-diameter lens. (**d**),(**e**),(**f**) and (**g**),(**h**),(**i**) are the same results with 2λ- and 3λ-diameter lens, respectively. The simulation model consists of the AR-coated single lens; the extension thickness was fixed at $L/R = 0.34$.

Parameter H of Fig 5.1(A) is defined as the length from the hemispherical lens center to top of the planar part. This scheme has the following advantages:

1. stronger lens array with increasing thickness of the planar part.

2. reduced machining time for fabrication.

3. easy fabrication of the anti-reflection (AR) coating.

Figure 5.3 shows the gap height H dependence of 220-GHz (λ = 1.36 mm) beam patterns and half-power beam width. Lens diameters of 1.2λ, 2λ, and 3λ were calculated. From Fig. 5.3, when the gap height H becomes thick, the side-lobe level increases and the beam width broadens. Side-lobe level below -15 dB can be obtained when $H/R \leq 0.6$.

Both silicon substrate and the planar part of the lens array should be at least 200 μm thick to facilitate easy handling. When $L/R = 0.34$, $H/R = 0.6$, and $L + H = 400$ μm,

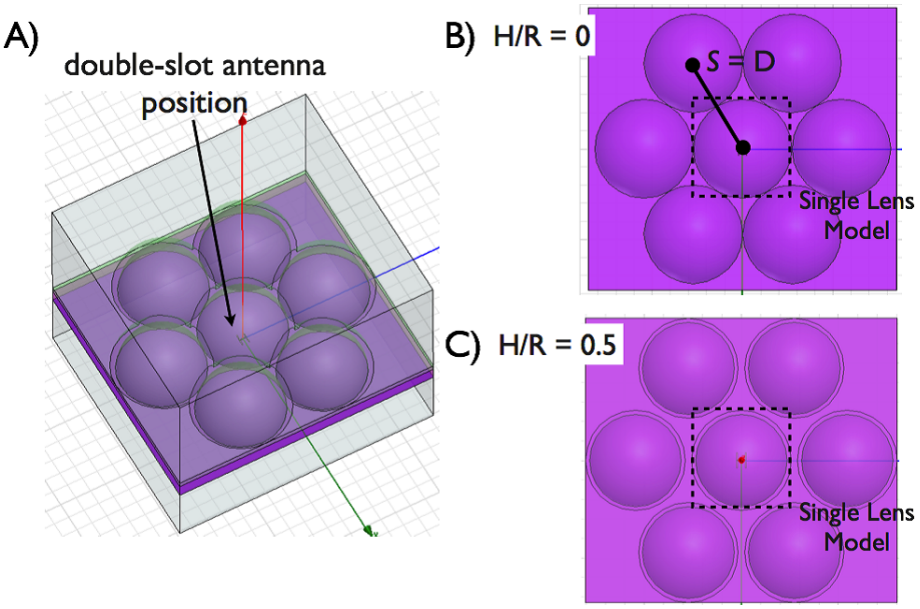

Figure 5.4: (**A**) Simulated model of an integrated silicon lens array with HFSS. The beam patterns were calculated in term of the center lens. Top view of the simulated model of (**B**) $H/R = 0$ and (**C**) $H/R = 0.525$. The pixel spacing was equivalent to the lens diameter.

minimum diameter lenses of 2.4λ and 4.3λ for 850 and 1500 GHz, respectively, can be fabricated.

5.3 Effects of the Surrounding Lenses on Beam Pattern

To design the silicon lens array for the 220-GHz MKID camera, we calculated the beam pattern of the close-packed array considering the effects of the surrounding lenses. Figure 5.4 shows the simulated model of an AR coated integrated silicon lens array with HFSS. The beam patterns were calculated in term of the center lens. The simulation conditions were as follows: 1) the pixel spacing was equivalent to the lens diameter and 2) extension thickness L/R was 0.34. The 1.2λ-, 2λ-, and 3λ- (λ = 1.36 mm) diameter lenses and their frequency dependence were calculated. The close-packed array was designed on the basis of the calculation results in Section 5.2. The gap height H was optimized to achieve symmetrical beam patterns, side-lobe level < -15 dB, and cross-polarization level < -15 dB. Figure 5.5 shows the simulation results of the beam patterns of the close-packed silicon lens array with $H/R = 0.525$ for several lens diameters. Good-quality beams were obtained with lens diameters of 1.2λ, 2λ, and 3λ in the bandwidth of $210-230$ GHz. A

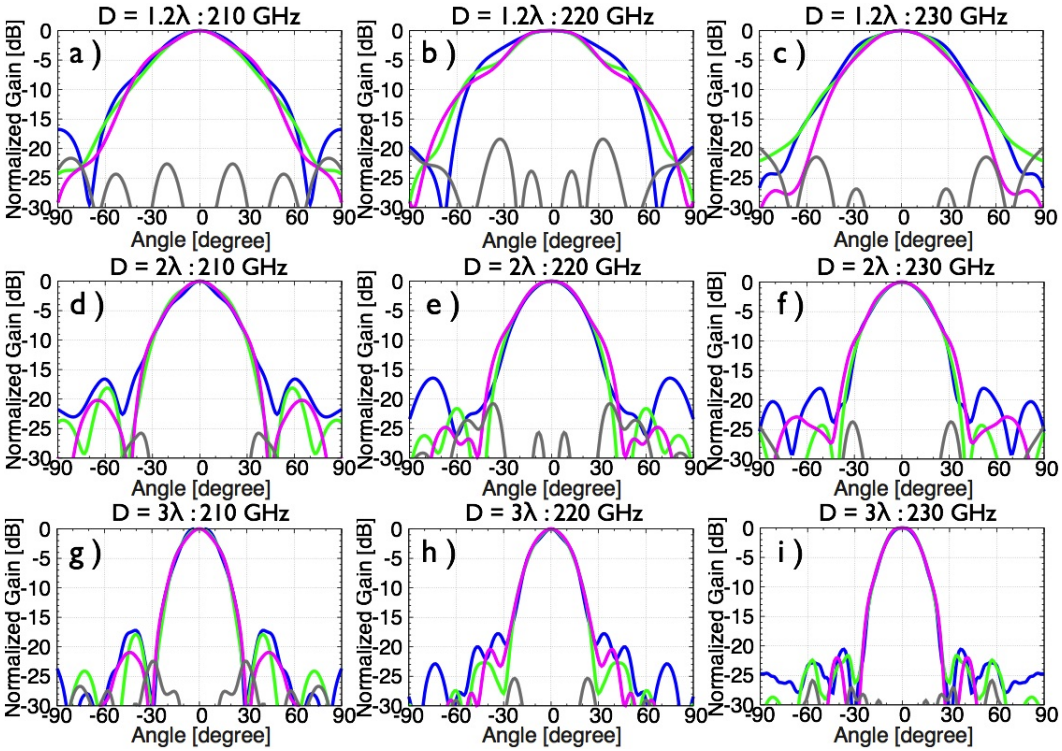

Figure 5.5: Beam pattern of close-packed silicon lens antenna with $H/R = 0.525$. (**a**), (**b**), and (**c**) correspond to the 210-, 220-, and 230-GHz beam patterns, respectively, of the 1.2λ-diameter lens. Blue, green, pink, and gray lines correspond to the co-polarization of E-, D-, and H-planes and the cross-polarization of D-plane, respectively. (**d**),(**e**),(**f**) and (**g**),(**h**),(**i**) are the same results with 2λ- and 3λ-diameter lenses, respectively.

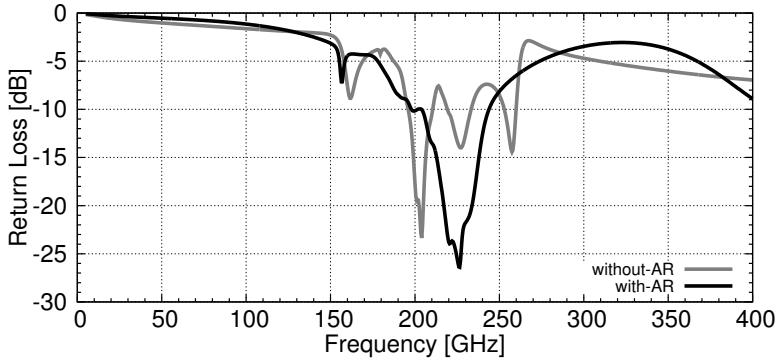

Figure 5.6: The return loss (S_{11}) of the close-packed silicon lens array fed by the double-slot antenna in the 220-GHz band calculated with HFSS. The parameters of the lens array were D = 1.2λ, $L/R = 0.34$ and $H/R = 0.525$. Black and gray lines correspond to the simulated model with and without AR coating, respectively. The result of without AR coating model see the effect of a standing wave.

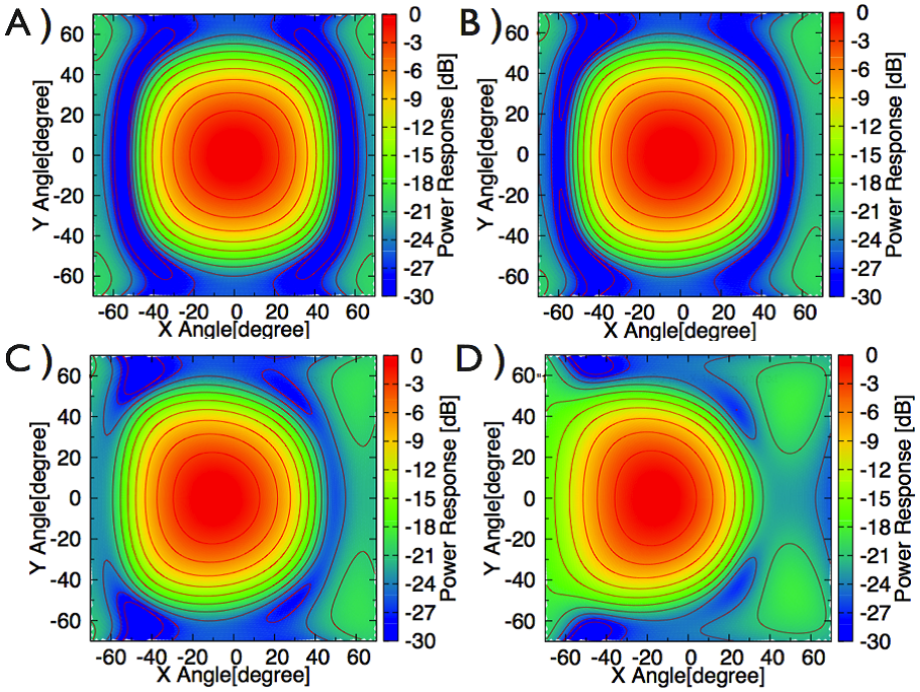

Figure 5.7: The simulated beam patterns of the extended hemispherical silicon lens as a function of the antenna position. (**A**), (**B**), (**C**) and (**D**) showed the antenna displacements (δ) from center position of 0, 25, 50 and 100 μm, respectively. The parameters of lens were D = 1.2λ, L/R = 0.34 and H/R = 0.

slight asymmetry in the main beam is possibly caused by interference of the electric field with the surrounding lenses. Making the pixel spacing narrower than the lens diameter caused the beam pattern profile to become worse.

Figure 5.6 shows the return loss (S_{11}) of the close-packed silicon lens array fed by the double-slot antenna in the 220-GHz band. Black and gray lines correspond to the simulated model with and without AR coating, respectively. If the AR coating layer is not used, the standing wave of the return loss is caused by the multiple reflections.

5.4 Alignment between Lens and Double-Slot Antenna

Misalignment between the silicon lens and the double-slot antenna causes larger beam ellipticity, beam center displacement, and larger cross-polarization level. To study the effects of the misalignment, we calculated the beam pattern using *HFSS*. The simulation conditions were as follows: 1) the simulation model consisted of an AR-coated single silicon lens fed by a double-slot antenna and 2) extension thickness L/R was approximately

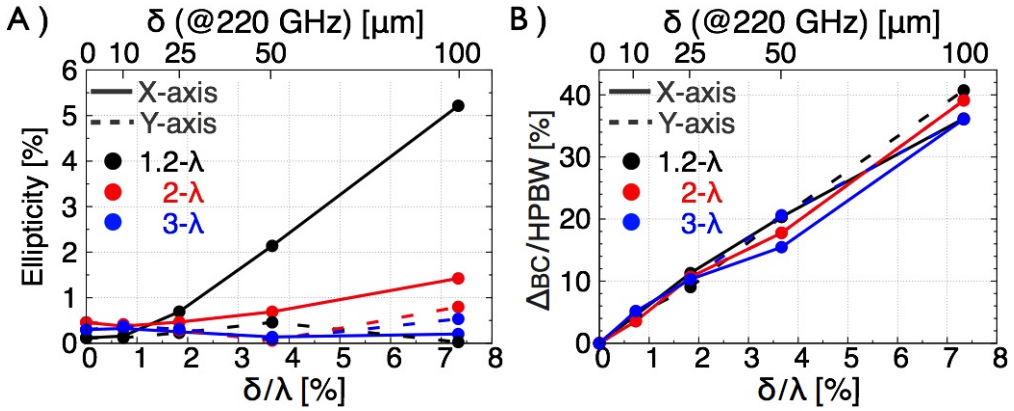

Figure 5.8: Simulated results of (**A**) beam ellipticity and (**B**) beam center direction (Δ_{BC}) as functions of the antenna displacement (δ). Black, red, and blue lines correspond to the 1.2λ-, 2λ-, and 3λ-diameter lenses, respectively, and the solid and dashed lines correspond to the displacement in the X and Y directions, respectively.

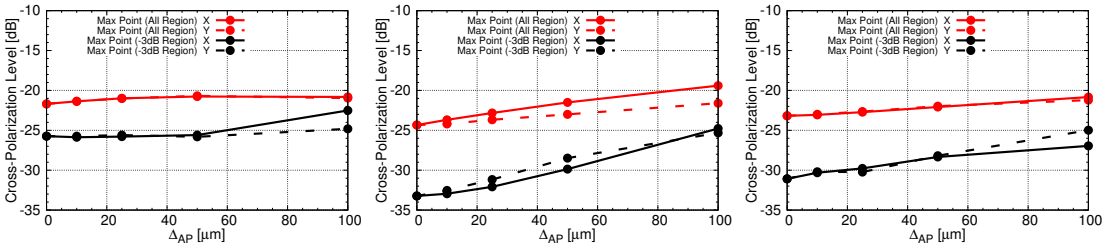

Figure 5.9: The simulated cross-polarization level as a function of the antenna position. Left, middle and right panels correspond to the 1.2λ-, 2λ-, and 3λ-diameter lenses, respectively. Red and black points showed the maximum cross-polarization level at the all region and the main beam (inside $-$ 3 dB level of the co-polarization beam) region, respectively. Solid and dashed lines correspond to the displacement in the X and Y directions, respectively.

0.34. Antenna displacements (δ) of 0, 10, 25, 50 and 100 μm (δ/λ = 0, 0.7, 1.8, 3.7 and 7.3% for 220 GHz) were calculated. The displacements in the X and Y directions, as shown in Fig. 5.1(B), were considered.

Figure 5.7 shows the simulated beam patterns of the extended hemispherical silicon lens as a function of the antenna position. (**A**), (**B**), (**C**) and (**D**) showed the antenna displacements (δ) from center position of 0, 25, 50 and 100 μm, respectively. As shown in the results, the increasing of antenna displacement induces large beam ellipticity, beam center displacement, and large sidelobe-level.

Figures 5.8(A) and (B) show the simulation results of beam ellipticity and beam center

direction as functions of antenna displacement. Beam ellipticity (ϵ) was calculated by two-dimensional Gaussian fitting, based on the definition $\epsilon = (a - b)/(a + b)$, where a and b are the major and minor axes, respectively. From the simulations, when the lens size is smaller, the misalignment between the lens and double-slot antenna in the X direction has a larger effect on the beam pattern. Ellipticity below 1% and cross-polarization level below -20 dB were achieved by keeping the alignment error below $\delta/\lambda = 1.8\%$ (δ = 25, 6, and 4 μm for 220, 850, and 1500 GHz, respectively) for each lens diameter.

Figure 5.9 shows the simulated cross-polarization level as a function of the antenna position. Left, middle and right panels correspond to the 1.2λ-, 2λ-, and 3λ-diameter lenses, respectively. The larger antenna displacement induces the large cross-polarization level. In case of the alignment error below $\delta/\lambda = 1.8\%$, however, the misalignment effect on the cross-polarization level was negligible.

6

Antireflection Coating for Cryogenic Silicon and Alumina Lenses

This chapter includes material accepted for publication in Journal of Low Temperature Physics, as "Anti-Reflection Coating for Cryogenic Silicon and Alumina Lenses in Millimeter-Wave Bands"
by T. Nitta, S. Sekiguchi, Y. Sekimoto, K. Mitsui, N. Okada, K. Karatsu, M. Naruse, M. Sekine, H. Matsuo, T. Noguchi, M. Seta, and N. Nakai

6.1 Introduction

Silicon and alumina lenses with high refractive indices are widely used for low temperature detectors at millimeter-/submillimeter-wave bands, and their re-imaging optics (Baryshev et al., 2011; Fowler et al., 2007; Tomaru et al., 2012). It can be used to realize a CCD-like camera with MKIDs and lens array, and a fast diffraction-limited field-of-view optics in a relatively compact package. A dielectric lens with high refractive index for focusing device becomes thinner than that with a low refractive index, leading to lower mass/volume and lower loss if an appropriate anti-reflection (AR) coating is applied. AR coatings are critical for dielectric lenses with high refractive indices, such as silicon, because such high refractive indices cause reflections of approximately 30% at each material/vacuum interface as shown in the following equation:

$$R = \frac{(n_r - 1)^2}{(n_r + 1)^2} = \frac{(3.388 - 1)^2}{(3.388 + 1)^2} = 0.296, \tag{6.1}$$

where refractive index (n_r) of silicon of 3.388 was used. So far, there are studies on various AR coatings at millimeter-wave bands with epoxy (Suzuki et al., 2012; Rosen et al., 2013) and Cirlex (Lau et al., 2006) and at terahertz bands with parylene (Gatesman et al., 2000; Hübers et al., 2001) as well as bulk meta-materials containing subwavelength features (Kamizuka et al., 2012). We study two types of AR coatings for cryogenic silicon and alumina samples at the millimeter-wave (220 GHz) band.

At normal incidence, surface reflection from the dielectric material at a particular wavelength (λ) can be made zero when

$$n_{AR} = \sqrt{n}, \tag{6.2}$$

$$d_{AR} = \frac{(2m+1)\lambda}{4n_{AR}} \qquad (m = 0, 1, 2, \cdots), \tag{6.3}$$

where n_{AR} and n correspond to the refractive indices of the AR coating and dielectric material, respectively, and d_{AR} is the thickness of the AR coating.

In case of silicon, the refractive index and thickness of AR coating layer are obtained by using n = 3.38;

$$n_{AR} = 1.84. \tag{6.4}$$

Table 6.1: Refractive index and suitable thickness of the materials for AR coating.

	Refractive Index	AR thickness@220 GHz [μm]	Reference
Kapton / Cirlex	1.84	185	Lau et al. (2006)
TMM 3	1.81	188	Tran & Page (2009)
Parylene D	1.62	205	Gatesman et al. (2000)
Stycast 1266	1.68	203	Tran & Page (2009)
Stycast 2850FTJ	2.2	155	Halpern et al. (1986)

$$d_{AR} = 185\ \mu\mathrm{m}. \tag{6.5}$$

Also in case of alumina (n = 3.11), the refractive index and thickness of AR coating layer are n_{AR} = 1.76 and d_{AR} = 193 μm, respectively.

6.2 Epoxy Based Anti-Reflection Coating

Refractive index and suitable thickness of the materials for AR coating are summarized in Tabel 6.1. However, conventional coatings have a few problems as follows.

1. In case of Kapton coating, it is difficult to form the lens shape. In addition, Kapton coating has a concern about a break-up of lens and coating during thermal cycling because the silicon and the coating have different coefficients of thermal expansion.

2. The parylene coating is very expensive because the thickness of coating layer is too thick for using in the millimeter-wave band.

3. Other materials do not have refractive index for perfect matching.

Recently, AR coating with mixtures of various epoxies has been reported (Suzuki et al., 2012; Rosen et al., 2013). We tested the AR coating for silicon and alumina with Emerson and Cuming's Stycast 1266 and Stycast 2850FTJ. Mixed epoxy coatings have a few advantages over other conventional coatings as follows.

1. An intermidiate refractive index ($n_{1266} < n_{int} < n_{2850FTJ}$) is obtained by mixing Stycast 1266 ($n_{1266} \sim 1.68$) with Stycast 2850FTJ ($n_{2850FTJ} \sim 2.2$).

2. Thickness of the epoxy coating layer can be precisely controlled by direct machining.

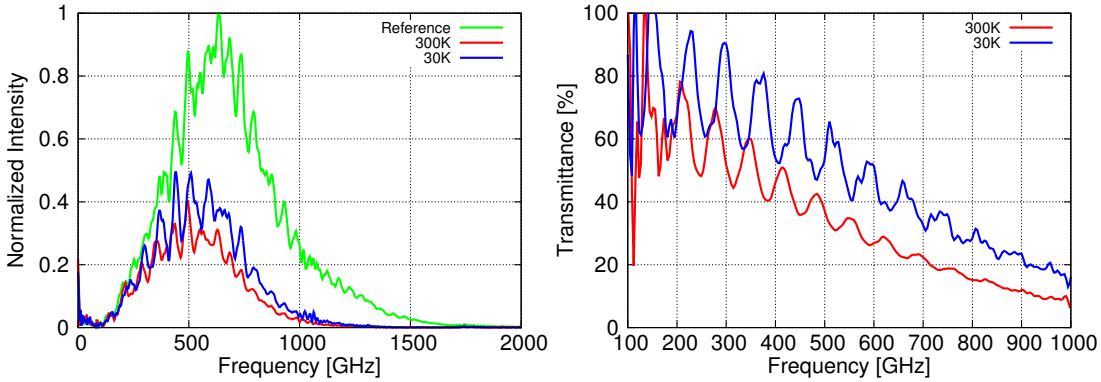

Figure 6.1: (*Left*) The measured frequency spectrums of reference (green line), Stycast epoxy at ambient temperature (red line) and Stycast epoxy at cryogenic temperature (blue line) with Fourier transform spectrometer. (*Right*) The transmittance of the Stycast epoxy at millimeter/submillimeter-wave range. Blue and red lines correspond to 30 K and 300 K data, respectively.

3. A dielectric lens and a epoxy coating do not separate easily because of its adhesion properties.

Catalyst 23LVJ was used in Stycast 2850FTJ preparation. Stycast1266 has only one curing agent (Stycast 1266B). For the mixing ratio we followed each product's data sheets. Before application, the mixed epoxies were vacuum degassed at ambient temperature for about 10 minutes. After degassing, a molded flat samples for refractive index measurements were cured at ambient temperature for 24 hours.

6.2.1 Optical Properties of Stycast Epoxies

The refractive index and dielectric loss tangent of the Stycast epoxies were measured at 30 K with a Fourier transform spectrometer (FTS). The FTS is the same measurement system as described in Chapter 3. The left panel of Fig. 6.1 shows the measured frequency spectrums of reference (green line), Stycast epoxy at ambient temperature (red line) and Stycast epoxy at cryogenic temperature (blue line). The sample was 1-mm-thick Stycast 2850FTJ. The transmission spectrums were obtained by dividing the frequency spectrums of sample by that of reference, as shown in the right panel of Fig. 6.1. Figures 6.2 and 6.3 show the refractive index and the dielectric loss tangent of Stycast 1266 and 2850FTJ, respectively. The samples were measured at 30 K and 300 K. The error bars are 1-σ error, which was determined by the multiple transmittance measurements. Large error bars of

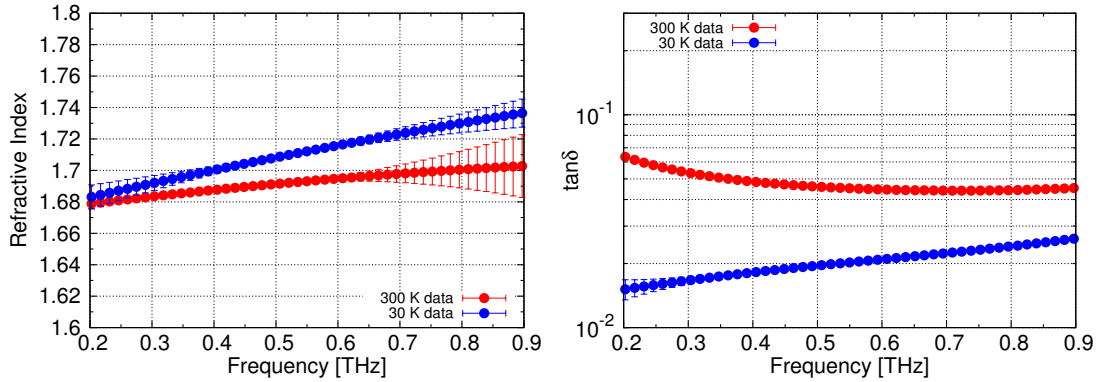

Figure 6.2: (*Left*) Refractive index and (*Right*) dielectric loss tangent measurement results of Stycast 1266. Blue and red lines correspond to 30 K and 300 K data, respectively.

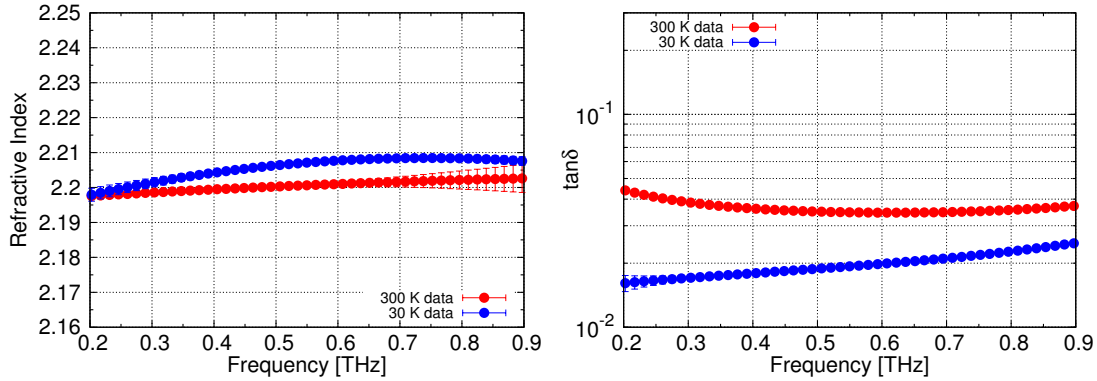

Figure 6.3: (*Left*) Refractive index and (*Right*) dielectric loss tangent measurement results of Stycast 2850FTJ. Blue and red lines correspond to 30 K and 300 K data, respectively.

refractive indies around 0.8 THz were due to the low signal-to-noise ratio of Fably-Pelot fringes, as shown in the right panel of Fig. 6.1. Dielectric losses of the Stycast epoxies were large at cryogenic temperatures, tan$\delta \approx 0.016$ at 220 GHz, which are higher than that of Cirlex at room temperature (Lau et al., 2006). However the absorption loss is not an issue as the coating is thin of few hundreds μm.

The temperature dependence of the refractive index and dielectric loss tangent of Stycast 1266 at 1 kHz between 0.07 and 300 K has been reported (Barucci et al., 1999). From their results, the measured refractive index and dielectric loss tangent behave smoothly even at extremely low temperature below 0.1 K. Therefore, we expect that the dielectric loss of mixed epoxy has no sharp transition and no drastic change at lower temperatures.

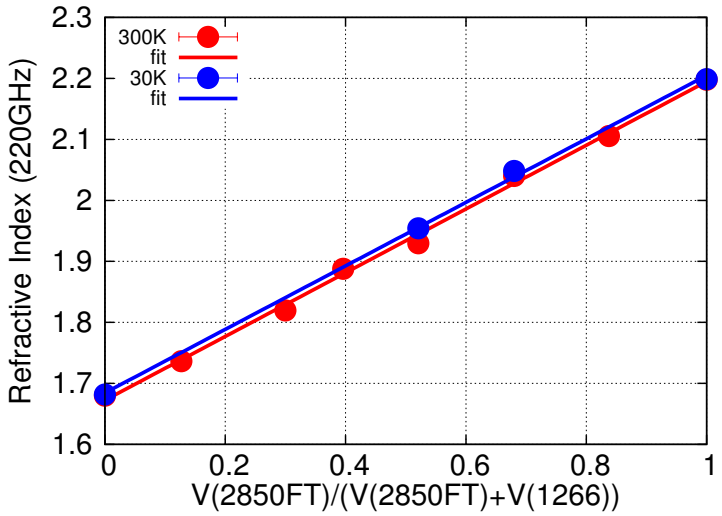

Figure 6.4: Measured refractive indices of mixed Stycast 1266 with Stycast 2850FTJ. Intermediate refractive indices were linearly varied as functions of volume ratio. Blue and red points correspond to measured data at cryogenic and ambient temperatures, respectively, and solid lines indicate linear fits.

6.2.2 Refractive Index Control

Some samples of various volume ratios were fabricated to measure the intermediate refractive indices of mixed epoxy. The refractive indices of mixed Stycast 1266 and 2850FTJ were varied linearly as functions of the volume fraction of Stycast 2850FTJ, as shown in Fig. 6.4. We were able to fabricate coating materials with a refractive index between 1.68 and 2.2. The measured refractive indices were not much difference between ambient and cryogenic temperatures. Here the volume fraction (r) is defined as:

$$r = \frac{V(2850FTJ)}{V(1266) + V(2850FTJ)}. \tag{6.6}$$

From the linear fitting of the measured data, mixed refractive index as a function of the volume fraction can be written as:

$$n_{mix,300K} = 0.5225r + 1.672. \tag{6.7}$$

$$n_{mix,30K} = 0.5205r + 1.684. \tag{6.8}$$

We also successfully obtained epoxies with mixed refractive indexes of 1.76 and 1.84,

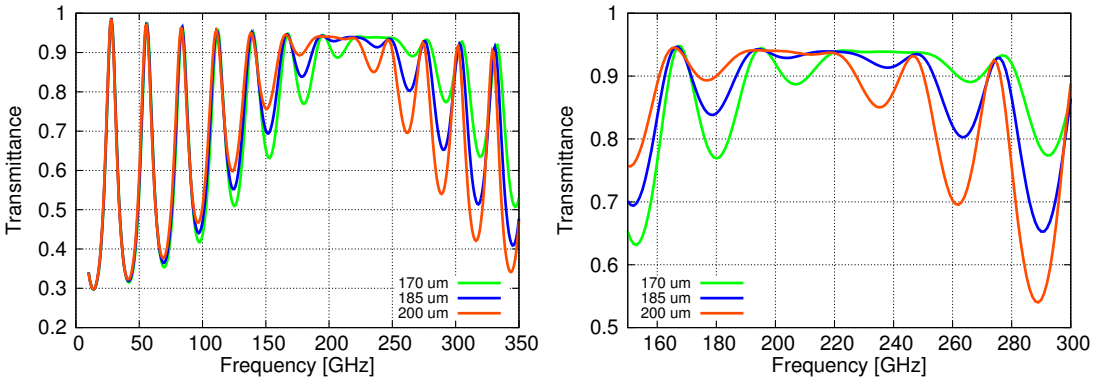

Figure 6.5: (*Left*) A comparison of simulated transmittance of various AR layer thickness. The simulation model included the dielectric loss tangent of AR layer material. (*Right*) Extended figure around 220 GHz. The thickness error affects the shift of the flat region. The tolerance of the AR layer thickness is $\pm$ 15 μm for design value (d_{AR} = 185 μm).

which matches for alumina and silicon.

6.2.3 AR Coating on Flat and Lens Samples

To test the AR coating at the 220-GHz band, we applied a layer of coating made from mixed epoxies on a 2.4-mm-thick flat silicon sample. In addition, to confirm the control of the mixed refractive index, another mixed epoxy AR coating was applied on a 2-mm-thick flat alumina sample. Silicon and alumina were the same high-purity samples as measured in Chapter 3.

Figure 6.5 shows a transmittance of various AR layer thickness simulated with HFSS. Its model consisted of both-side coated 2-mm-thick flat silicon. As shown in the right panel of Fig. 6.5, the thickness error affects the shift of the flat region. The tolerance of the AR layer thickness is $\pm$ 15 μm for design value (d_{AR} = 185 μm).

The AR coating for high-purity polycrystalline silicon lens array was fabricated, as shown in Fig. 6.6. The mixed epoxy coating on the silicon lens array was directly machined using a high-speed spindle on an ultraprecision machine in a similar way to that for a silicon lens array; thus, the shape and thickness of the epoxy AR coating were precisely controlled. The mixed epoxy was thickly (approximately 1 mm thick) spread on the lens array. The excess epoxy on the lens array was quickly cut with large diameter (e.g. 3 $-$ 5 mm) square end-mill, which did not affect on total machining time. The time consuming process is to make lens shapes of the epoxy with quarter-wavelength thick-

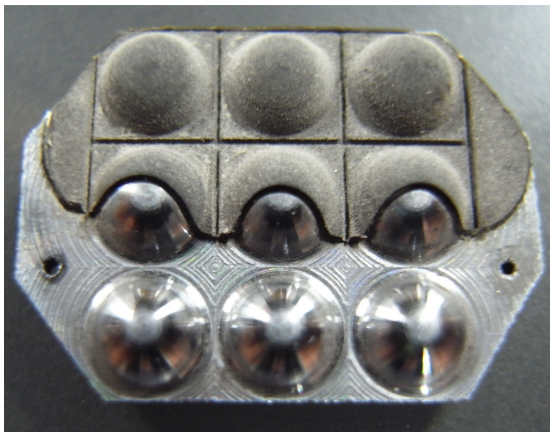

Figure 6.6: Photograph of an epoxy-coated nine-pixel silicon lens array. For demonstration, epoxy AR coating was applied to the upper half of the lens array. Machining tools for the AR coating were made of TiAlN-coated ceramic end mill with radii of 0.5, 0.3, and 0.15 mm. Slits between lens pixels relaxed the thermal stress between silicon and epoxy.

Table 6.2: Design and measured epoxy AR layer thickness of various samples.

	AR thickness (Design) [μm]	AR thickness (Measured) [μm]	Surface roughness (r.m.s.) [μm]
Flat Silicon (Side 1)	185	188	1.1
Flat Silicon (Side 2)	185	186	0.7
Flat Alumina (Side 1)	193	194	0.5
Flat Alumina (Side 2)	193	192	1.1
Silicon Lens Array	185	199	5.3

ness of 185 μm with small diameter end-mills. As shown in Fig. 6.6, the epoxy coating on the lens array has slits between the lenses, which prevent the lens from breaking as silicon and epoxy have different thermal expansion coefficients. It was confirmed that the epoxy-coated lens array had no degradation after several thermal cycles to 0.3 K.

Table 6.2 shows the design and measured AR coating thickness of the flat silicon, flat alumina, and silicon lens array. Surface profile of three lenses in one direction was measured by using a non-contact three-dimensional measuring machine. The measured AR thicknesses varied $197 - 201$ μm, and the average value was shown in Table 6.2. The variation in measured thickness may be caused by wear of end-mills, position reproducibility of end-mills and misalignment between the center position of lens and AR coating. The position reproducibility of the machine was around 50 nm, and the alignment accuracy

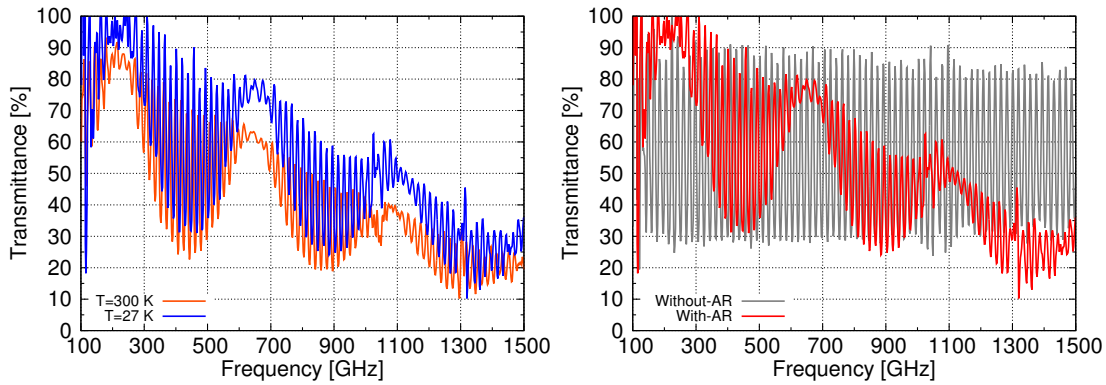

Figure 6.7: (*Left*) Measured transmittance of the 2.4-mm-thick flat epoxy-coated silicon. Epoxy was coated on both sides. Blue and orange lines correspond to the cryogenic temperature (27 K) and ambient temperature, respectively. Reduction in transmittance with increasing frequency was due to the increasing loss in the epoxy AR coatings. (*Right*) The comparison of the measured transmittance of a flat bare-silicon sample (gray line) and a flat epoxy-coated silicon sample (red line).

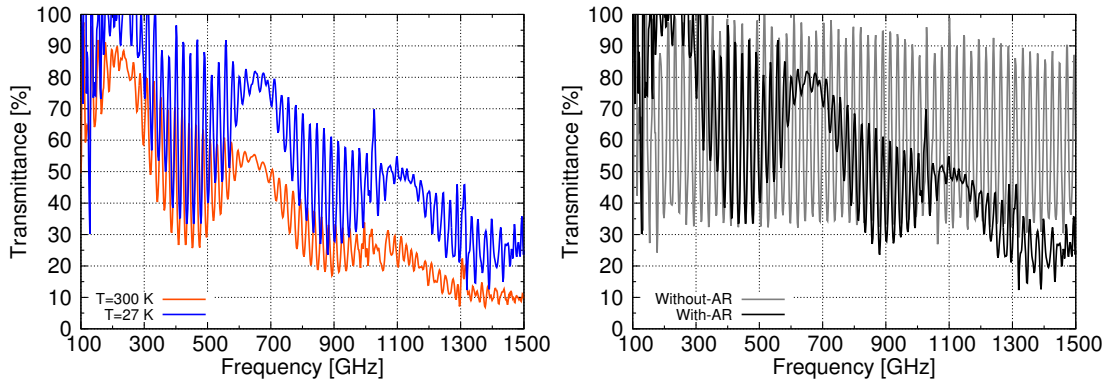

Figure 6.8: (*Left*) Measured transmittance of the 2-mm-thick flat epoxy-coated alumina. Epoxy was coated on both sides. Blue and orange lines correspond to the cryogenic temperature (27 K) and ambient temperature, respectively. Reduction in transmittance with increasing frequency was due to the increasing loss in the epoxy AR coatings. (*Right*) The comparison of the measured transmittance of a flat bare-alumina sample (gray line) and a flat epoxy-coated alumina sample (black line).

between the center position of lens and AR coating was less than 10 μm.

The fabrication error of the AR coating thickness for the flat samples and lens array were less than 3 μm in rms and approximately 10 μm in rms, respectively. The surface roughness of the top of the lens was less than 6 μm in rms. The surface roughness of the epoxy-coated silicon lens array was affected by grain particles in the epoxy. These values were sufficiently small for application in the millimeter-wave range.

The left panel of Fig. 6.7 and Fig. 6.8 show the measured transmittance of the epoxy-coated flat silicon and alumina samples. The blue and orange lines correspond to cryogenic and room temperatures, respectively. High transmittance near 220, 660, and 1100 GHz was due to the $\lambda/4$-, $3\lambda/4$- and $5\lambda/4$-thick AR coatings. Reduction in transmittance with increasing frequency was due to the increasing loss in the epoxy AR coatings. The measured 220-GHz-band transmittance at 27 K was $95 \pm 2\%$ with a bandwidth of 25%. The loss of approximately 5% was caused by the absorption in the epoxy AR coatings. This value is consistent with the measured dielectric loss tangent which are summarized in Fig. 3.10. Also there is a small ripple in the transmittance at 220 GHz band of the flat epoxy coated silicon and alumina. As one of the possibilities, this ripple in the 220-GHz band may be caused by refractive index inhomogeneity of epoxy thin-layer after machining.

The right panel of Fig. 6.7 and Fig. 6.8 show the coated and uncoated transmittance of silicon and alumina samples. The interference fringes corresponding to the sample thickness of uncoated transmittance are caused by multiple reflections within the samples, whereas the interference fringe disappears for the coated samples.

The AR thickness is practically limited to 30 μm. So, it is possible to apply this technology to THz range. For terahertz applications, AR thickness and absorption loss in the epoxy AR coatings at 1.2 THz are 34 μm and approximately 11%, respectively.

6.3 Sub-wavelength Structures as an Anti-Reflection Coating

When we use the large-diameter dielectric lens, the epoxy AR coatings have concerns about thermal stress. A large-diameter dielectric lens with the coating has a possibility to separate AR coating from lens during thermal cycling because the alumina (or silicon) and the Stycast epoxy have different coefficients of thermal expansion. To solve these issues, we designed antireflective sub-wavelength structures (SWSs) for controlling the refractive index.

In general, thin film coatings have been used to reduce reflections at dielectric surface, but recently the antireflective sub-wavelength structures have been proposed (Raguin & Morris, 1993). For antireflective structures, several types such as groove (Wagner-Gentner et al., 2006), hole (Biber et al., 2003), pillar (BrŘckner et al., 2009) and moth-eye (Kamizuka

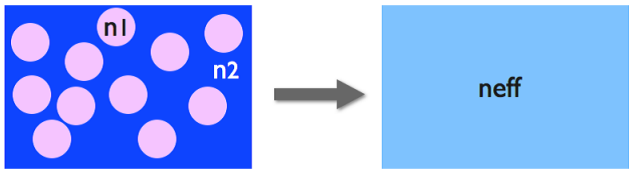

Figure 6.9: The schematic view of the effective medium theory.

Figure 6.10: Cross-sectional view of the effective medium theory. A sub-wavelength structure can be regarded as a homogenous dielectric layer with an effective refractive index.

et al., 2012) have been developed at millimeter-wave to terahertz range.

6.3.1 Effective Medium Theory

Effective medium theory discusses a complex mixture with respect to a spatially homogeneous electromagnetic response (Bruggeman, 1935). If the structure size is smaller than the target wavelength, scattering effects of structure are negligible and quasi-static models are adequate. Figure 6.9 shows the schematic view of the effective medium theory. As shown in Fig. 6.9, periodic structures in subwavelength scale are regarded as homogeneous media with effective refractive indices determined by the volume filling factor (= diameter/period of the structures). In case of alumina, as shown in Fig 6.10, it is expected that we obtain the medium whose effective refractive index of $n_{vacuum} < n_{eff} < n_{alumina}$. Thus, the effective medium act as antireflective layers.

6.3.2 Design

We studied two types of sub-wavelength structures, cylindrical hole and rectangular pillar, on cryogenic flat alumina samples. Figure 6.11 shows the unit cell of a cylindrical hole and a rectangular pillar structures. The filling factor (f) is defined as

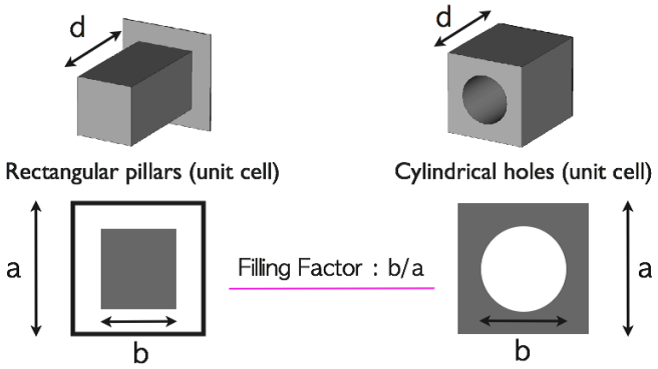

Figure 6.11: The definition of the filling factor for a rectangular pillar and a cylindrical hole structures (Biber et al., 2003).

$$f = \frac{b}{a}, \tag{6.9}$$

where a and b correspond to a period and diameter of structures, respectively. d is a depth of structures. The effective refractive index ($n_{vacuum} < n_{eff} < n_{alumina}$) is obtained by changing the filling factor.

Cylindrical Holes and Rectangular Pillars

The period of a SWS must be smaller than the target wavelength for not energy being lost to higher-diffraction-orders. In other words, the period of a SWS must hold the following relation to propagate only the zeroth-diffraction-orders (BrŘckner et al., 2009):

$$\frac{a}{\lambda} \leq \frac{1}{n_{air}\sin\theta\cos(\phi-\delta) + \sqrt{n_{al}^2 - n_{air}^2\sin^2\theta\sin^2(\phi-\delta)}}, \tag{6.10}$$

where n_{air}, n_{al} and λ correspond to the refractive index of the air, the refractive index of alumina and wavelength, respectively. Also, θ, ϕ and δ correspond to the polar angle of incidence, the azimuthal angle of incidence and the phase angle, respectively. For normal incidence (θ = 0°), the normalized period a/λ becomes

$$\frac{a}{\lambda} \leq \frac{1}{n_{al}}. \tag{6.11}$$

When a period a meets the Eq. 6.11, high-transmittance with no diffraction loss can

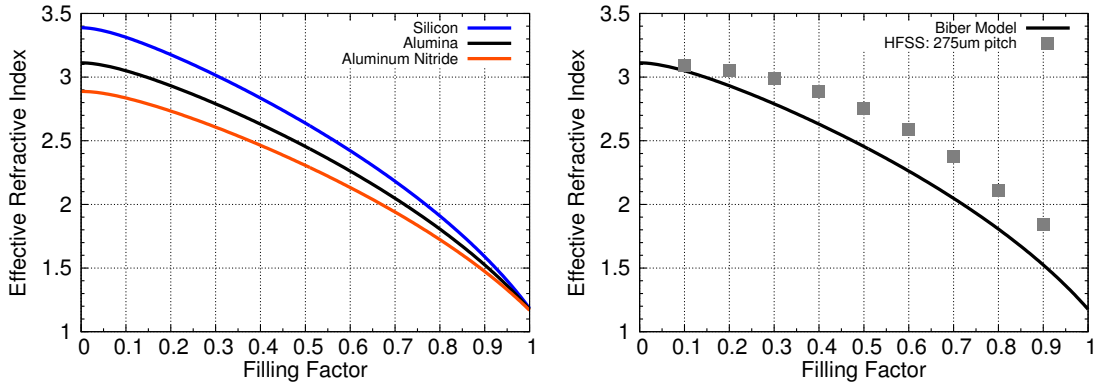

Figure 6.12: (*Left*) Effective refractive index of a cylindrical hole structure as a function of the filling factor, calculated by using Eq. 6.13. (*Right*) The comparison of the effective refractive index of Eq. 6.13 (solid line) and HFSS simulation (gray symbols) in the case of alumina. The structure period of HFSS simulated model was 275 μm.

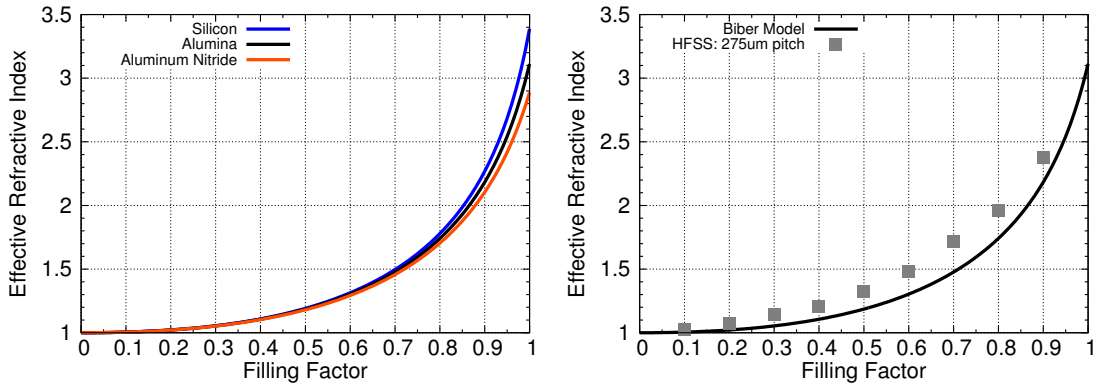

Figure 6.13: (*Left*) Effective refractive index of a rectangular pillar structure as a function of the filling factor, calculated by using Eq. 6.12. (*Right*) A comparison between the effective refractive index of Eq. 6.12 (solid line) and HFSS simulation (gray symbols) in the case of alumina. The structure period of HFSS simulated model was 275 μm.

be obtained.

According to Biber et al. (2003), the effective refractive indices of cylindrical hole and rectangular pillar structures are expressed by the field-equivalent circuit model which provides precise information about the effective refractive index as a function of the filling factor of the unit cell. By considering the parallel and series capacitors of unit cells, the effective refractive index is calculated easily. By using this model, the effective refractive index of rectangular pillar is determined as follows (Biber et al., 2003).

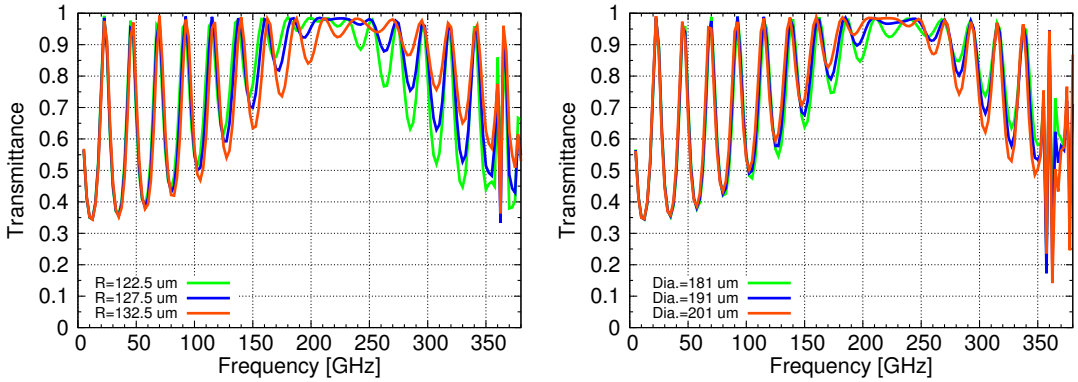

Figure 6.14: Comparisons of the simulated transmittance of various structure diameter. In the simulated geometry, period and depth were 275 and 193 μm, respectively. (*Left*) The results of a cylindrical hole structure. The tolerance of the structure diameter is $\pm$ 10 μm for design value (dia. = 255 μm). (*Right*) The results of a rectangular pillar structure. The tolerance of the structure diameter is $\pm$ 10 μm for design value (dia. = 191 μm).

$$n_{eff,Pillar} = \sqrt{\frac{\epsilon_0 d(\frac{a-b}{a} + \frac{bn_{al}^2}{(a-b)n_{al}^2+b})}{\epsilon_0 d}}, \tag{6.12}$$

where a, b and d correspond to a period, diameter and depth of a SWS, respectively. Also, ϵ_0 is permittivity of free space. Furthermore, the effective refractive index of cylindrical hole structure is determined as follows (Biber et al., 2003).

$$n_{eff,Hole} = \sqrt{\frac{\epsilon_0 n_{al}^2 \frac{(a-b)d}{a} + \int_{-\frac{b}{2}}^{\frac{b}{2}} \frac{\epsilon_0 n_{al}^2 d}{a+\sqrt{(\frac{b}{2})^2-x^2(2n_{al}^2-2)}} dx}{\epsilon_0 d}}. \tag{6.13}$$

The left panel of Fig. 6.12 and Fig 6.13 show the calculated effective refractive index of a cylindrical hole and a rectangular pillar structures as a function of filling factor for several different refractive indices of 2.88, 3.11 and 3.38. The refractive indices of 2.88, 3.11 and 3.38 correspond to aluminum nitride (AlN), alumina and silicon, respectively. In this calculation, SWSs with a periodicity smaller than $\lambda/10$ (quasi-static limit) were investigated. However, it is difficult to fabricate a cylindrical hole and a rectangular pillar structures with small period which is smaller than $\lambda/10$. When the SWS for 220-GHz band is designed, for example, a 275 μm ($\sim \lambda/5$) period leads to acceptable performance up to approximately 300 GHz, and this shape can be easily processed. In this condition, however, SWS design does not operate in the quasi-static limit ($a < \lambda/10$). Thus, the

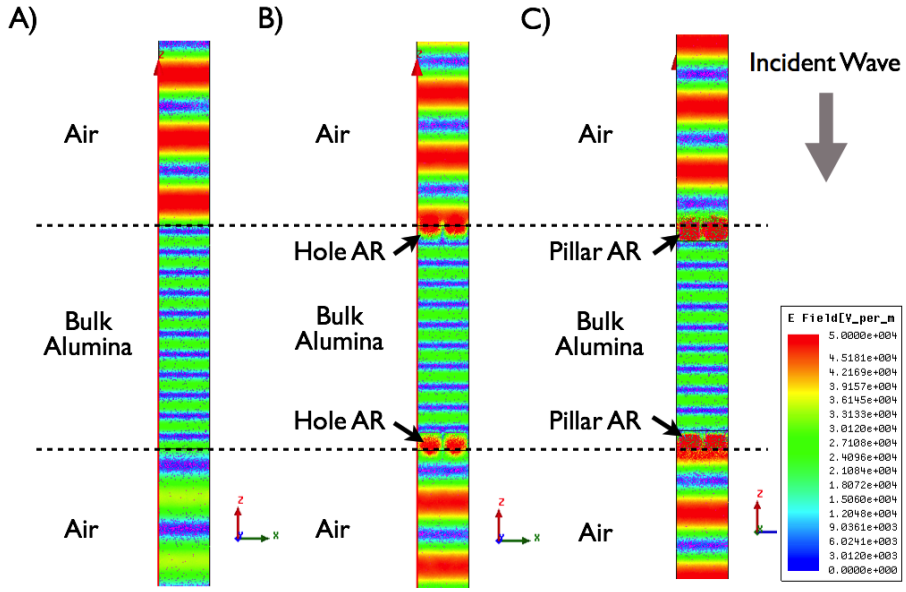

Figure 6.15: Electric field distribution inside the alumina. (**A**) A bare alumina. (**B**) A cylindrical hole structure. (**C**) A rectangular pillar structure.

effective refractive index of cylindrical hole and rectangular pillar structures with 275 μm period have been calculated by using the 3-D full-wave electromagnetic field simulator HFSS to optimize the geometry of our structures. A comparison between the effective refractive index of "Biber Model (Eqs. 6.12, 6.13)" and HFSS simulation are shown in Fig 6.12 and 6.13. As shown in the results, calculated effective refractive indices have a slight difference in two models.

Polynomial fitting results of simulated effective refractive index by HFSS for cylindrical hole and rectangular pillar are as follows;

$$n_{eff,Hole} = -1.7491f^2 + 0.1812f + 3.0978. \tag{6.14}$$

$$n_{eff,Pillar} = 5.4894f^4 - 7.3882f^3 + 4.3306f^2 - 0.3485f + 1.0094. \tag{6.15}$$

The transmittance of cylindrical hole and rectangular pillar structures were calculated by using optimized parameters at 220 GHz band. Figure 6.14 shows the simulated transmittance of various structure diameter. In the simulated geometry, period and depth were 275 μm and 193 μm, respectively. The tolerance of the structure diameter is $\pm$ 10 μm for design value. Figure 6.15 shows the electric field distribution inside the alumina. The

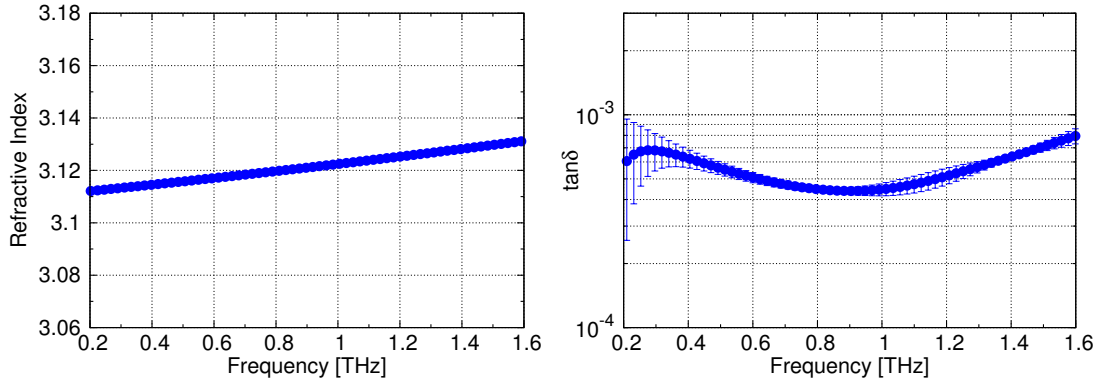

Figure 6.16: (*Left*) Refractive index and (*Right*) dielectric loss tangent measurement results of high-purity (4N purity) alumina for fabrication of sub-wavelength structures. The data were taken at 30 K.

transmitted energy of uncoated alumina (see (A)) was lost by surface reflection, whereas the transmitted energy of alumina with cylindrical hole and rectangular pillar (see (B), (C)) structures were without loss.

6.3.3 Fabrication

Cylindrical Holes

The measured refractive index and dielectric loss tangent of alumina for fabrication of sub-wavelength structures are shown in Fig. 6.16. A purity of alumina is 4N. Figures 6.17(A) and (B) show the antireflective cylindrical hole structures on 2-mm-thick flat alumina machined by YAG laser with 10 W output power at 532 nm. (A) and (B) correspond to the top view of the antireflective periodic cylindrical hole structures on a flat alumina surface and its cross section, respectively. It took approximately 20 min to process the holes over an area of 10 mm $\times$ 10 mm (manufactured by Oshima Prototype Engineering). The geometrical parameters of the antireflective structures were controlled to satisfy Equations 6.2 and 6.3, and were optimized for the 220-GHz band. The grid-type antireflective structures show same responses for both horizontal and vertical polarizations. The designed and measured parameters of the antireflective periodic cylindrical hole structures are summarized in Table 6.3. Measurements of a period, a hole diameter, a depth and a filling factor were made with a digital microscope.

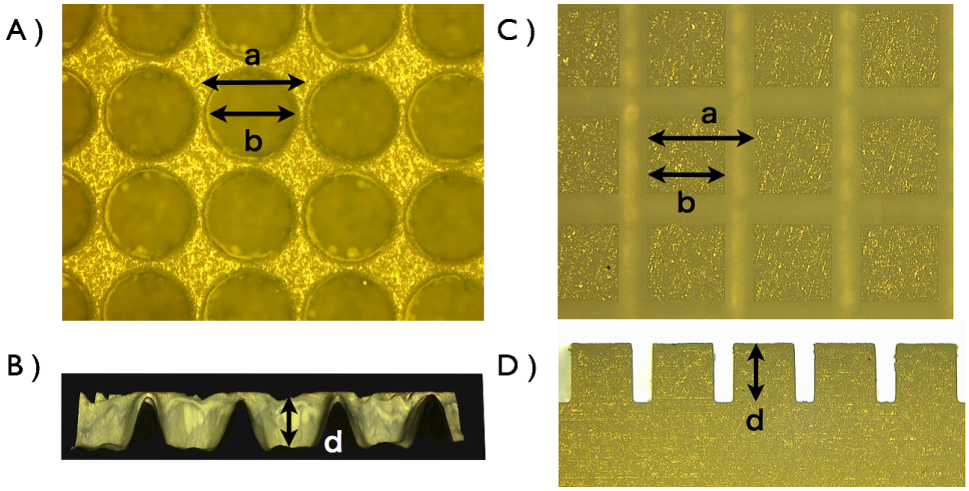

Figure 6.17: (**A**) Microscopic image of the antireflective periodic cylindrical hole structures on a flat alumina surface. (**B**) Cross section of the antireflective hole structures. (**C**) Microscopic image of the antireflective periodic rectangular pillar structures on a flat alumina surface. (**D**) Cross section of the antireflective pillar structures.

Rectangular Pillars

The antireflective rectangular pillar structures on 2-mm-thick flat alumina machined by dicing saw are shown in Fig. 6.17(C) and (D), which correspond to the top view of the antireflective periodic rectangular pillar structures on a flat alumina surface and its cross section, respectively. An edge shape of rectangular pillar is very sharp. The machining time of rectangular pillar structures was faster than that of cylindrical hole structures. The designed and measured parameters of the antireflective periodic rectangular pillar structures are summarized in Table 6.4. Typical mechanical error was less than 10 μm from the measurements.

6.3.4 Transmittance Measurement

The measured transmittance of alumina sample with cylindrical hole and rectangular pillar structures are shown in Fig. 6.18. The measured temperature was 25 K. In case of a cylindrical hole structure, the measured 220-GHz-band transmittance was above 90% with a bandwidth of 25%. The absorption loss of the sample at 220 GHz was 1%, which was derived from the measured dielectric loss tangent. The transmittance of the design configuration shows no ripples and flat transmittance at 220-GHz (see Fig. 6.14). How-

Table 6.3: Designed and measured parameters of the antireflective periodic cylindrical hole structures.

	Design / Measurement
Period : a [μm]	275 / 360
Hole Diameter : b [μm]	255 / 320
Hole Depth : d [μm]	193 / 190
Filling Factor : f	0.927 / 0.889
Cutoff Frequency [GHz]	350 / 280

Table 6.4: Designed and measured parameters of the antireflective periodic rectangular pillar structures.

	Design / Measurement
Period : a [μm]	275 / 275
Pillar Diameter : b [μm]	201 / 210
Pillar Height : d [μm]	193 / 190
Filling Factor : f	0.731 / 0.764
Cutoff Frequency [GHz]	350 / 320

ever, the small fringes were measured at approximately 220 GHz because the mismatch in the effective refractive indices was caused by the slope of sidewalls, which was made by machining errors. Transmittance was drastically reduced at frequencies higher than 300 GHz because most of the energy was scattered into higher diffraction orders. Thus, the antireflective structures act as low-pass filters. As shown in Table 6.3, measured cut-off frequency differ from the expected frequency. This is because the machined period and the hole diameter are bigger than the design value.

In case of a rectangular pillar structure, the measured 220-GHz-band transmittance was almost 100% with a bandwidth of 25% at 25 K. The comparison of the measured and simulated transmittance at millimeter-wave bands is shown in the right panel of Fig. 6.19. The measured transmittance is in good agreement with the calculations. Also the other parameters such as cutoff frequency are in good agreement with the expected value. The comparison of the measured transmittance of the antireflective hole and pillar structures is shown in the left panel of Fig. 6.17.

The advantages of antireflective sub-wavelength structure over a film coating are summarized as follows.

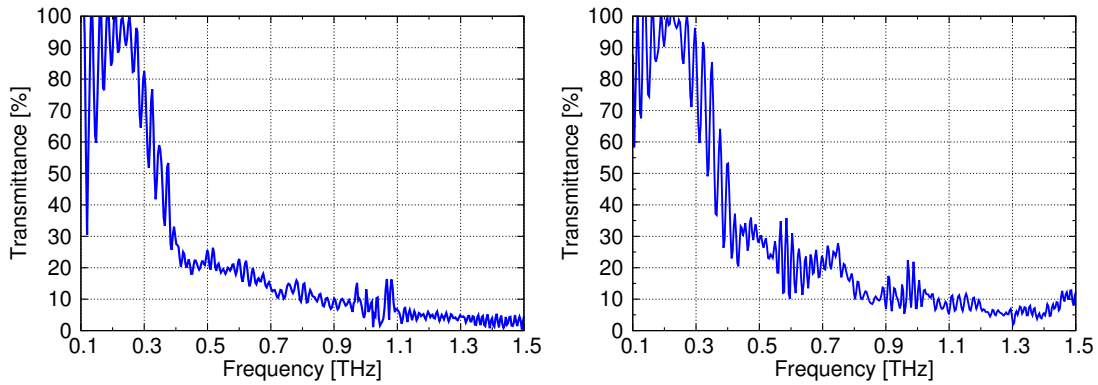

Figure 6.18: Measured transmittance of (*Left*) antireflective hole structures and (*Right*) antireflective pillar structures on the flat alumina samples at 25 K.

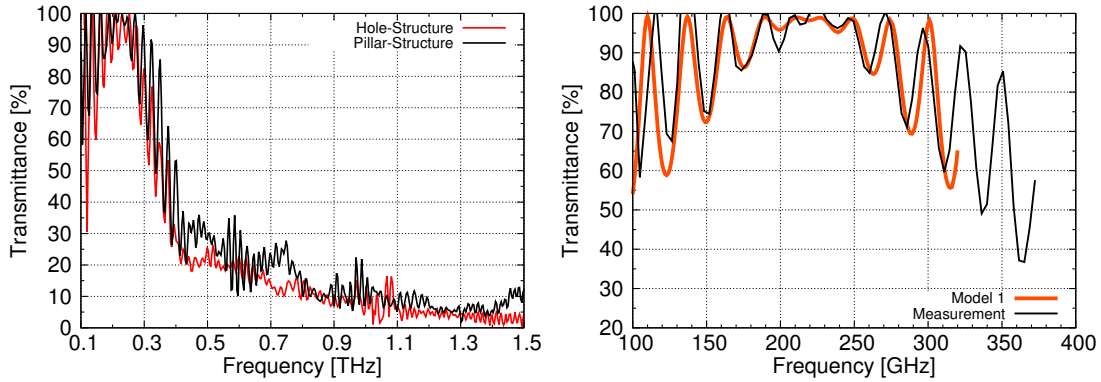

Figure 6.19: (*Left*) The comparison of the measured transmittance of the antireflective hole and pillar structures. (*Right*) The comparison of the measured and simulated transmittance of the antireflective pillar structures. Black and orange lines showed the measured and simulated results, respectively. In the simulated geometry, period of 275 μm, diameter of 210 μm and depth of 190 μm.

1. It is possible to obtain an antireflective effect with only one material.

2. The AR-coated lens has mechanical strength and robustness for thermal cycling.

3. There is no additional dielectric loss such as epoxy AR coatings.

4. It acts as a low-pass filter.

However, it is difficult to fabricate the antireflective structure on the lens array because of the small radius of curvature. Therefore, this antireflective structure is likely to be applicable to the large-diameter dielectric lenses used in re-imaging optics.

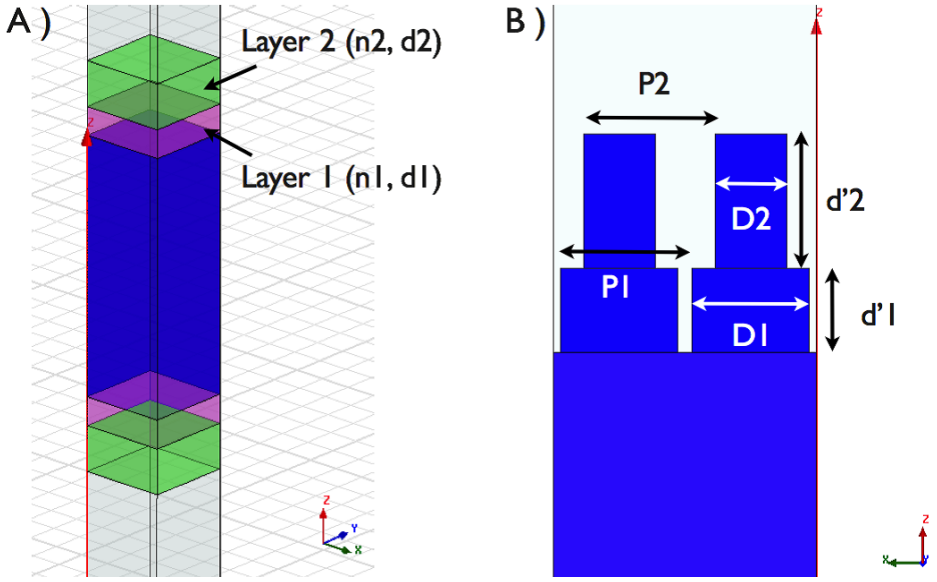

Figure 6.20: Two models of the broadband AR coating. (**A**) Two-layers of dielectric AR coating. (**B**) Two-layers of pillar-type sub-wavelength structure.

Table 6.5: Design parameters of two-layers dielectric AR coating and pillar-type sub-wavelength structure for an alumina sample (n = 3.112).

	Parameter	Design Value
Dielectric Layer	n1	2.23 (Suzuki et al., 2012; Rosen et al., 2013)
	n2	1.4 (Suzuki et al., 2012; Rosen et al., 2013)
	d1	181 μm (=λ/4n1; λ=1.62 mm, F=185 GHz)
	d2	287 μm (=λ/4n2; λ=1.62 mm, F=185 GHz)
Sub-wavelength Structure	P1	320 μm
	P2	320 μm
	D1	280 μm
	D2	170 μm
	d'1	177 μm
	d'2	281 μm

6.4 Broadband Design

A broadband AR effect can be realized by stacking of films with different refractive indices. For example, a multi-layer coating with mixtures of various epoxies has been developed (Suzuki et al., 2012; Rosen et al., 2013). Furthermore, a multi-layer sub-wavelength structure which has different filling factor at each layer also acts as multi-layer coating. Figure 6.20 shows the design of two-layers dielectric AR coating and pillar-type sub-

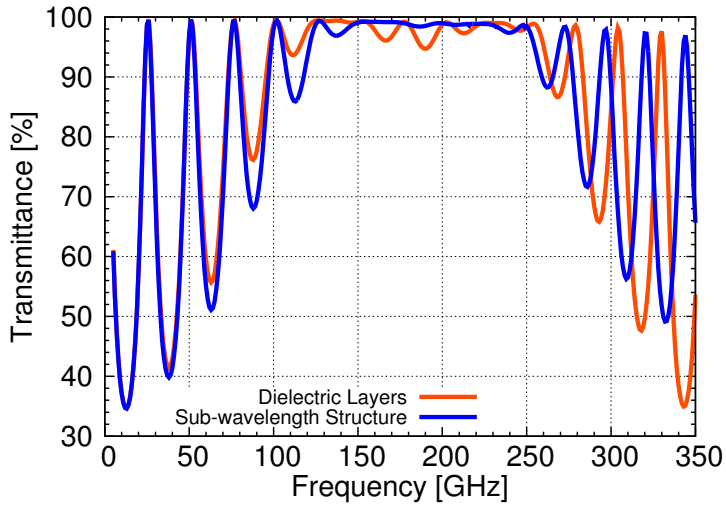

Figure 6.21: A comparison of simulated transmittance of two-layers dielectric AR coating and pillar-type sub-wavelength structure for an alumina flat sample.

wavelength structure for an alumina sample. Design parameters of each model are summarized in Table 6.5. These parameters were optimized to cover both 150-GHz band (130 — 170 GHz) and 220-GHz band (200 — 240 GHz). Simulated transmittance of both models are shown in Fig. 6.21. The transmittance of above 90% with bandwidth of approximately 70% can be achieved. This technology is important for various astronomical missions such as CMB polarization measurement (Datta et al., 2013) and imaging spectrograph for determining the redshift of distant galaxies (Endo et al., 2012).

7

Development of a Wide Field Camera System for Millimeter-Wave Observations

7.1 Introduction

In this chapter, we show about the development of wide field-of-view millimeter-wave camera system. The aim of the development of wide field-of-view camera system is to realize a wide-field observations for detecting a number of unknown distant galaxies. The camera system is composed of 608 pixel MKID camera for 220-GHz band and all-refractive re-imaging optics with silicon and alumina lenses. The MKID camera was designed based on a direct machined silicon lens array, a double-slot antenna coupled MKID, and an AR coating, which are described in previous chapters. The all-refractive re-imaging optics couples the F/# = 6 telescope focus to the F/# = 1 focal plane. The design, fabrication and evaluation results of a wide field-of-view millimeter-wave camera system are shown in this chapter.

7.2 Design of 608 pixels Camera

We adopted the mosaic design of MKID camera with a hexagonal shape as one module. In this case, several modules can be assembled into a larger array which fits the circular focal plane (Lee et al., 2008). The left panel of Fig. 7.1 shows the CAD drawing of the 608-pixel MKID camera with direct machined silicon lens array. A gold-plated copper frame has two SMA connectors for readout of the microwave signals, as shown in Fig. 7.1. The dimension of the 608 pixel camera is approximately 50 mm diameter. Metallic surface of the frame on the opposite side of the lens array is coated with a mixture of Stycast 2850FTJ, carbon black powder, and approximately 1 mm size silicon carbide grains to form an absorber in order to absorb stray light (Barends, 2009; Baselmans et al., 2012). A 608 pixel double-slot antenna coupled MKID array is made of aluminum film and high-resistivity silicon wafer. Epitaxial aluminum film was deposited on Si(111) wafer by using molecular beam epitaxy (Naruse, 2012). The CPW geometry of resonator had a 3 μm-wide central line and 2 μm-wide gaps. Bonding wires over the feed line were used to connect the ground-planes of the coplanar waveguides because the total feed line length is approximately 680 mm.

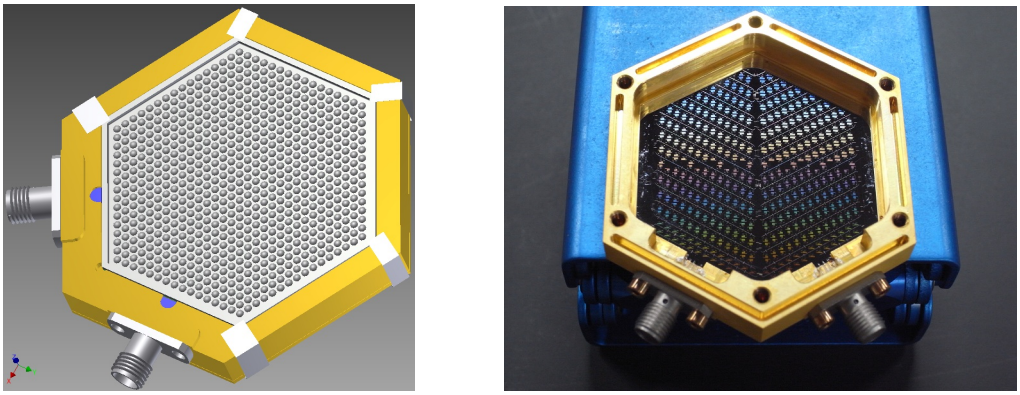

Figure 7.1: (*Left*) The CAD drawing of 220-GHz band 608-pixel MKID camera. (*Right*) The photograph of the frame and the 608 pixel MKID array.

Table 7.1: Processing conditions of the 721 pixel silicon lens array.

	Silicon Lens	Stycast AR Coating
Rotating Speed [rpm]	40000	40000
Rotation Unbalance [nm]	Below 10	Below 10
Cutting Feed Rate [mm/min]	120	25 (R = 0.05 mm)
		120 (R = 0.1, 0.3, 0.5 mm)
Cutting Depth [μm]	10 — 50	10 — 30

Table 7.2: The fabrication time (only machine running time) and the number of used end-mills of the 721 pixel lens array.

Part	Fabrication Time (per pixel) [min]	Fabrication Time (total) [hours]	No. of Used End-mills
Silicon Lens	5.8	70	11
Stycast AR Cap	9.0	108	17
Slits between Lens Pixels	8.5	102	8
Total	23.3	280	36

7.2.1 Lens Array Fabrication

The close-packed lens array with L/R = 0.34 and H/R = 0.525 in the 220-GHz band was designed in accordance with Chapter 5. Lens diameter of 1.2λ (= 1.64 mm) was chosen to couple the re-imaging optics with fast focal plane F-number (F_{focal} = 1) and pixel spacing 1.2$\cdot F_{focal} \cdot \lambda$. Absorption loss inside the lens was only 0.5% because the lens diameter was very small.

Figure 7.2: (**A**) Completed 721 pixel silicon lens array in 220-GHz band. (**B**) The silicon lens array before AR coating fabrication. The lens array was covered with a Stycast epoxy for AR layer. The white pillars protected the alignment holes. (**C**) The silicon lens array after AR coating fabrication. (**D**) The photograph of the dicing machine, DAD321, for cutting the edge of the lens array. The lens array was placed on the working table. (**E**) Completed 721 pixel silicon lens array with single-layer AR coating.

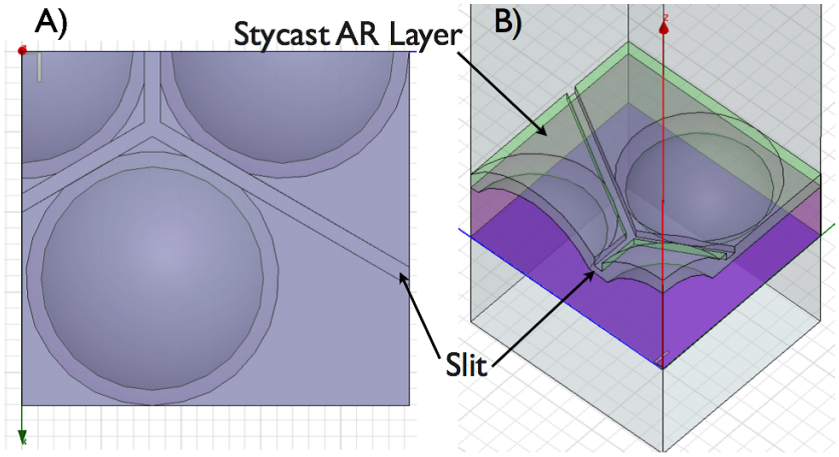

Figure 7.3: (**A**) The top view and (**B**) side view of the HFSS model for the beam pattern simulation. Slits between lens pixels relaxed the thermal stress between silicon (purple) and epoxy (green).

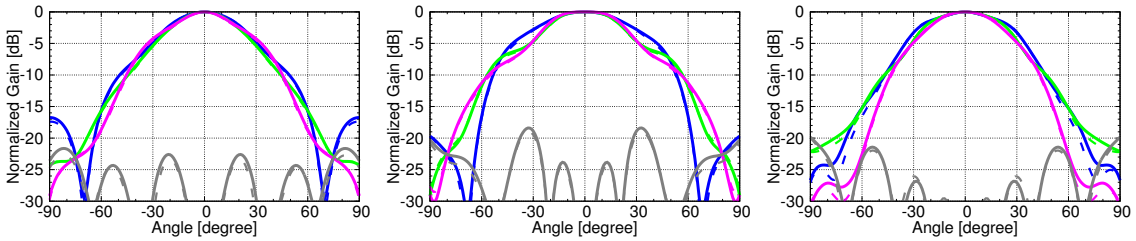

Figure 7.4: The effect of the slits on the beam patterns at (*Left*) 210 GHz, (*Middle*) 220 GHz and (*Right*) 230 GHz. The dashed and solid lines correspond to the beam patterns with slits and without slits, respectively. Blue, green and pink lines showed the E-, D- and H-planes, respectively.

Figure 7.2 shows the developed 721-pixel silicon lens array. The lens array was directly machined using a high-speed spindle on an ultraprecision machine. As described in Chapter 3, the fundamental fabrication method for 9, 102 and 721-pixel lens array is basically the same. We applied one layer of AR coating made from mixed epoxies, Stycast 1266 and 2850FTJ, onto the silicon lens array. It took approximately 100 hours to machine the 721-pixel silicon lens array with 11 end-mills. The details are 6 minutes for machining per lens and 2 hours for changing an end-mill. The time can be reduced by optimizing the machining condition. Processing conditions of the 721-pixel silicon lens array and its coating layer are summarized in Table 7.1. Also, Table 7.2 shows the fabrication time (only machine running time) and the number of used end-mills of the 721 pixel lens array.

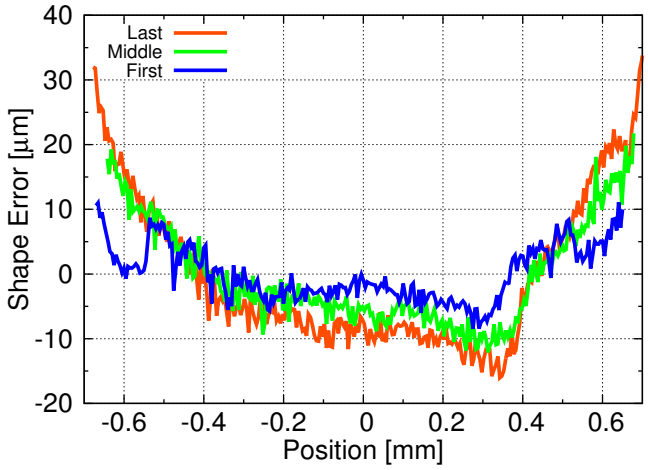

Figure 7.5: Measured shape fabrication errors of the 721pixel lens array. The vertical axis shows the shape error from the designed value and the horizontal axis shows the distance from the center of the lens. Blue, green and pink lines correspond to the first, middle and last fabricated lenses.

Table 7.3: Summary of the measured properties of the 721 pixel lens array.

	Measured Value
Best Shape Fabrication Error (P-V) [μ m]	15
Worst Shape Fabrication Error (P-V) [μ m]	45
Extension Thickness Error [μ m]	$\sim$ 14
Surface Roughness (r.m.s.) [μ m]	$\sim$ 1

The dimension of 721-pixel array is approximately 50 mm in diameter. Therefore, the AR-coated silicon lens array has slits between the lenses, which prevent the lens from breaking as silicon and epoxy have different thermal expansion coefficients. Figure 7.3 shows the model of the lens array with slits. The slit geometry has a 100 μm-width and 100 μm-depth. A slits were fabricated by using an end-mills with 50 μm radius. The effect of the slits on the far-field beam patterns at 210, 220 and 230 GHz are shown in Fig. 7.4. As shown in the calculated results, the effect of slits on the beam patterns is negligible because the slit size is very small.

Figure 7.5 shows the measured shape fabrication errors of the 721pixel lens array. The first, middle and last fabricated lenses were chosen to confirm the distribution of machining error. Measurements were done with a non-contact three-dimensional measuring machine. The machining error increases with progression of the fabrication. This

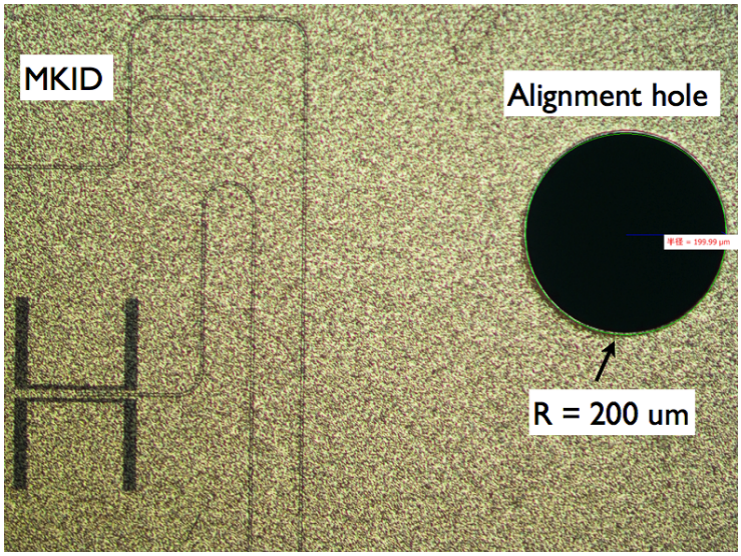

Figure 7.6: A photograph of an antenna-coupled MKID and an alignment hole. Alignment holes of the MKID substrate were fabricated by reactive ion etching (The holes were fabricated by M. Naruse from Saitama University). Its diameter was approximately 400 μm.

is because the end-mill was worn out. However, the shape fabrication error less than 50 μm was achieved. Simulations showed that these error values are within acceptable limits and do not affect the beam patterns much. Measured properties of the 721-pixel lens array are summarized in Tabel 7.3.

7.2.2 Alignment Between Lens and Substrate

The 721-pixel silicon lens array and the MKID substrate have 8 alignment holes at the edge of corners. Alignment holes of the 721-pixel lens array and the MKID substrate were fabricated by direct machining with small-diameter end-mill and reactive ion etching process, respectively. Figure 7.6 shows the alignment hole and antenna-coupled MKID of the device substrate. The diameter of alignment hole was approximately 400 μm and its edge shape was very sharp.

Figure 7.7 shows the alignment holes of lens array with device substrate. Small and large holes indicated with green circles correspond to the device substrate and lens array, respectively. The hole diameter of lens side was approximately 550 μm. The distance between position 1 and 2 (position 3 and 4) is approximately 5 mm. Also the distance between position 1 and 3 (position 2 and 4) is approximately 50 mm. Alignment accuracy

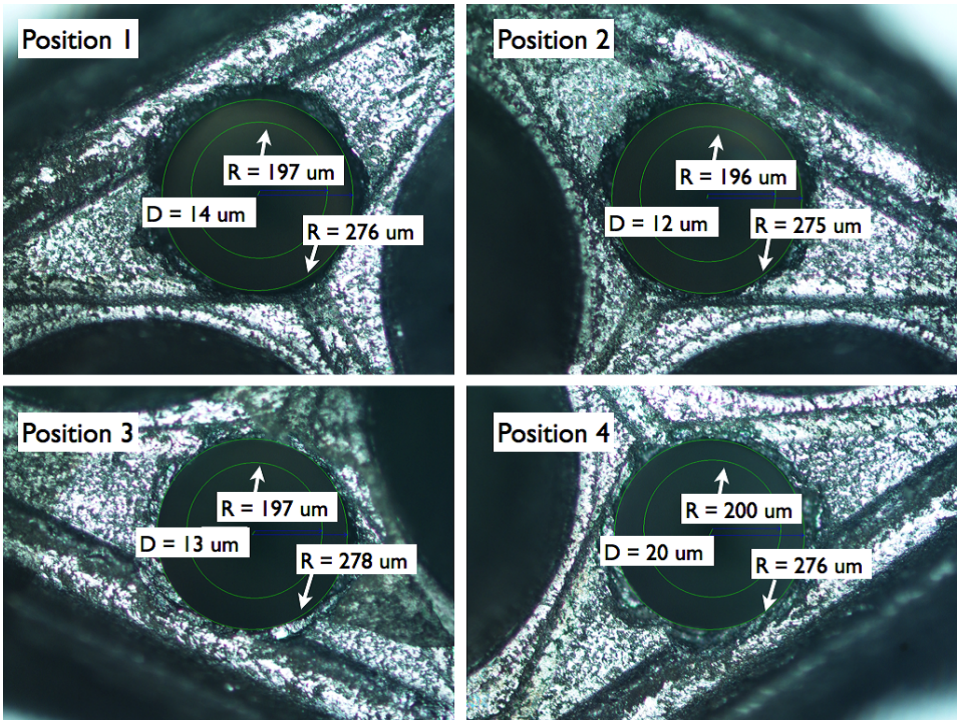

Figure 7.7: Photographs of alignment holes of lens array with the device substrate. Green circles correspond to alignment holes. Small holes correspond to device substrate and its diameter is approximately 400 μm. Big holes are lens side and its diameter is approximately 550 μm. The distance between position 1 and 2 (position 3 and 4) is approximately 5 mm. Also the distance between position 1 and 3 (position 2 and 4) is approximately 50 mm. Alignment accuracy of position 1, 2, 3 and 4 were 14, 12, 13 and 20 μm, respectively.

of position 1, 2, 3 and 4 were 14, 12, 13 and 20 μm, respectively. We confirm the alignment accuracy of less than 20 μm by using 4 holes. In this case, as discussed in Chapter 5, the misalignment effect on the beam pattern was negligible. It took about only 10 minutes to align this 4 holes.

7.3 Optical Measurement System

7.3.1 0.1K Dilution Refrigerator

To reduce excited quasi-particles and achieve high-sensitivity, 608-pixel MKID camera is required to be cooled to below a fifth of the critical temperature ($T \sim T_c/5$). In case of Al-based MKID array ($T_c \sim 1.2$ K), low-temperature of approximately 200 mK is needed. For this reason, a dilution refrigerator constructed by Taiyo Nippon Sanso Co. with 4 K

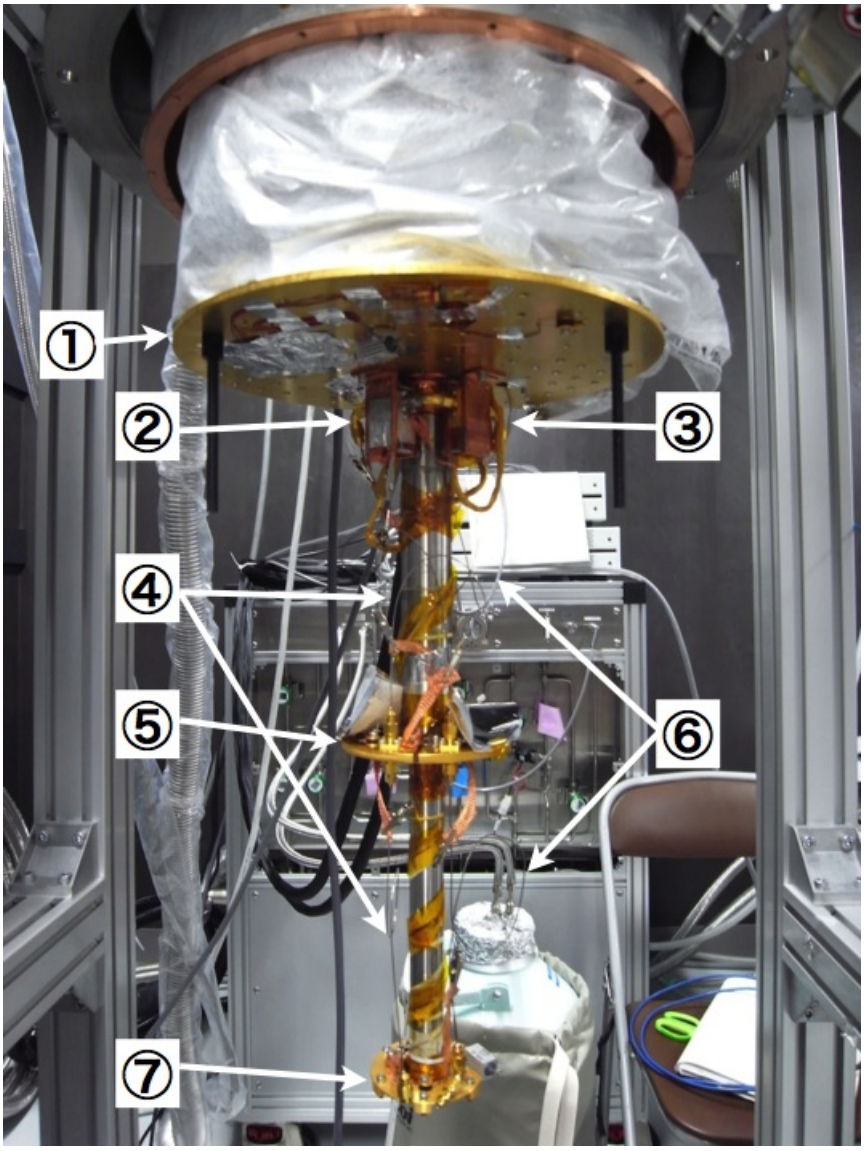

Figure 7.8: A photograph of the inside of the 0.1 K dilution refrigerator. 1: 4 K cold stage. 2: A cold isolator. 3: A cold low-noise amplifier (HEMT). 4: 0.86 mm diameter CuNi cables for transmission of the input signals. 5: 1 K cold stage. 6: 0.86 mm diameter NbTi superconducting cables for transmission of the output signals. 7: 0.1 K cold stage.

pulse tube (PT) refrigerator (Sumitomo Heavy Industries, Ltd/SRP-082B2S-F-70LP) has been used. The dilution refrigerator is composed of four cold stages; first stage (40 K) of the PT refrigerator, second stage (4 K) of the PT refrigerator, 1 K stage and 100 mK stage with mixing chamber. The cooling power of 40 K, 4 K, 1 K and 100 mK stages are 35 W, 0.9 W, approximately 2 mW and 20 μW, respectively.

Figure 7.8 shows a photograph of the inside of the dilution refrigerator. 4 K, 1 K and 100 mK stages and each component such as low-noise amplifier and coaxial cables are shown. As discussed in Chapter 4, the CuNi coaxial cables were chosen to reduce the thermal load on the cold stages because its low thermal conductivity (Barends, 2009). The microwave signals between room temperature, 40 K and 4 K stages are carried by CuNi coaxial cables with the diameter of 2.19 mm. Also, the input microwave signals between 608 pixel MKID array, 1 K and 4 K stages are carried by CuNi coaxial cables with the diameter of 0.86 mm. However, attenuation of 300 mm-length CuNi coaxial cable with the diameter of 0.86 mm is approximately 5 dB (17.1 dB/m at 5 GHz). To improve the attenuation loss of output signal caused by thin CuNi coaxial cable, 0.86 mm-diameter superconducting coaxial cables made from niobium titanium (NbTi) were used to connect between 608 pixel MKID array and cold low-noise amplifier which is located at 4 K cold stage. These superconducting cables have the advantages of low electrical resistivity and low thermal conductivity. The gain of cold low-noise amplifier is more than 30 dB, and the noise temperature is less than 5 K at the frequency from 3 to 9 GHz.

To reduce the effect of external magnetic field from the PT refrigerator and terrestrial magnetism, five magnetic shields were used. First shield is made of the permalloy, which is an alloy of nickel and iron, and located outside of the 300 K radiation shield. Second shield at 4 K and third shield at 1 K are made of A4K which is a product of amuneal. The 4 K shield is located outside of the 4 K radiation shield and cold nested baffle, and 1 K shield is located outside of the gas piping of ^{4}He and ^{3}He. Fourth shield is Sn-plated 4 K radiation shield (Sn directly over copper), and which acts as a superconducting shield at temperature below 3.7 K. Similarly, fifth shield made of Sn-plated copper is located on opposite side of 608 pixel MKID array at 100 mK.

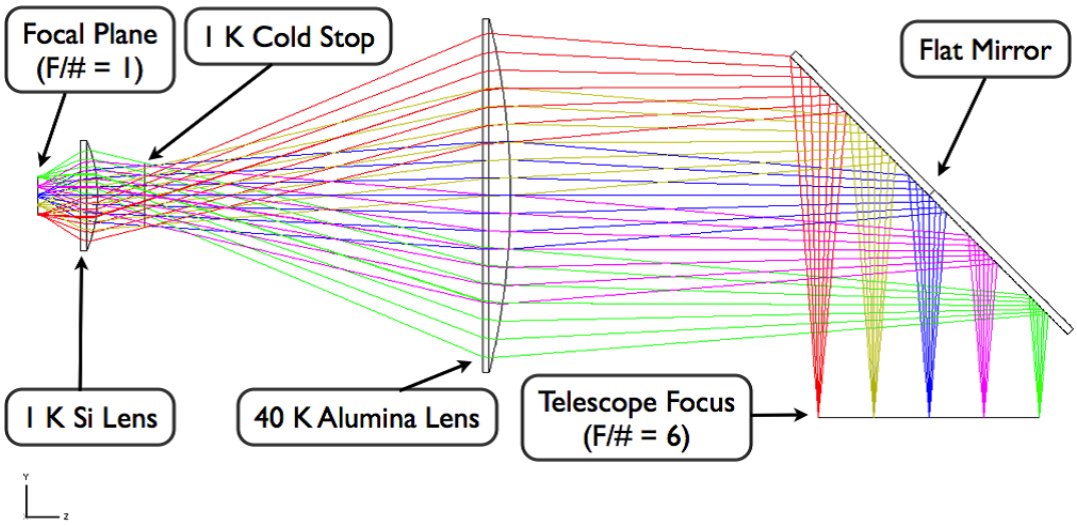

Figure 7.9: A cross-sectional view of a re-imaging optics. The silicon and alumina cold re-imaging lenses were shown with ray-tracing image calculated by ZEMAX. The two cold lenses re-image the F/# = 6 telescope focus to the F/# = 1 telecentric focal plane. The diameter of telescope focus and focal plane are 100 mm and approximately 18 mm, respectively. If the optical system is installed on a 10-m telescope, it provides a field-of-view of approximately 6.6 arcmin.

7.3.2 Re-imaging Optics for Beam Measurement

To couple the signal from telescope focus to focal plane efficiently, we should consider whether to use a reflective, refractive or combinational optical system. A large-format camera with more than 1000 pixels is composed of superconducting films and flat dielectric wafers. Therefore, flat focal plane and telecentricity, which means that the all incident chief rays is perpendicular to focal plane, are needed to efficiently couple the signal to the detector.

An all-refractive optics system using 608 pixel MKID camera for wide field-of-view observations has been developed. The all-refractive optics with two dielectric lenses transfers from a telescope focus of F/# = 6 at ambient temperature to a focal plane of F/# = 1 at 100 mK. The all-refractive optics has the following advantages:

1. The configuration is overwhelmingly compact compared to reflective optics system.

2. It typically provides a large diffraction limited field-of-view with high optical throughput.

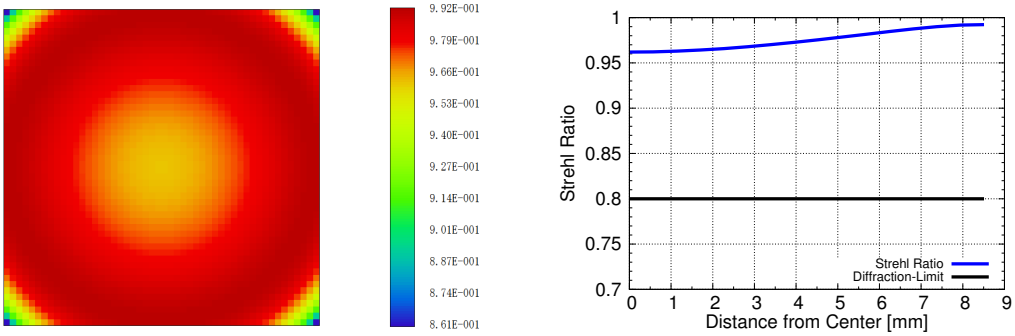

Figure 7.10: (*Left*) The Strehl ratio of 220 GHz over the focal plane. (*Right*) The Strehl ratio of 220 GHz in x and y directions of the focal plane. Black line showed the diffraction limit.

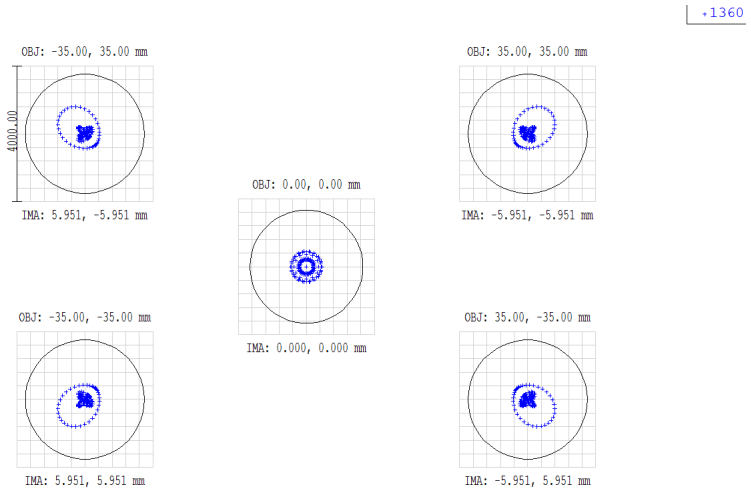

Figure 7.11: Spot diagrams of 220 GHz over the focal plane. Four corners of the figure correspond to the edge of the field of view. The ray spots (blue points) are small compared to the Airy disks (black circles).

3. The mechanical design is simple.

The small F-number of telescope focus (F/# $\leq$ 6) leads to the compact configuration and fast scanning. Also, fast focal plane (F/# $\sim$ 1) can keep the cryostat compact and facilitate cooling to a temperature below 300 mK. A cross-sectional view of designed all-refractive re-imaging optics between F/# = 6 telescope focus and F/# = 1 focal plane with ray-tracing image calculated by ZEMAX is shown in Fig. 7.9. The difference in color corresponds to the difference in position. The large and small dielectric lenses are made from high-purity alumina and silicon, respectively, and these lenses are mounted on 40 K and 1 K stages. The diameter of telescope focus, 40 K alumina lens, 1 K silicon

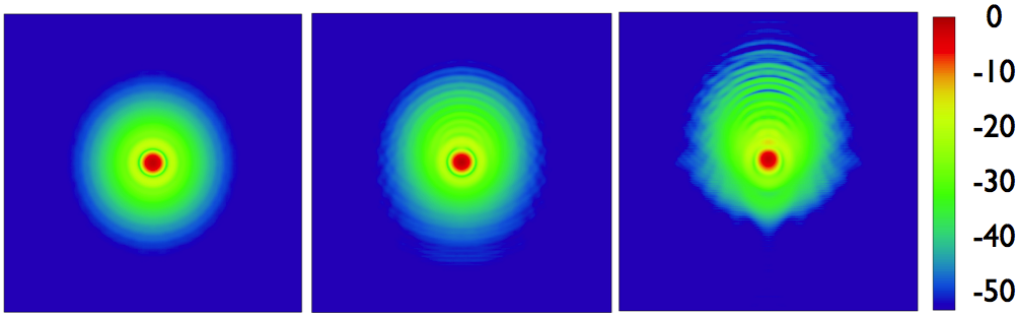

Figure 7.12: Calculated beam patterns at the F/# = 6 telescope focus. Beam patterns were calculated based on the physical optics propagation. From left to right figures correspond to (X mm, Y mm) position of (0, 0), (0, 4) and (0, 8.5) (= edge of the focal plane), respectively. The scale of each figure is 166 mm.

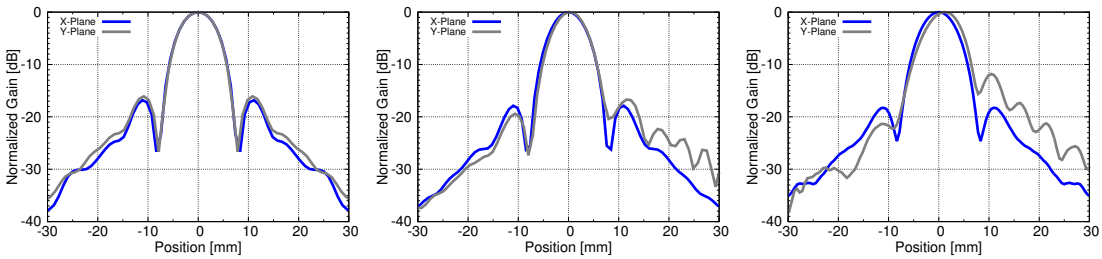

Figure 7.13: Cross-sectional view of the figure 7.12. Blue and gray lines correspond to the X-plane (horizontal axis of the 2D maps) and the Y-plane (vertical axis of the 2D maps), respectively.

lens and focal plane are 100 mm, 170 mm, 50 mm and approximately 18 mm, respectively. The role of the 1 K silicon lens is to correct aberrations and to obtain fast focal plane (F/# = 1), flat focal plane and telecentricity. To realize the telecentric focal plane, the radius of curvature (R) of the 1 K silicon lens needs to satisfy the following equation:

$$R = l(n-1), \tag{7.1}$$

where n is the refractive index of silicon, and l is the distance between the cold stop and the silicon lens surface.

Strehl ratio and spot diagram were calculated to evaluate the imaging quality of the re-imaging optics. Higher Strehl ratio provides smaller beam asymmetry. Therefore, Strehl ratio higher than 0.8 (the Strehl ratio of 0.8 correspond to the diffraction limit) is required. The calculated Strehl ratio of 220 GHz over the focal plane is shown in the

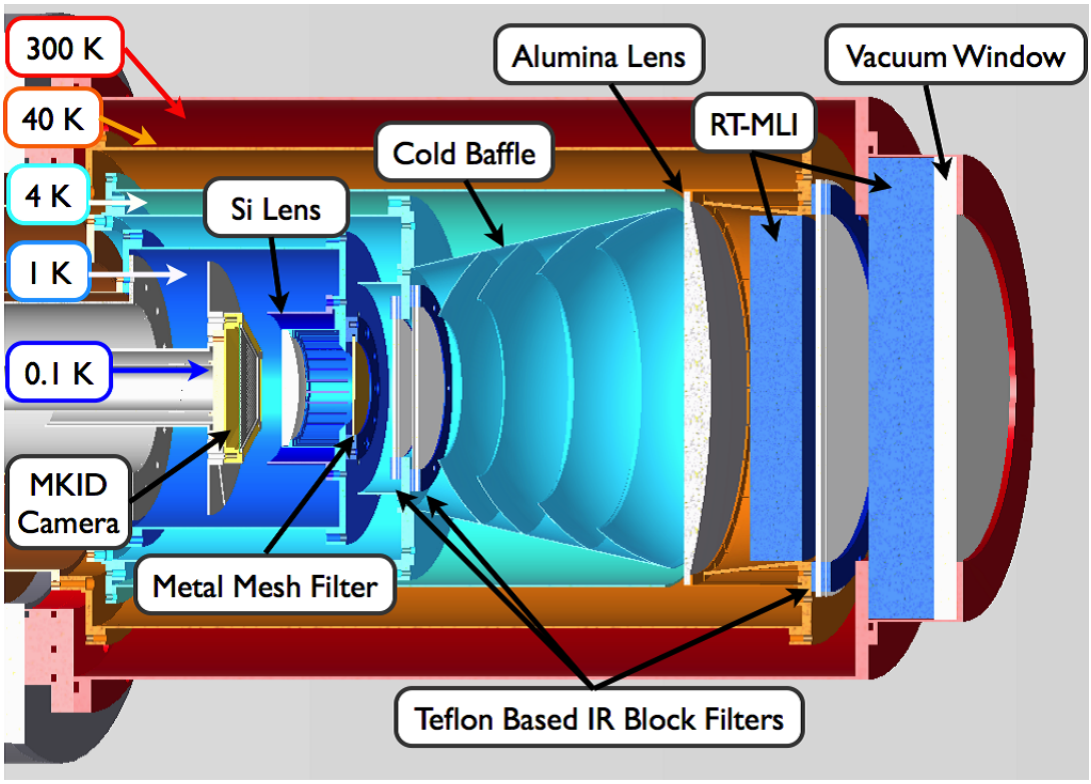

Figure 7.14: Mechanical design of optical measurement system with the 0.1 K dilution refrigerator.

left panel of Fig. 7.10. The right panel of Fig. 7.10 shows its cross section in x and y directions. Strehl ratio higher than 0.96 over the edge of field-of-view has been achieved. Figure 7.11 shows a spot diagrams of 220 GHz over the focal plane. Four corners of the figure correspond to the edge of the field-of-view. The results showed that the ray spots (blue points) are small compared to the Airy disks (black circles). The diameter of the Airy disk at 220 GHz is approximately 3400 μm.

Figure 7.12 shows calculated two-dimensional beam patterns at the F/# = 6 telescope focus. Beam patterns were calculated based on the physical optics (PO) propagation. A software ZEMAX was used to analyze the geometric optics and PO. The half-power beam width (HPBW) of input gaussian beam at the F/# = 1 focus is 48 degree which corresponds to HPBW of the 210 GHz beam pattern calculated by HFSS (see Fig. 7.4). The side-lobe level, which corresponds to a green area in the figure, increases with the increasing distance from the center position. This is because the edge-taper level increases with distance from the center position. Cross-sectional patterns of Fig. 7.12 are shown

Table 7.4: Material properties of ZITEX coated IR blocking filters.

	Pore Size [μm]	Filling Rate [%]	Refractive Index	Thickness [μm]	Melting Temperature [K]
Teflon	-	-	1.44	1500	330
ZITEX G-108	3.5	45	1.24	200	330
ZITEX G-110	1.5	40	1.26	250	330
ZITEX G-115	1.5	40	1.26	380	330
LDPE	-	-	1.51	30	120

Table 7.5: Frequency at zero reflection of various types ZITEX coated IR blocking filters.

Coated Material	Frequency at Zero Reflection [GHz]
ZITEX G-108	302
ZITEX G-110	238
ZITEX G-115	157

in Fig. 7.13. The beam patterns with circular symmetry and maximum sidelobe level of approximately $-$ 15dB were achieved over the whole focal plane.

The mechanical design of all-refractive re-imaging optics with the 0.1 K dilution refrigerator is shown in Fig. 7.14. The re-imaging optics consists of a vacuum window, IR blocking filters, a nested baffle, two dielectric lenses made from high-purity alumina and silicon, magnetic shields and 608 pixel MKID camera. The diameter of the vacuum window is 150 mm. The distance between the vacuum window and 608 pixel MKID camera is approximately 330 mm. The alumina lens at 40 K and the silicon lens at 1 K were mounted with a stress-free lens holder since thermal expansion coefficient of lens and holder is different. Other components such as IR blocking filters and a nested baffle are discussed later.

7.3.3 Filter Chain

ZITEX coated Low-pass Filters

It is required to use a high-performance low-pass filters because the vacuum-window of our optical measurement system has a large diameter of 150 mm and the cooling power of the 0.1 K stage is only 20 μW. In our optical measurement system, a power of 8.12 W

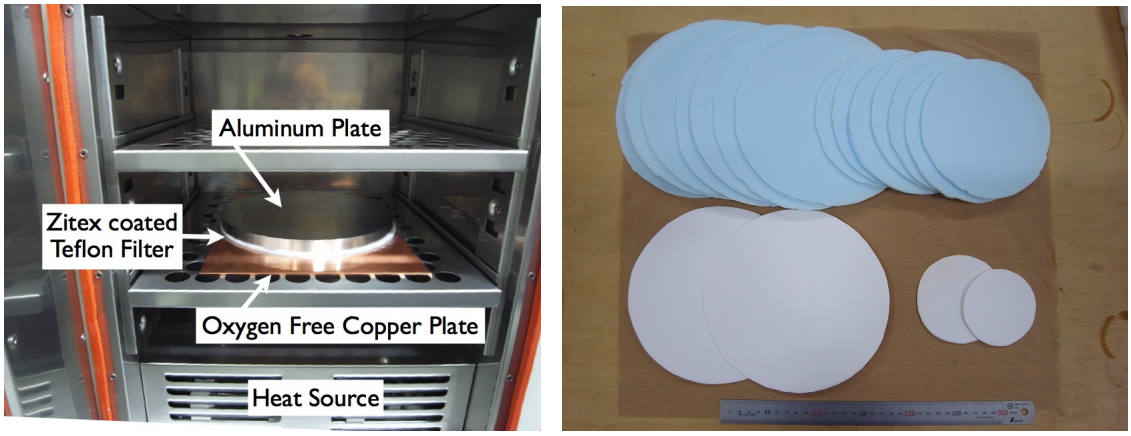

Figure 7.15: (*Left*) Inside the oven for the fabrication of the ZITEX coated IR blocking filters. The filters, which have ZITEX/LDPE/Teflon/LDPE/ZITEX structure, were pressed by an aluminum plate, and heated above the melting temperature of LDPE. (*Right*) A photograph of the filters. Blue and white filters correspond to the radio-transparent multi-layer insulations (RT-MLI) and ZITEX coated Teflon filters, respectively.

from a blackbody spectrum at 300 K is incident on the vacuum window. Metal mesh filters have high transmittance at millimeter-wave range and excellent filter cut-off (Ade et al., 2006). However, the larger filter is more expensive. Therefore it is quite important to develop an inexpensive but large-diameter, high-performance filters.

By reference to Yoon et al. (2006), IR blocking filters based on ZITEX coating and Teflon (PTFE) plate were developed. ZITEX coating and Teflon plate act as scattering type and absorptive type filters, respectively. The ZITEX film, which is a product of Saint-Gobain, is porous PTFE thin sheet. The pore size and the thickness of ZITEX G-series are typically 3 μm and 200 μm, respectively. A small pore size leads to a scattering at terahertz range. Therefore, ZITEX films have sharp cutoff at approximately 6 THz (see Appendix A). IR-blocking filter requires high transmittance and low-absorption loss in millimeter-wave bands. It also requires low-refractive index to reduce the surface reflection and effective cutoff property at IR region. In millimeter-wave bands, Teflon has low-dielectric loss tangent of less than 10^{-4}, and low-refractive index of 1.44, at 4 K (Lamb, 1996). However, the refractive index of 1.44 leads to a reflection at each Teflon-vacuum interface of approximately 3% per surface. The ZITEX filters with refractive index of approximately 1.24 were used as an AR coating layer for Teflon plate to reduce surface reflections (Yoon et al., 2006). The ZITEX filters have millimeter-wave band transmittance

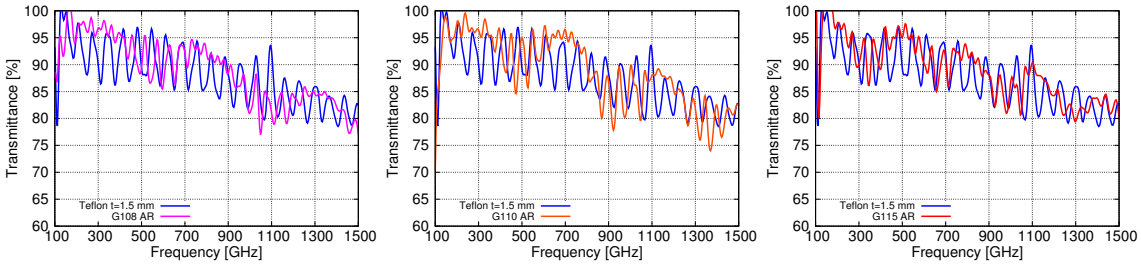

Figure 7.16: The measured transmittance of the ZITEX coated IR blocking filters. Blue line showed the uncoated teflon, and other color lines showed the coated teflon. The coated materials were (*Left*) ZITEX G-108, (*Middle*) ZITEX G-110 and (*Right*) ZITEX G-115, respectively. The frequency at zero reflection slightly shifted because the ZITEX has different thickness.

of more than 96% and excellent cutoff at IR region, and these properties are summarized in Appendix A.

To bond the Teflon plate and ZITEX coating layers, a thin low-density polyethylene (LDPE) sheets were used (Yoon et al., 2006). The material properties for ZITEX coated Teflon filter are summarized in Table 7.4. According to Yoon et al. (2006), LDPE thin film is very suitable material for bonding ZITEX sheet with Teflon plate because its melting temperature is lower than that of Teflon and ZITEX. As shown in Fig 7.15, the filters which have ZITEX/LDPE/Teflon/LDPE/ZITEX structure were pressed by an aluminum plate, and heated above the melting temperature of LDPE.

The three types of filters using various ZITEX coating layers have been developed. The measured transmittance of these filters are shown in Fig. 7.16. The left, middle and right panel correspond to the ZITEX G-108, G-110, and G-115 type filters. The calculated and measured frequencies at zero reflection are in good agreement, as shown in Table 7.5. The G-110 type ZITEX coated Teflon filter was chosen to use for optical system because it has a minimum reflection loss at 200 $-$ 250 GHz.

Vacuum Window

A vacuum window consists of 10-mm-thick high-density polyethylene (HDPE) and ZITEX G-110 AR coating layers. The refractive index of HDPE is 1.54 (Lamb, 1996), and that leads to a reflection at each HDPE-vacuum interface of approximately 4% per surface. Therefore, an AR coating is needed to improve the total reflection loss of approximately

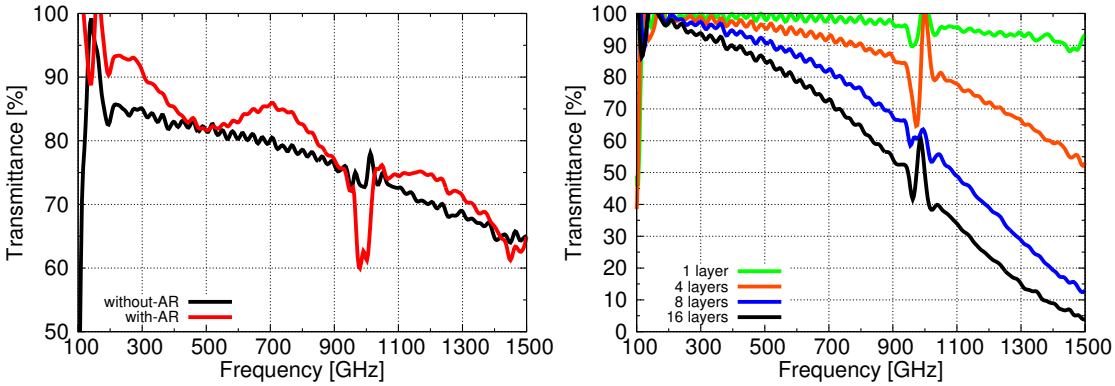

Figure 7.17: (*Left*) The comparison of the measured transmittance of an AR coated (red line) and an uncoated HDPE vacuum window (black line). (*Right*) The measured transmittance of the radio-transparent multi-layer insulations at ambient temperature. Green, orange, blue and black lines correspond to the 1, 4, 8 and 16 layers, respectively. The spikes around 1 THz of both figures were due to the effect of water vapor in the air.

8%. The fabrication process of AR coated window is the same as the ZITEX coated Teflon filter. The left panel of Fig. 7.17 shows the comparison of the measured transmittance of an AR coated (red line) and an uncoated HDPE vacuum window (black line). The thickness of AR coating layers was optimized at 220 GHz. The 220-GHz transmittance of coated window is approximately 8% higher than that of uncoated window.

Radio-transparent Multi-layer Insulation

Recently, radio-transparent multi-layer insulation (RT-MLI) using Styroace-II Styrofoam (the Dow Chemical Company) has been developed (Choi et al., 2013). Multi-layer insulation is multiply-stacked thermal insulation sheet. Generically, thin thermal insulating sheet consists of polyimide, polyester, and fluorinated ethylene propylene (FEP) films specially coated with vapor-deposited aluminum. These evaporated metal films are not transparent to millimeter-/submillimeter-wave range. On the one hand, RT-MLI is composed of stacked Styroace-II Styrofoam which is millimeter-wave transparent thermal insulator. An AR coating is unnecessary on the Styroace-II Styrofoam surface because its refractive index is nearly 1.

According to Choi et al. (2013), the radiation energy from high-temperature stage

(T_{high}) to low-temperature stage (T_{low}) per unit area is described as follows:

$$q = \sigma[(T_{high})^4 - (T_{low})^4], \tag{7.2}$$

where q and σ correspond to the radiation energy and the Stefan-Boltzmann constant, respectively. When RT-MLI is located between high-temperature stage and low-temperature stage, the radiation energy from T_{high} to T_{low} is described as follows:

$$q = \frac{1}{N+1}\sigma[(T_{high})^4 - (T_{low})^4], \tag{7.3}$$

where N is the number of layers. As can be seen from Eq. 7.2 and Eq. 7.3, the relation between the radiation energy (q) and the number of layers (N) is given by,

$$q \propto \frac{1}{N+1}. \tag{7.4}$$

The right panel of Fig. 7.17 shows the measured transmittance of RT-MLI. The comparison of 1, 4, 8 and 16 layers is shown. Each layer has a thickness of approximately 2 mm. The high transmittance of the RT-MLI at millimeter-/submillimeter-wave range has been confirmed. Also, RT-MLI acts as a low-pass filter because of its porous structure. In our optical system, 8 layers RT-MLI located inside a 40 K baffle and 8 layers RT-MLI located behind vacuum window were used to reduce the incident thermal loads. A photograph of RT-MLI (blue filters) and ZITEX coated Teflon filters (white filters) is shown in the right panel of Fig. 7.15.

Metal-mesh Low-pass Filter

A 300-GHz metal mesh filter, which was provided by QMC Instruments Ltd., was used as a 1 K low-pass filter. This filter was located at a cold stop of a re-imaging optics. According to Ade et al. (2006), the inductive, capacitive and complex grid geometries act as a high-pass filter, low-pass filter and band-pass filter, respectively. These grid patterns over large areas are fabricated by using ultra-violet photolithographic techniques. Furthermore, a multi-layer structure produces flat in-band transmittance and sharp cutoff property (Tucker & Ade, 2006).

The left panel of Fig. 7.18 shows the measured transmittance of 300-GHz metal mesh

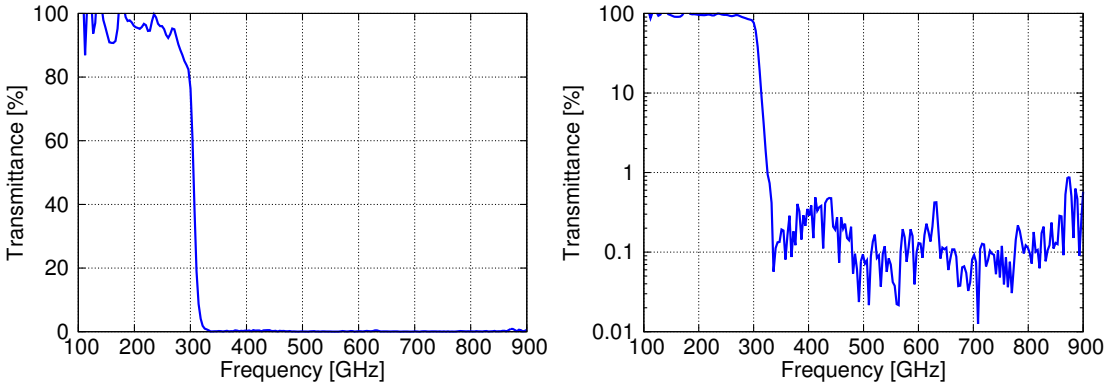

Figure 7.18: (*Left*) The measured transmittance of metal-mesh low-pass filter. (*Right*) The same data as left figure but the vertical axis is logarithmic scale.

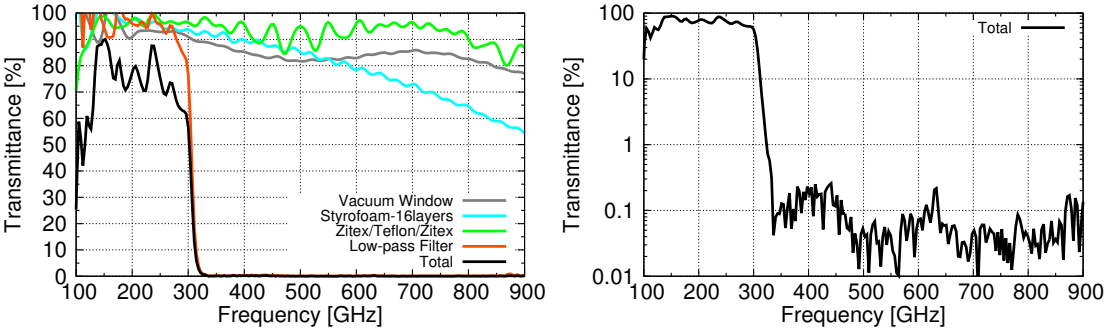

Figure 7.19: (*Left*) The measured transmission of the individual IR blocking filters and vacuum window. A composite transmittance of all filters is also plotted (black line). (*Right*) The transmission of all filters but the vertical axis is logarithmic scale.

filter. The millimeter-wave band ($<$ 300 GHz) transmittance is above 90%. The right panel of Fig. 7.18 shows the same data with logarithmic scale. A high cutoff rate, which corresponds to below 1% transmittance, at a frequency of above 300 GHz was achieved.

Total Transmittance of Filter Chain

A total filter chain consists of vacuum window, 16 layers of RT-MLI, 4 layers of ZITEX coated Teflon filter and single metal-mesh low-pass filter. The measured transmittance of the individual IR blocking filters and vacuum window are shown in the left panel of Fig 7.19. A composite transmittance of all filters is also plotted (black line). The right panel of Fig 7.19 shows the transmittance of all filters with logarithmic scale. The high transmittance of approximately 80% at millimeter-wave band, and high-rejection rate at

Figure 7.20: Photograph of the cold baffles. Left, center and right baffles correspond to the large 4 K nested baffle with reflective plates, small 4 K baffle and 1 K baffle, respectively. The 4 K baffles are made of aluminum. The 1 K baffle is made of oxygen free copper. The black parts of the inside of the baffles showed the absorber with a carbon black.

Table 7.6: The recipe of carbon based black coating (Persky, 1999).

	Rate [%]
Stycast 2850FTJ	64.67
Catalyst 23LVJ	4.85
Carbon Black	6.67
Glass Beads	
(ϕ = 60, 400, 600 and 800 [μm])	19.05
Silicon Carbide	4.76

out-band have been achieved.

7.3.4 Baffles

A cold baffles located at 1 K and 4 K have been installed to reduce stray light from vacuum window. A photograph of the cold baffles is shown in Fig. 7.20. The 1 K small-baffle (right) and 4 K small-baffle (middle) are made of oxygen free copper and aluminum, respectively. The carbon based black coating was applied to the inside of the cold baffles (Persky, 1999). The recipe of carbon based black coating is shown in Table 7.6. The role of a carbon black and Stycast 2850FTJ is to absorb a stray light. Also, various glass beads

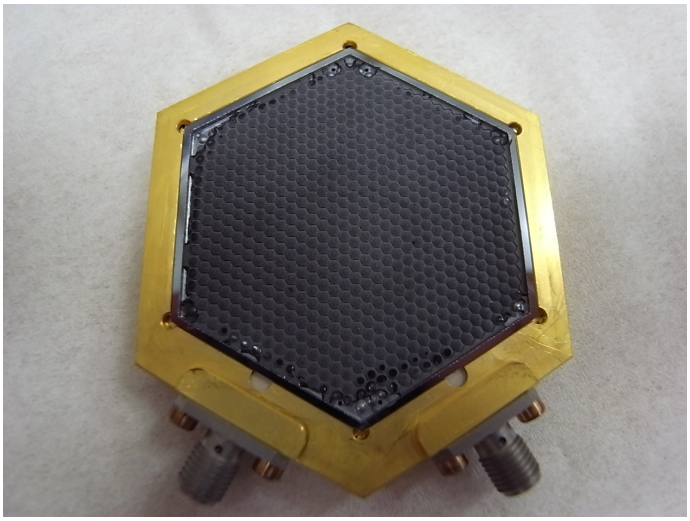

Figure 7.21: A photograph of 608-pixel MKID camera with AR-coated silicon lens array.

and approximately 1 mm-size silicon-carbide-grains act as scattering substance for the frequency range from millimeter-wave to terahertz.

A large nested baffle (left of Fig. 7.20) mounted on 4 K consists of conical baffle and four reflective plates (Sekiguchi, 2014). The shape of reflective plates is spherical surface, and its curvature radius is 80 mm. The length and diameter of the nested baffle are approximately 120 mm and 155 mm, respectively. The carbon based black coating was applied to the back side of the reflective plates. Therefore, the front side and back side of reflective plates act as reflector and absorber, respectively.

7.4 Evaluations of MKID Array

A photograph of 608-pixel MKID camera with AR-coated silicon lens array is shown in Fig. 7.21. The whole size of a module is approximately 60 mm. The center black part correspond to the AR-coated silicon lens array. The cooling time from 300 K to 100 mK of optical measurement setup is approximately 60 hours as shown in Fig. 7.22. The system includes a 608-pixel MKID camera, cryogenic wiring, coaxial cabling, baffles, two dielectric lenses and IR blocking filters. As shown in the black line in Fig. 7.22, 608-pixel MKID camera has been cooled to 100 mK when the camera observed the 300 K blackbody load. The dilution refrigerator constructed by Taiyo Nippon Sanso Co., which was used this optical measurements, was well-cooled, easy handling and compact system.

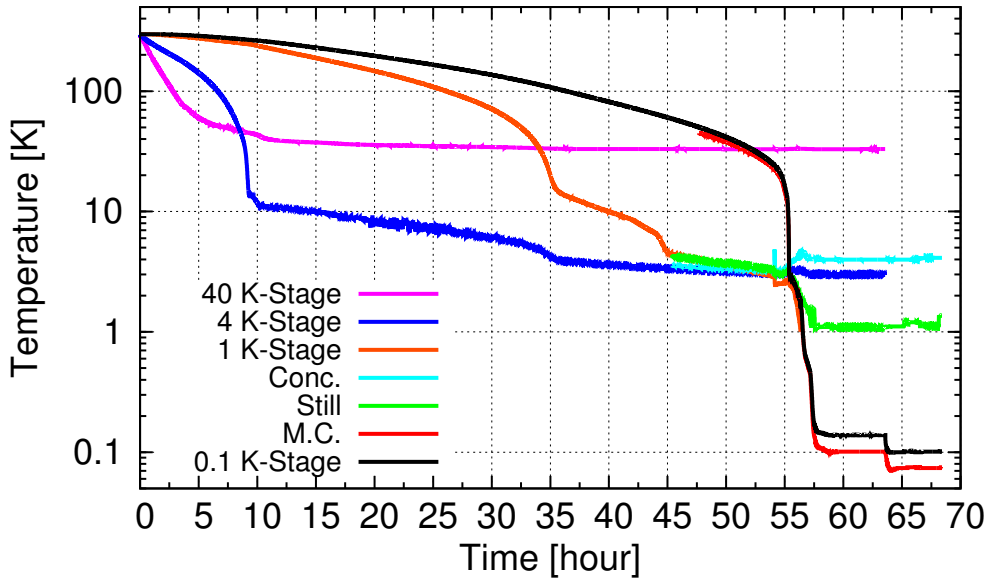

Figure 7.22: The cooling time from 300 K to 100 mK of optical measurement condition. The system includes a sample box, cabling, baffles and IR blocking filters. A thermometer for mixing chamber (M.C.) is just outside the cold head, and that for a 100 mK stage is attached near the frame of 608-pixel MKID camera. A ruthenium oxide temperature sensor (RX-202A) driven by LakeShore 350 temperature monitor and a silicon diode sensor (DT-670) driven by LakeShore 218 were used to monitor the temperature of 100 mK stage. The roles of the RX-202A and the DT-670 are to monitor the low temperature (< 40 K) and high temperature (> 1.4 K), respectively.

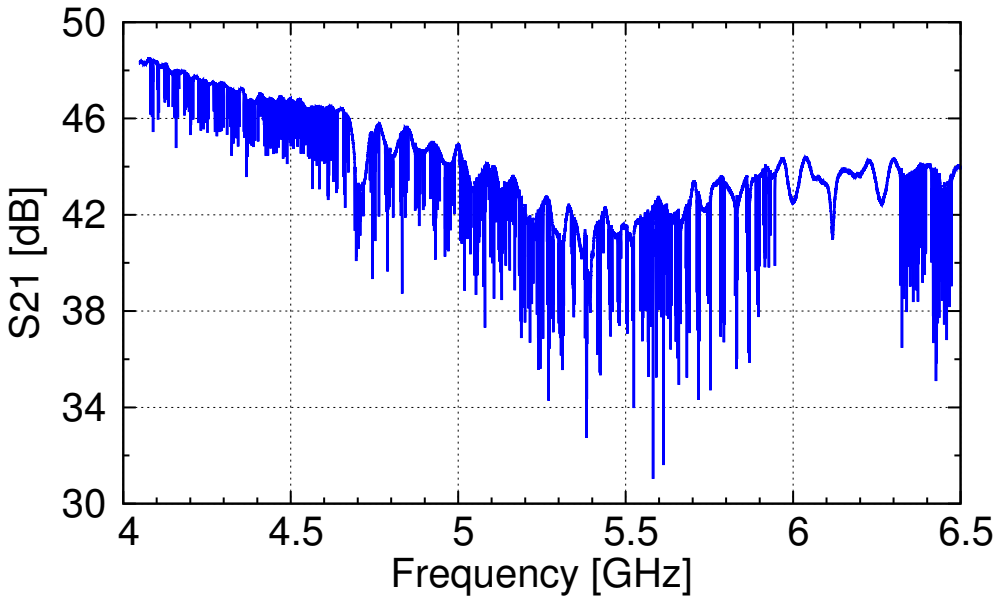

Figure 7.23: The S_{21} spectrum of 608-pixel MKID array at 100 mK. The number of measured pixels were 584 (yield of $\sim 95\%$), and resonance frequencies falls into a 2.5 GHz band centered at 5.2 GHz.

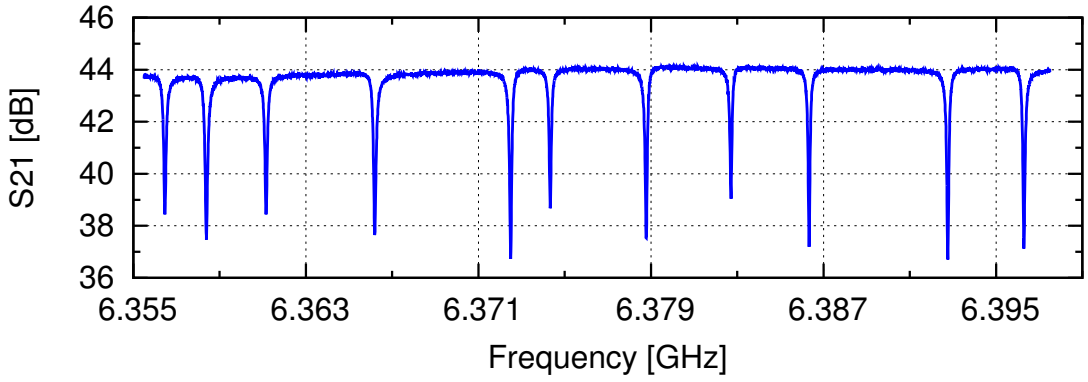

Figure 7.24: Extended figure of Fig. 7.23 around 6.37 GHz. 11 resonators were displayed.

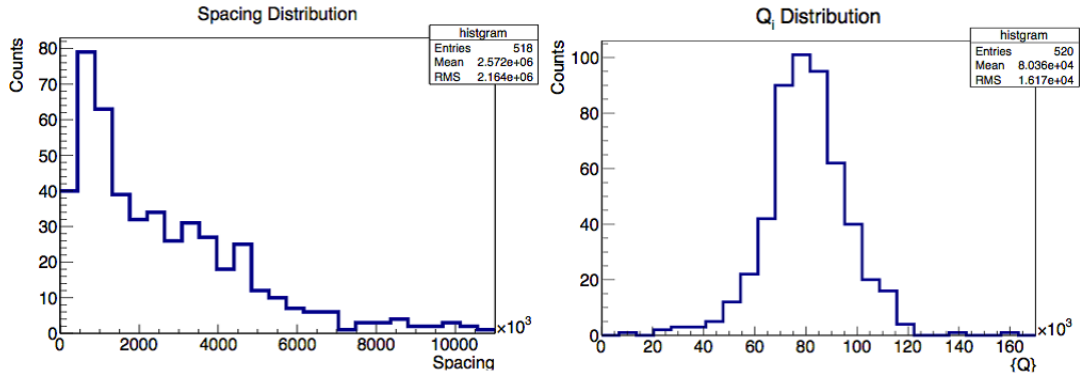

Figure 7.25: (*Left*) Frequency spacing distribution of 608-pixel MKID array. Average frequency spacing was approximately 2 MHz. (*Right*) Quality factor (Q_i) distribution of 608-pixel MKID array. The average quality factor was approximately 10^5.

Figure 7.23 shows the S_{21} spectrum of 608-pixel MKID array at 100 mK. Also, the detail of MKID resonances around 6.37 GHz is shown in Fig. 7.24. The resonance frequencies falls into a 2.5 GHz band centered at 5.2 GHz. High yield of around 95% has been achieved for the 608 pixel MKID camera. The left panel of Fig. 7.25 shows the frequency spacing distribution of 608-pixel MKID array. Average frequency spacing was approximately 2 MHz. Internal quality factor (Q_i) distribution of 608-pixel MKID array is shown in the right panel of Fig. 7.25. The average quality factor was approximately 10^5.

To confirm overall response of the re-imaging optics with 608-pixel MKID camera, optical responses of MKID array were measured by using hot (300 K blackbody absorber with ECOSORB) and cold loads (77 K blackbody absorber sunk in liquid nitrogen). Figure

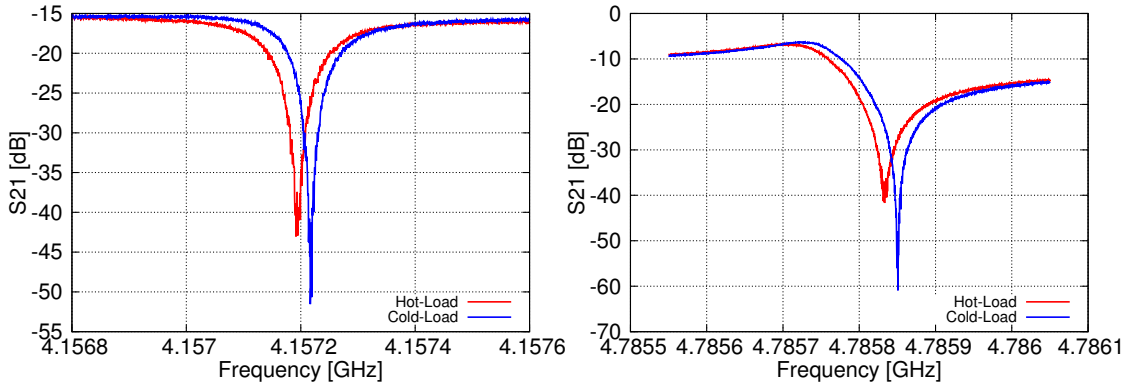

Figure 7.26: Hot (300 K blackbody absorber with ECOSORB) and cold (77 K blackbody absorber sunk in liquid nitrogen) load responses of the two resonators at 100 mK.

7.26 shows the hot and cold load responses of the two resonators at 100 mK. Hot and cold loads were located in front of the vacuum window of the cryostat. As shown in Fig. 7.26, blackbody radiation of 77 K and 300 K were distinguished by MKIDs array. We confirmed that the optical measurement system with the 100 mK dilution refrigerator was well-behaved.

8

Design of the 20000 Pixels Terahertz-Camera for the Antarctic 10-m Terahertz Telescope

8.1 Introduction

It is important to combine the wide field-of-view (FoV) telescope with large-format camera to reveal large scale structures of distant sub-millimeter galaxies. The Antarctic terahertz telescope will be constructed at Dome Fuji, a Japanese Antarctic station. The observing frequency of this telescope is 400-, 850- and 1500-GHz bands. In this chapter, we present a design of a wide field-of-view re-imaging optics and a 20000 pixels terahertz camera for the Antarctic terahertz telescope.

8.2 Design of the Antarctic 10-m Terahertz Telescope

To obtain wide FoV, the Antarctic terahertz telescope was designed based on Ritchey-Chretien optics (Imada et al., in prep). The Antarctic terahertz telescope consists of 10-m single dish telescope to obtain small angular resolution. The Antarctic terahertz telescope has two Nasmyth foci, and the one is used for a large-format terahertz camera. A well-designed mirror configuration produces 1-degree FoV at the F/# = 6 Nasmyth focus.

8.2.1 Fast and Wide-FoV Re-imaging Optics

The main observing frequency of the Antarctic terahertz telescope is 850 GHz band. By using the developed elemental technologies discussed in previous chapters, a 850-GHz band re-imaging optics which connects a Nasmyth focus of F/# = 6 with a focal plane has been designed. The small F-number of telescope focus (F/# $\leq$ 6) leads to the compact configuration and fast scanning. Also, fast focal plane (F/# = 1) can keep the cryostat compact and facilitate cooling to a temperature below 100 mK.

Figure 8.1 shows the ray-tracing image of the 10-m Antarctic terahertz telescope with re-imaging optics calculated by ZEMAX (Imada et al., in prep, Tsuzuki et al. 2014). The diameter of a sub-reflector and a free-form third-mirror are 1500 mm and 1571 mm, respectively. This telescope design provides 1-degree FoV. Extended figure of 1 degree FoV re-imaging optics after reflecting by a M1 mirror (third free-form mirror) is shown in Fig. 8.2 (Tsuzuki et al., 2014). The 1 degree FoV re-imaging optics consists of four free-form (X-Y polynomial) reflective mirrors at ambient temperature and 530-mm-diameter aspheric alumina lens at cryogenic temperature. The size of telescope focus, vacuum window and

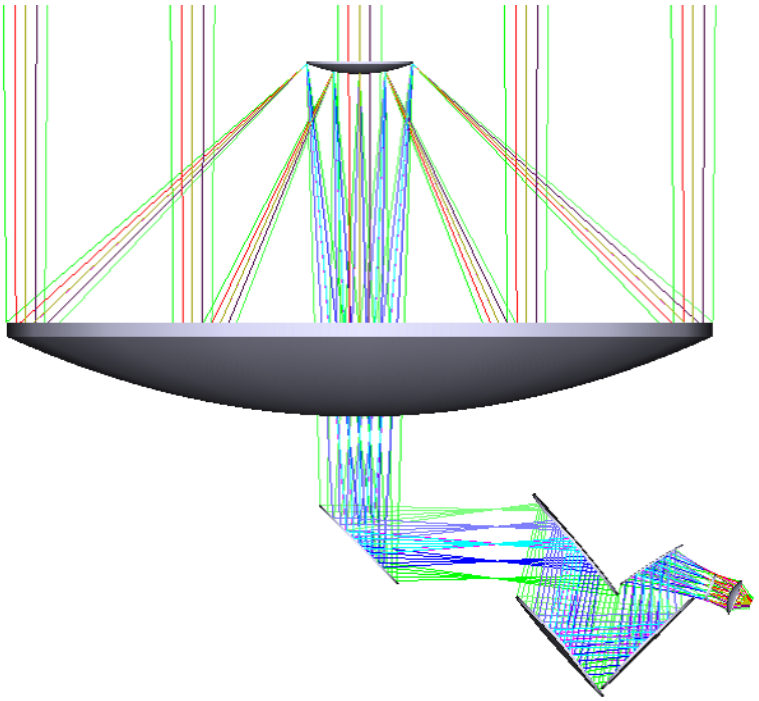

Figure 8.1: The ray-tracing image of the 10-m Antarctic terahertz telescope with re-imaging optics calculated by ZEMAX (Imada et al., in prep, Tsuzuki et al. 2014). This telescope design has a field of view of 1 degree.

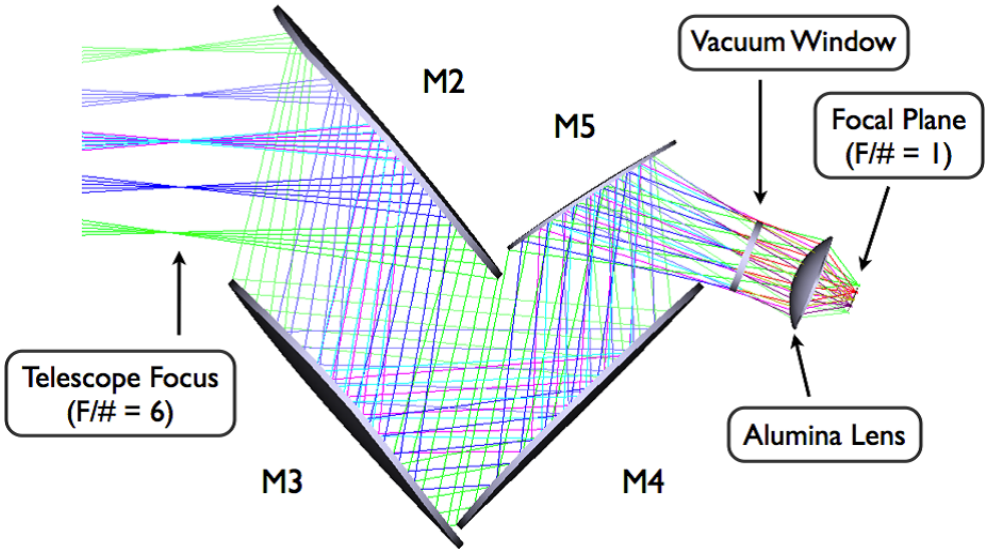

Figure 8.2: Extended figure of 1 degree field-of-view re-imaging optics after reflecting by a M1 free-form mirror (Tsuzuki et al., 2014). The size of telescope focus, vacuum window and focal plane are 1000 mm, 400 mm and 160 mm, respectively. In this design, X-Y polynomial reflective mirrors and aspheric alumina lens were used.

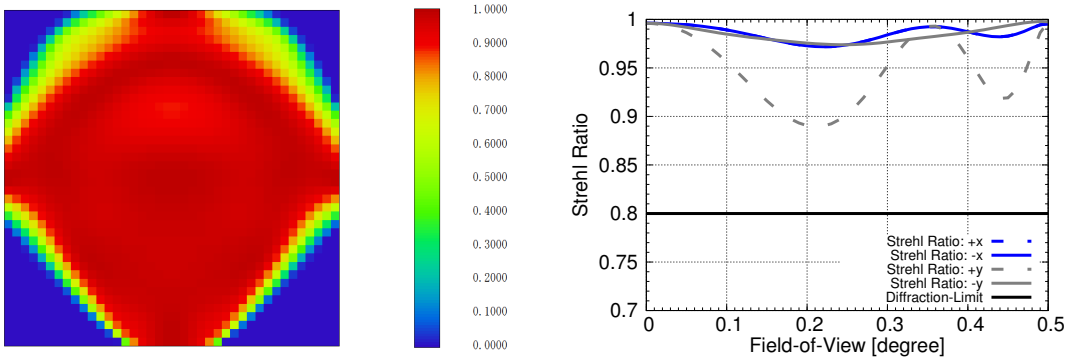

Figure 8.3: (*Left*) The Strehl ratio of 850 GHz over the focal plane. (*Right*) The Strehl ratio of 850 GHz in the x and y directions of the focal plane. Black line showed the diffraction limit (Tsuzuki et al., 2014).

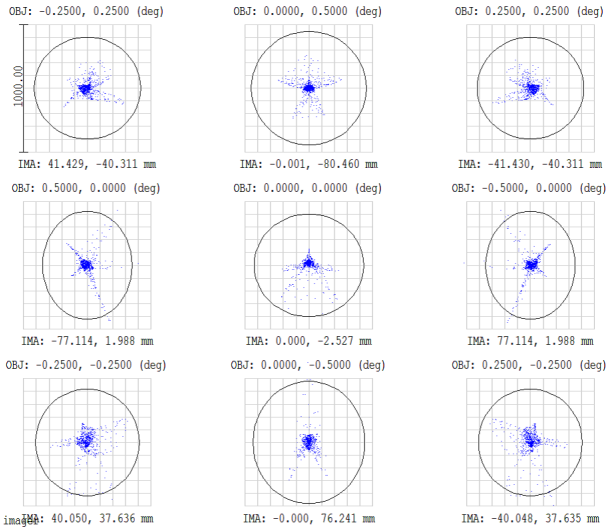

Figure 8.4: The spot diagram of 850 GHz over the focal plane (Tsuzuki et al., 2014). The center spot showed the center of the FoV, and other spots correspond to the edge of the FoV, respectively. The ray spots (blue points) are small compared to the Airy disks (black circles).

focal plane are 1000 mm, 400 mm and 160 mm, respectively. Also, the size of M2, M3, M4 and M5 mirrors are 1868, 1871, 1826 and 1062 mm, respectively. A telecentric focal plane was realized to install a large-format terahertz camera on a F/# = 1 camera focus.

The left panel of Fig. 8.3 shows the Strehl ratio of 850 GHz over the focal plane. Red color correspond to the high Strehl ratio of approximately 1. The Strehl ratio of 850 GHz in the x and y directions of the focal plane is shown in the right panel of Fig. 8.3. To obtain the smaller beam asymmetries, Strehl ratio higher than 0.8 (the Strehl ratio of 0.8

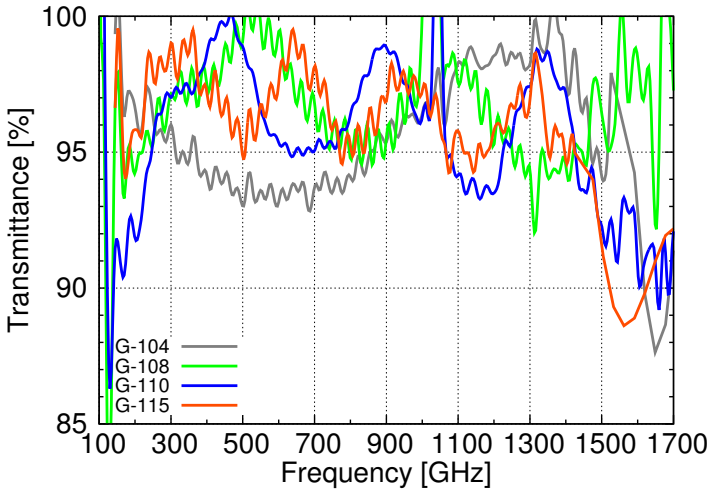

Figure 8.5: The measured transmittance of various types of the ZITEX filters at sub-millimeter region for the window of receiver cabin.

correspond to the diffraction limit) is required. The calculated results showed that the Strehl ratio higher than 0.89 over the edge of field-of-view has been achieved.

Figure 8.4 shows the spot diagram of 850 GHz over the focal plane. The center spot showed the center of the FoV, and other spots correspond to the edge of the FoV, respectively. We confirmed that the ray spots are small compared to the Airy disks (black circles). The diameter of Airy disk at 850 GHz is approximately 800 μm.

The re-imaging optics from telescope focus to focal plane will be arranged in the receiver cabin. Also, telescope focus correspond to a window of the receiver cabin. Therefore, approximately 1-m diameter window with high terahertz band transmittance is required. We investigated the ZITEX filter, which was discussed in Chapter 7, for using the window of the receiver cabin. The measured transmittance of various types of the ZITEX filters at sub-millimeter region is shown in Fig. 8.5. The interference fringes corresponding to the thickness of each ZITEX filter were observed. The ZITEX G-108 and G-110 are suitable for the window of the receiver cabin because these filters have high transmittance at 400-, 850- and 1500-GHz band which correspond to the observing frequency of the Antarctic terahertz telescope.

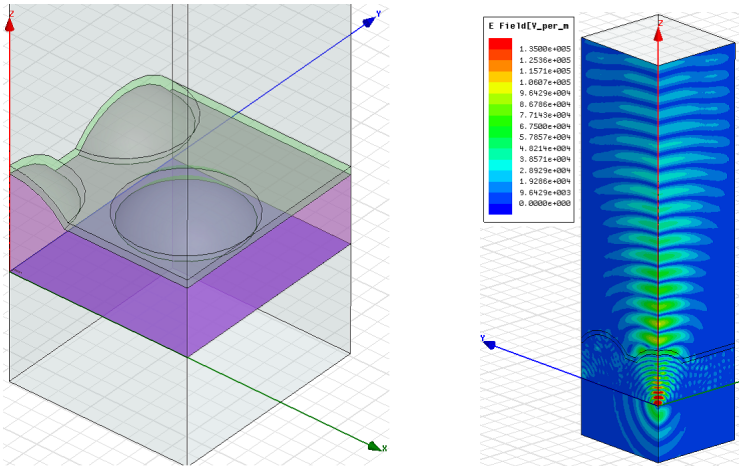

Figure 8.6: (*Left*) A HFSS model of the integrated silicon lens array. Purple and green parts showed the silicon and the Stycast AR layer, respectively. The thickness of AR layer at 850 GHz was 48 μm. (*Right*) Electric field distribution inside the integrated lens array at 850 GHz.

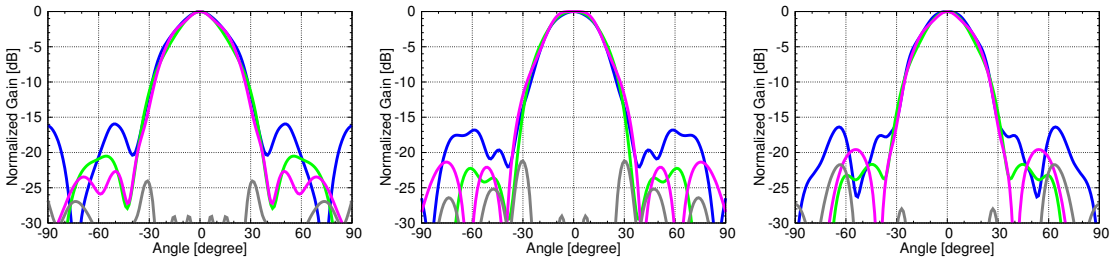

Figure 8.7: Simulated beam patterns of integrated silicon lens array at (*Left*) 810 GHz, (*Middle*) 850 GHz, and (*Right*) 890 GHz. The lens diameter, lens spacing, extension thickness and gap height were 2.4λ, 0 μm, $L/R = 0.34$ and $H/R = 0.604$, respectively.

8.3 Design of 850 GHz-bands Camera

8.3.1 Lens Array

As discussed in Chapter 5, a small-diameter silicon lens array is required to realize a wide FoV camera with large amounts of detector. Therefore, small-diameter silicon lens array for 850-GHz band was design by the 3-D full-wave electromagnetic field simulator HFSS. The design model of HFSS is shown in the left panel of Fig. 8.6. The model takes into account the effects of the surrounding lenses. Parameters of the extension thickness (L), the gap height (H) and the lens diameter (D) were optimized to achieved the good-quality beam patterns with symmetry mainlobe and low-sidelobe level less than -15

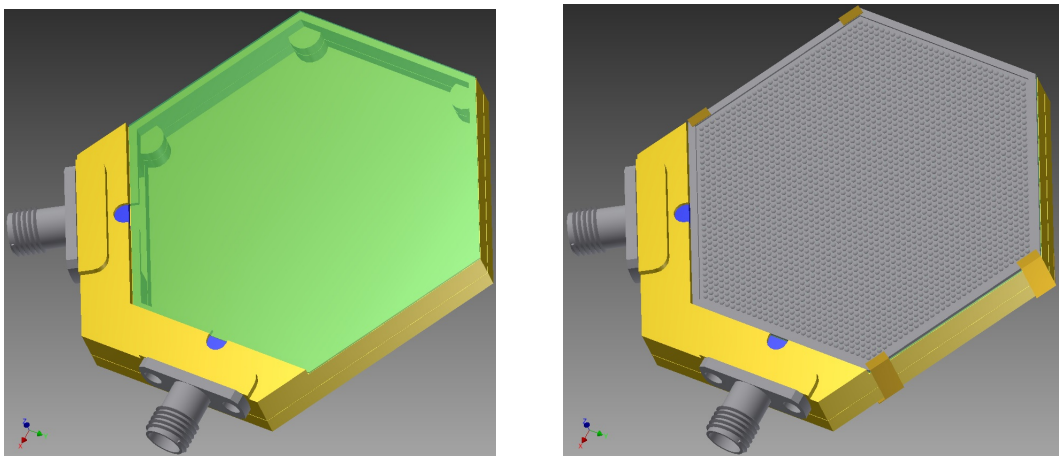

Figure 8.8: A module design of 850-GHz band camera. (*Left*) Green part showed the silicon substrate, and the bottom space is used for the carbon based absorber. (*Right*) The camera module with the 2977 pixel silicon lens array and the springs for fixing the camera module and the lens array.

dB. These parameters were summarized in chapter 5, Fig. 5.1.

The optimized parameters of the extension thickness, the gap height and the lens diameter were L/R = 0.34, H/R = 0.604 and D = 2.4λ (λ = 353 μm; the wavelength of 850 GHz), respectively. In this simulation, the detector spacing was equivalent to the lens diameter. Figure 8.7 shows the simulated beam patterns of integrated silicon lens array at (*Left*) 810 GHz, (*Middle*) 850 GHz, and (*Right*) 890 GHz. Good-quality beam patterns with symmetry mainlobe, low-sidelobe level less than $-$ 15 dB and cross-polarization level less than $-$ 20 dB were achieved by optimizing the parameters of lens array.

8.3.2 Camera Mount

Figure 8.8 shows a CAD drawing of a 850-GHz band camera module. 2977 pixel MKIDs are mounted on the camera module with a diameter of approximately 50mm. The green and gray parts correspond to the silicon substrate and silicon lens array, respectively. Gold-plated copper module with two SMA connectors for readout of the microwave signals was used. As shown in Fig. 8.8, the camera module has hexagonal shape. In this case, several modules can be assembled into a larger array which fits the circular focal plane (Lee et al., 2008).

Figure 8.9 shows a CAD drawing of a 850-GHz band camera for the 10-m Antarctica

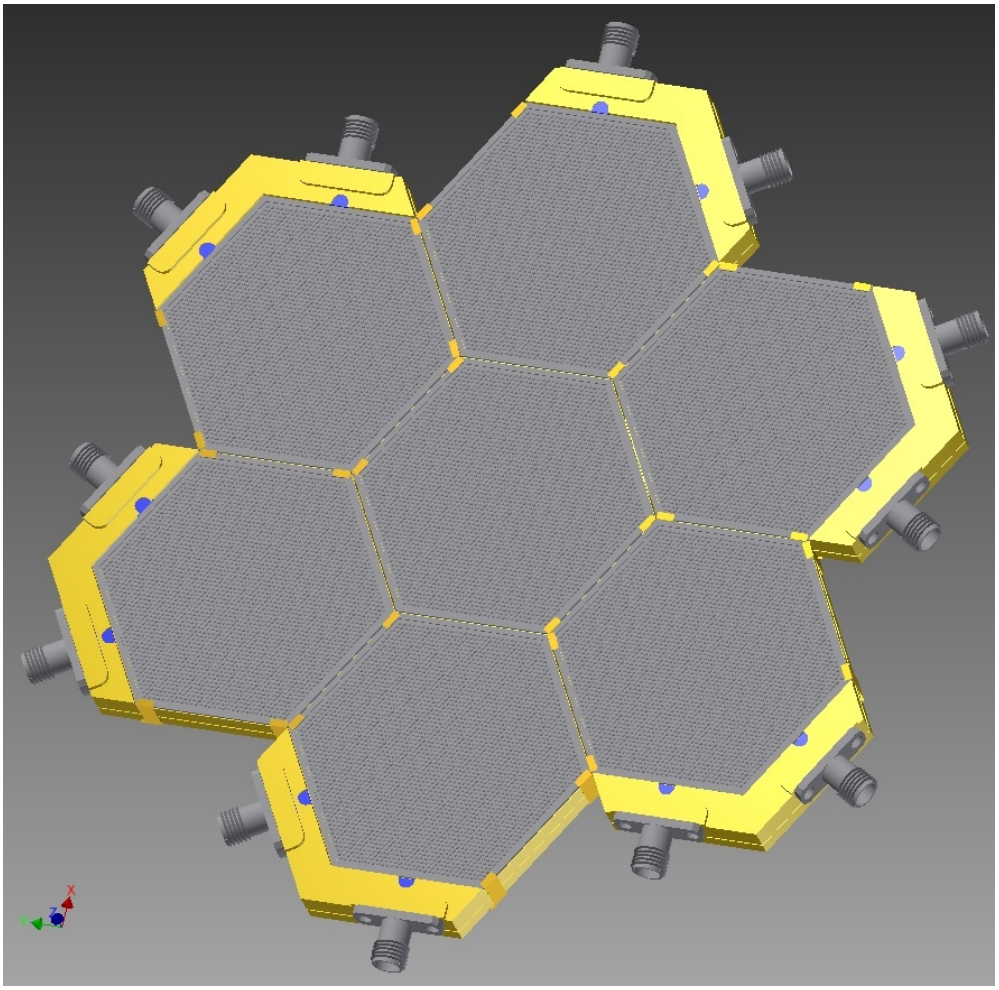

Figure 8.9: A 850-GHz band camera for the 10-m Antarctica terahertz telescope. The camera consists of the seven hexagonal modules. The camera has 20871 pixels of antenna-coupled MKID spaced 2.4·F_{focal}·λ, where F_{focal} is the focal ratio at the detectors, giving a field-of-view of 1 degree. The whole size and spacing of each camera were 160 mm and 0.3 mm, respectively.

terahertz telescope. The camera consists of the seven hexagonal modules. The camera has 20871 pixels of antenna-coupled MKID spaced 2.4·F_{focal}·λ, where F_{focal} is the focal ratio at the detectors, giving a field-of-view of 1 degree. The whole size and spacing of each camera were 160 mm and 0.3 mm, respectively. High integration density of camera assembly was obtained by reducing the area of edge space of camera module. For coaxial readout of the center module, gold bumping (Au bump) technology has been investigated.

9

Summary

A wide field-of-view (FoV) millimeter-wave camera system with a compact cryogenic re-imaging optics and a 608 pixel MKID camera has been developed. A 20000 pixels terahertz camera with seven hexagonal modules for the Antarctic terahertz telescope has also been designed. Elements and systems are summarized in the following lists.

9.1 Elements

Dielectric materials suitable for focusing lenses

Dielectric materials with low dielectric loss and high refractive index are suitable for focusing lenses. To select the dielectric materials, a refractive index and a dielectric loss tangent were measured by using a Fourier transform spectrometer (FTS). High-purity samples were selected to reduce absorption loss. High-purity silicon (11N purity) and alumina (4N purity) were suitable for focusing devices because of their high refractive index ($n > 3$) and low dielectric loss (tan$\delta \sim 10^{-4}$).

Design of silicon lens antennas for close-packed array

To realize a CCD-like large-format camera, it is required to increase the integration density of millimeter-wave camera. For this purpose, small lens diameters of 1.2, 2, and 3 times the target wavelength were investigated for the main beam symmetry, side-lobe level, cross-polarization level, and bandwidth, taking into account of the effects of the surrounding lenses. Beam patterns were calculated with the 3-D full-wave electromagnetic field simulator. Simulated results showed the circular symmetry main-lobe and low-sidelobe level of $-$ 15 dB by optimizing the lens parameters such as an extension thickness and a gap height.

Fabrication and evaluation of direct machined silicon lens array

An extended hemispherical lens array consists of a hemispherical lens and a planar plate. In this thesis, ultra-precision cutting by using ball-end mills has been demonstrated to process silicon in the shape of the extended hemispherical lens. This technique has the following advantages: there is no additional dielectric loss such as glue, high positional accuracy of many lenses is easy. The shape error and surface roughness were typically

less than 15 μm peak-to-valley and approximately 1 μm, respectively. These values are small enough for use in the millimeter-wave range. The beam patterns of the MKID camera were measured and were in good agreement with the calculations.

Anti-reflection coatings for small-diameter lens array and large-aperture lens

Epoxy based anti-reflection (AR) coatings for silicon lens array and antireflective sub-wavelength structures for large-diameter alumina lens have been demonstrated. Transmittance of the both methods, measured with a FTS, was approximately 95% at the center frequency of the 220 GHz band with a bandwidth of 25%. A broadband (approximately 70% bandwidth) design with rectangular pillar structures was also designed. This technology is important for various astronomical missions such as CMB polarization measurement and imaging spectrograph for determining the redshift of distant galaxies.

9.2 Systems

Development of wide FoV camera system at millimeter-wave bands

By using the developed elemental technologies, a wide FoV cryogenic system with two dielectric lenses and 608 pixel MKIDs has been developed. High yield of around 95% has been achieved for the 608 pixel MKID camera. The typical internal quality factor at 100 mK of this array was approximately 10^5. Also, blackbody radiation of 77 K and 300 K were distinguished by MKID array.

Design of 1 degree FoV terahertz band camera system

By extending the these technologies, a wide FoV terahertz camera system for the Antarctic terahertz telescope has been designed. The wide FoV terahertz camera system consists of re-imaging optics with reflective mirrors, refractive lens and 850-GHz band 20000 pixel camera with seven hexagonal modules. This system provides 1 degree FoV observations for detecting unknown distant galaxies.

A

Filter Transmittance of 0.3 K Optical Measurement System

Table A.1: Summary of measured filters for beam pattern measurements.

No	Filter name	Thickness [μm]
1	1-THz Low-pass Filter	250
2	1-THz Low-pass Filter	400
3	1-THz Low-pass Filter	600
4	1-THz low-pass Filter	300
5	Black Polyethylene	100
6	Black Polyethylene	125
7	ZITEX (G104)	100
8	ZITEX (G115)	400

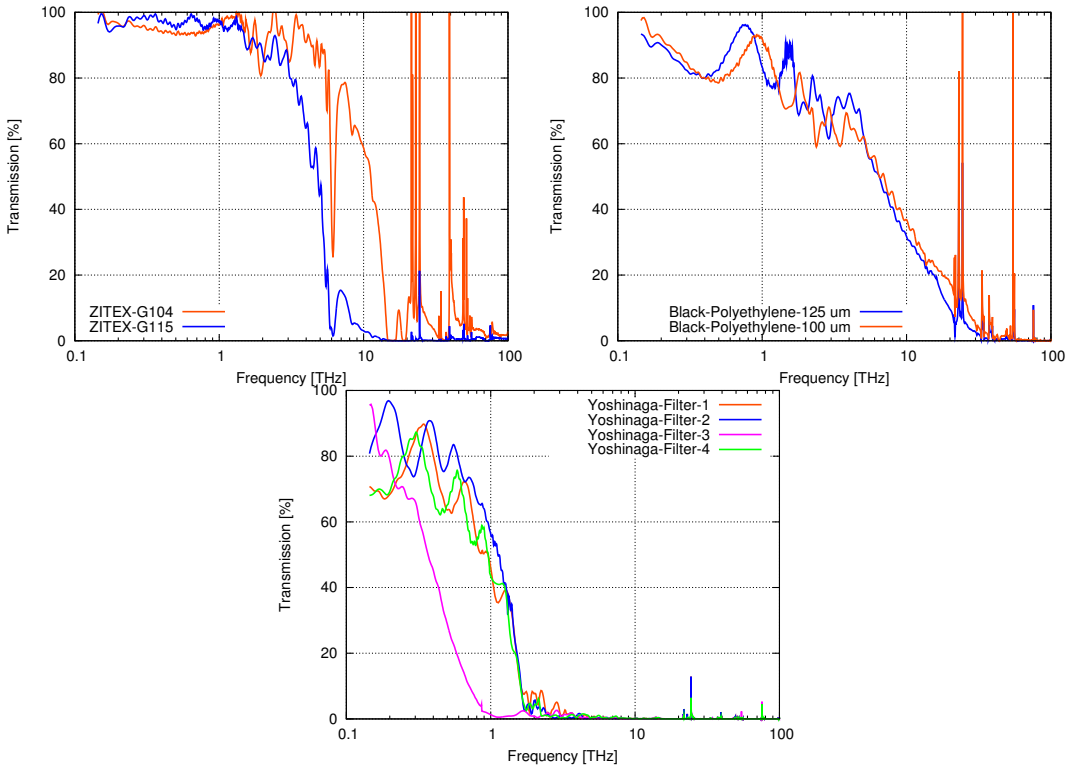

Figure A.1: The measured transmittance of the various types of the IR blocking filters at millimeter-wave to mid-infrared regions.

In this chapter, we show about filter transmittance of the 0.3 K optical system. To confirm the cutoff performance at infrared region, we measured the various types of low-pass filters with Fourier transform spectrometer. Measured filters for the 0.3 K cryostat are summarized in Table A.1. Figure A.1 shows the measured transmittance of ZITEX filters (upper left), black polyethylene filters (upper right) and 1-THz Low-pass filters

(bottom). Filter chain is composed of single ZITEX-G115 filter, triple 100 μm-thick black polyethylene filters and single 400 μm-thick 1-THz low-pass filter because of its high transmittance at millimeter-wave bands and excellent cutoff performance at infrared region.

Bibliography

Ade, P.A.R., Pisano, G., Tucker, C., & Weaver, S. 2006, in Proc. SPIE, Vol. 6275, 62750U–62750U

Alonso-DelPino, M., Llombart, N., Chattopadhyay, G., Lee, C., Jung-Kubiak, C., Jofre, L., & Mehdi, I. 2013, IEEE Antennas and Wireless Propagation Letters, 12, 84

Ariyoshi, S., Matsuo, H., Otani, C., Sato, H., Shimizu, H.M., Kawase, K., & Noguchi, T. 2005, IEEE Transactions on Applied Superconductivity, 15, 920

Arnold, K., Ade, P.A.R., Anthony, A.E., Barron, D., Boettger, D., Borrill, J., Chapman, S., Chinone, Y., Dobbs, M.A., Errard, J., et al. 2012, in Proc. SPIE, Vol. 8452, 84521D–84521D

Bardeen, J., Cooper, L.N., & Schrieffer, J.R. 1957, Physical Review, 108, 1175

Barends, R. 2009, PhD thesis, Delft University of Technology

Barucci, M., Bianchini, G., Gottardi, E., Peroni, I., & Ventura, G. 1999, Cryogenics, 39, 963

Baryshev, A., Baselmans, J.J.A., Freni, A., Gerini, G., Hoevers, H., Iacono, A., & Neto, A. 2011, IEEE Transactions on Terahertz Science and Technology, 1, 112

Baselmans, J., Yates, S., Diener, P., & de Visser, P. 2012, Journal of Low Temperature Physics, 167, 360

Biber, S., Richter, J., Martius, S., & Schmidt, L-P. 2003, in 33rd European Microwave Conference, IEEE, 1115–1118

Blain, A.W., Smail, I., Ivison, R.J., Kneib, J-P., & Frayer, D.T. 2002, Physics Reports, 369, 111

BrŘckner, C., Kńsebier, T., Pradarutti, B., Riehemann, S., Notni, G., Kley, E-B., & TŘnnermann, A. 2009, Optics express, 17, 3063

Bruggeman, V.D.A.G. 1935, Annalen der Physik, 416, 636

Burton, M.G. 2010, The Astronomy and Astrophysics Review, 18, 417

Chapman, S.C., Blain, A.W., Smail, I., & Ivison, R.J. 2005, The Astrophysical Journal, 622, 772

Chattopadhyay, G., & Zmuidzinas, J. 1998, IEEE Transactions on Antennas and Propagation, 46, 736

Choi, J., Ishitsuka, H., Mima, S., Oguri, S., Takahashi, K., & Tajima, O. 2013, Review of Scientific Instruments, 84, 114502

Clements, D.L., Vaccari, M., Babbedge, T., Oliver, S., Rowan-Robinson, M., Davoodi, P., Ivison, R., Farrah, D., Dunlop, J., Shupe, D., et al. 2008, Monthly Notices of the Royal Astronomical Society, 387, 247

Datta, R., Munson, C.D., Niemack, M.D., McMahon, J.J., Britton, J., Wollack, E.J., Beall, J., Devlin, M.J., Fowler, J., Gallardo, P., et al. 2013, Applied Optics, 52, 8747

Day, P.K., LeDuc, H.G., Mazin, B.A., Vayonakis, A., & Zmuidzinas, J. 2003, Nature, 425, 817

De Visser, P.J., Baselmans, J.J.A., Diener, P., Yates, S.J.C., Endo, A., & Klapwijk, T.M. 2012, Journal of Low Temperature Physics, 167, 335

Doyle, S., Mauskopf, P., Naylon, J., Porch, A., & Duncombe, C. 2008, Journal of Low Temperature Physics, 151, 530

Dye, S., Eales, S.A., Aretxaga, I., Serjeant, S., Dunlop, J.S., Babbedge, T.S.R., Chapman, S.C., Cirasuolo, M., Clements, D.L., Coppin, K.E.K., et al. 2008, Monthly Notices of the Royal Astronomical Society, 386, 1107

Endo, A., Van der Werf, P., Janssen, R.M.J., De Visser, P.J., Klapwijk, T.M., Baselmans, J.J.A., Ferrari, L., Baryshev, A.M., & Yates, S.J.C. 2012, Journal of Low Temperature Physics, 167, 341

Eom, B.H., Day, P.K., LeDuc, H.G., & Zmuidzinas, J. 2012, Nature Physics, 8, 623

Filipovic, D.F., Gauthier, G.P., Raman, S., & Rebeiz, G.M. 1997, IEEE Transactions on Antennas and Propagation, 45, 760

Filipovic, D.F.., Gearhart, S.S.., & Rebeiz, GM. 1993, IEEE Transactions on Microwave Theory and Techniques, 41, 1738

Fowler, J.W., Niemack, M.D., Dicker, S.R., Aboobaker, A.M., Ade, P.A.R., Battistelli, E.S., Devlin, M.J., Fisher, R.P., Halpern, M., Hargrave, P.C., et al. 2007, Applied Optics, 46, 3444

Gao, J., Daal, M., Martinis, J.M., Vayonakis, A., Zmuidzinas, J., Sadoulet, B., Mazin, B.A., Day, P.K., & Leduc, H.G. 2008a, Applied Physics Letters, 92, 212504

Gao, J., Daal, M., Vayonakis, A., Kumar, S., Zmuidzinas, J., Sadoulet, B., Mazin, B.A., Day, P.K., & Leduc, H.G. 2008b, Applied Physics Letters, 92, 152505

Gatesman, A.J., Waldman, J., Ji, M., Musante, C., & Yagvesson, S. 2000, IEEE Microwave and Guided Wave Letters, 10, 264

Godi, G., Sauleau, R., & Thouroude, D. 2005, IEEE Transactions on Antennas and Propagation, 53, 1278

Haig, D.J., Ade, P.A.R., Aguirre, J.E., Bock, J.J., Edgington, S.F., Enoch, M.L., Glenn, J., Goldin, A., Golwala, S., Heng, K., et al. 2004, in Proc. SPIE, Vol. 5498, 78–94

Halpern, M., Gush, H.P., Wishnow, E., & De Cosmo, V. 1986, Applied Optics, 25, 565

Holland, W.S., Bintley, D., Chapin, E.L., Chrysostomou, A., Davis, G.R., Dempsey, J.T., Duncan, W.D., Fich, M., Friberg, P., Halpern, M., et al. 2013, Monthly Notices of the Royal Astronomical Society, 430, 2513

Holland, W.S., Robson, E., Gear, W.K., Cunningham, C.R., Lightfoot, J.F., Jenness, T., Ivison, R.J., Stevens, J.A., Ade, P.A.R., Griffin, M.J., et al. 1999, Monthly Notices of the Royal Astronomical Society, 303, 659

Hübers, H-W., Schubert, J., Krabbe, A., Birk, M., Wagner, G., Semenov, A., Gol ’tsman, G., Voronov, B., & Gershenzon, E. 2001, Infrared physics & technology, 42, 41

Hughes, D.H., Serjeant, S., Dunlop, J., Rowan-Robinson, M., Blain, A., Mann, R.G., Ivison, R., Peacock, J., Efstathiou, A., Gear, W., et al. 1998, Nature, 394, 241

Irwin, K.D.. 1995, Ph.D. dissertation, Stanford University

Irwin, K.D., & Hilton, G.C. 2005, in Cryogenic Particle Detection (Springer), 63–150

Ishii, S. 2011, Ph.D. dissertation, University of Tsukuba

Ishii, S., Seta, M., Nakai, N., Nagai, S., Miyagawa, N., Yamauchi, A., Motoyama, H., & Taguchi, M. 2010, Polar Science, 3, 213

Kamizuka, T., Miyata, T., Sako, S., Imada, H., Nakamura, T., Asano, K., Uchiyama, M., Okada, K., Wada, T., Nakagawa, T., et al. 2012, in Proc. SPIE, Vol. 8450, 845051–845051

Kaplan, S.B., Chi, C.C., Langenberg, D.N., Chang, J.J., Jafarey, S.., & Scalapino, D.J. 1976, Physical Review B, 14, 4854

Kasilingam, D., & Rutledge, D. 1986, International journal of infrared and millimeter waves, 7, 1631

Kozorezov, A.G., Volkov, A.F., Wigmore, J.K., Peacock, A., Poelaert, A., & den Hartog, R. 2000, Physical Review B, 61, 11807

Kreysa, E., Gemuend, H-P., Gromke, J., Haslam, C.G.T., Reichertz, L., Haller, E.E., Beeman, J.W., Hansen, V., Sievers, A., & Zylka, R. 1999, Infrared physics & technology, 40, 191

Lamb, J.W. 1996, International Journal of Infrared and Millimeter Waves, 17, 1997

Lanting, T.M., Cho, H-M., Clarke, J., Dobbs, M., Lee, A.T., Lueker, M., Richards, P.L., Smith, A.D., & Spieler, H.G. 2004, Nuclear Instruments and Methods in Physics Research Section A: Accelerators, Spectrometers, Detectors and Associated Equipment, 520, 548

Lau, J., Fowler, J., Marriage, T., Page, L., Leong, J., Wishnow, E., Henry, R., Wollack, E., Halpern, M., Marsden, D., et al. 2006, Applied optics, 45, 3746

Lee, A.T., Tran, H., Ade, P., Arnold, K., Borrill, J., Dobbs, M.A., Errard, J., Halverson, N., Holzapfel, W.L., Howard, J., et al. 2008, in AIP Conference Proceedings, Vol. 1040, 66

Leech, J., Tan, B.K., Yassin, G., Kittara, P., & Wangsuya, S. 2012, IEEE Transactions on Terahertz Science and Technology, 2, 61

Llombart, N., Chattopadhyay, G., & Lee, C. 2010, in International Workshop on Antenna Technology,2010, IEEE, 1–4

Llombart, N., Thomas, B., Alonso, M., Lee, C., Chattopadhyay, G., Jofre, L., & Mehdi, I. 2011, in Proceedings of the 5th European Conference on Antennas and Propagation, IEEE, 3176–3179

Loewenstein, E.V., & Smith, D.R. 1971, Applied Optics, 10, 577

Loewenstein, E.V., Smith, D.R., & Morgan, R.L. 1973, Applied optics, 12, 398

Maloney, P.R., Czakon, N.G., Day, P.K., Downes, T.P., Duan, R., Gao, J., Glenn, J., Golwala, S.R., Hollister, M.I., LeDuc, H.G., et al. 2010, in Proc. SPIE, Vol. 7741, 77410F–77410F

Marriage, T.A., Acquaviva, V., Ade, P.A.R., Aguirre, P., Amiri, M., Appel, J.W., Barrientos, L.F., Battistelli, E.S., Bond, J.R., Brown, B., et al. 2011, The Astrophysical Journal, 737, 61

Matsuo, H., Nagata, H., Mori, Y., Kobayashi, J., Okaniwa, T., Yamakura, T., Otani, C., & Ariyoshi, S. 2006, in Proc. SPIE, Vol. 6275, 627504–627504

Matsuo, H., Sakamoto, A., & Matsushita, S. 1998, Publications of the Astronomical Society of Japan, 50, 359

McMillan, W.L. 1968, Physical Review, 167, 331

Mitsui, K., et al. 2014, in Proc. SPIE

Monfardini, A., Benoit, A., Bideaud, A., Swenson, L., Cruciani, A., Camus, P., Hoffmann, C., Désert, F.X., Doyle, S., Ade, P., et al. 2011, The Astrophysical Journal Supplement Series, 194, 24

Naruse, M. 2012, PhD thesis, The University of Tokyo

Naruse, M., Ito, T., Sekimoto, Y., Toba, H., Satou, N., Sugimoto, M., Shan, W., Iizuka, Y., Kamba, T., Kamikura, M., et al. 2009a, Experimental Astronomy, 24, 89

Naruse, M., Sekimoto, Y., Noguchi, T., Miyachi, A., Nitta, T., & Uzawa, Y. 2012, Journal of Low Temperature Physics, 167, 373

Naruse, M., Sekimoto, Y., Suzuki, T., Hibi, Y., Matsuo, H., Uzawa, Y., & Noguchi, T. 2009b, in 34th International Conference on Infrared, Millimeter, and Terahertz Waves, IEEE, 1–2

Neto, A., Iacono, A., Gerini, G., Baselmans, J.J.A., Yates, S.J.C., Baryshev, A., & Hoovers, H.F.C. 2009, in 3rd European Conference on Antennas and Propagation, IEEE, 1824–1827

Nibarger, J.P., Beall, J.A., Becker, D., Britton, J., Cho, H-M., Fox, A., Hilton, G.C., Hubmayr, J., Li, D., McMahon, J., et al. 2012, Journal of Low Temperature Physics, 167, 522

Niemack, M.D., Ade, P.A.R., Aguirre, J., Barrientos, F., Beall, J.A., Bond, J.R., Britton, J., Cho, H.M., Das, S., Devlin, M.J., et al. 2010, in Proc. SPIE, Vol. 7741, 77411S–77411S

Noroozian, O., Gao, J., Zmuidzinas, J., LeDuc, H.G., & Mazin, B.A. 2009, arXiv preprint arXiv:0909.2060

Pearson, J.C., Mehdi, I., Schlecht, E., Maiwald, F., Maestrini, A., Gill, J.J., Martin, S.C., Pukala, D., Ward, J., Kawamura, J., et al. 2003, in Proc. SPIE, Vol. 4850, 650–661

Persky, M.J. 1999, Review of scientific instruments, 70, 2193

Phillips, W.A. 1987, Reports on Progress in Physics, 50, 1657

Raguin, D.H., & Morris, G.M. 1993, Applied Optics, 32, 1154

Riechers, D.A., Bradford, C.M., Clements, D.L., Dowell, C.D., Pérez-Fournon, I., Ivison, R.J., Bridge, C., Conley, A., Fu, H., Vieira, J.D., et al. 2013, Nature, 496, 329

Rosen, D., Suzuki, A., Keating, B., Krantz, W., Lee, A.T., Quealy, E., Richards, P.L., Siritanasak, P., & Walker, W. 2013, Applied Optics, 52, 8102

Ruhl, J.E., Ade, P.A.R., Carlstrom, J.E., Cho, H-M., Crawford, T., Dobbs, M., Greer, C.H., Halverson, N.W., Holzapfel, W.L., Lanting, T.M., et al. 2004, in Proc. SPIE, Vol. 5498, 11–29

Saunders, W., Lawrence, J.S., Storey, J.W.V., Ashley, M.C.B., Kato, S., Minnis, P., Winker, D.M., Liu, G., & Kulesa, C. 2009, Publications of the Astronomical Society of the Pacific, 121, 976

Sayers, J., Mroczkowski, T., Zemcov, M., Korngut, P.M., Bock, J., Bulbul, E., Czakon, N.G., Egami, E., Golwala, S.R., Koch, P.M., et al. 2013, The Astrophysical Journal, 778, 52

Sebring, T. 2010, in Proc. SPIE, Vol. 7733, 77331X–77331X

Sekiguchi, S. 2014, Master ’s thesis, The University of Tokyo

Sergeev, A.V., Mitin, V.V., & Karasik, B.S. 2002, Applied physics letters, 80, 817

Siringo, G., Kreysa, E., Kovacs, A., Schuller, F., Weiß, A., Esch, W., Gemünd, H-P., Jethava, N., Lundershausen, G., Güsten, R., et al. 2008, in Proc. SPIE, Vol. 7020, 702003–702003

Suzuki, A., Arnold, K., Edwards, J., Engargiola, G., Ghribi, A., Holzapfel, W., Lee, A.T., Meng, X.F., Myers, M.J., O’Brient, R., et al. 2012, in Proc. SPIE, Vol. 8452, 84523H–84523H

Swain, M.R., & Gallée, H. 2006, in Proc. SPIE, Vol. 6267, 62671K–62671K

Tamura, Y., Kohno, K., Nakanishi, K., Hatsukade, B., Iono, D., Wilson, G.W., Yun, M.S., Takata, T., Matsuda, Y., Tosaki, T., et al. 2009, Nature, 459, 61

Tomaru, T., Hazumi, M., Lee, A.T., Ade, P., Arnold, K., Barron, D., Borrill, J., Chapman, S., Chinone, Y., Dobbs, M., et al. 2012, in Proc. SPIE, Vol. 8452, 84521H–84521H

Tran, H., & Page, L. 2009, in Journal of Physics: Conference Series, Vol. 155, 012007

Tsunawaki, Y., Yamamoto, Y., Kusaba, M., & Asakawa, M. 2004, Journal of Osaka Sangyo University. Natural Sciences, 39

Tsuzuki, T., et al. 2014, in Proc. SPIE

Tucker, C.E., & Ade, P.A.R. 2006, in Proc. SPIE, Vol. 6275, 62750T–62750T

Van der Vorst, M.J.M. 1999, Ph.D. dissertation, Elect. Eng. Dept., Eindhoven Univ. Technol., Eindhoven, The Netherlands

Vanderlinde, K., Crawford, T.M., de Haan, T., Dudley, J.P., Shaw, L., Ade, P.A.R., Aird, K.A., Benson, B.A., Bleem, L.E., Brodwin, M., et al. 2010, The Astrophysical Journal, 722, 1180

Wagner-Gentner, A., Graf, U.U., Rabanus, D., & Jacobs, K. 2006, Infrared physics & technology, 48, 249

Wang, W.H.., Barger, A.J.., & Cowie, L.L.. 2009, The Astrophysical Journal, 690, 319

Wardlow, J.L., Smail, I., Coppin, K.E.K., Alexander, D.M., Brandt, W.N., Danielson, A.L.R., Luo, B., Swinbank, A.M., Walter, F., Weiß, A., et al. 2011, Monthly Notices of the Royal Astronomical Society, 415, 1479

Wilson, G.W., Austermann, J.E., Perera, T.A., Scott, K.S., Ade, P.A.R., Bock, J.J., Glenn, J., Golwala, S.R., Kim, S., Kang, Y., et al. 2008, Monthly Notices of the Royal Astronomical Society, 386, 807

Wootten, A., & Thompson, A.R. 2009, in Proc. IEEE, Vol. 97, 1463–1471

Yamada, Y., Mitsuishi, A., & Yoshinaga, H. 1962, Journal of the Optical Society of America, 52, 17

Yamanouchi, T., Hirasawa, N., Hayashi, M., Takahashi, S., & Kaneto, S. 2003, Mem. Natl. Inst. Polar Res, 57, 94

Yates, S.J.C., Baselmans, J.J.A., Baryshev, A.M., Neto, A., Gerini, G., Barends, R., & Lankwarden, Y.J.Y. 2009, in AIP Conference Proceedings, Vol. 1185, 144

Yates, S.J.C., Baselmans, J.J.A., Endo, A., Janssen, R.M.J., Ferrari, L., Diener, P., & Baryshev, A.M. 2011, Applied Physics Letters, 99, 073505

Yoon, K.W., Ade, P.A.R., Barkats, D., Battle, J.O., Bierman, E.M., Bock, J.J., Brevik, J.A., Chiang, H.C., Crites, A., Dowell, C.D., et al. 2006, in Proc. SPIE, Vol. 6275, 62751K

Zmuidzinas, J. 2012, Annu. Rev. Condens. Matter Phys., 3, 169

Zmuidzinas, J., & LeDuc, H.G. 1992, IEEE Transactions on Microwave Theory and Techniques, 40, 1797

Zmuidzinas, J., & Richards, P.L. 2004, Proc.IEEE, 92, 1597